ULTRASONIC PLATE WAVES IN WOOD-BASED COMPOSITE PANELS

BY

BRIAN JAMES TUCKER

A dissertation submitted in partial fulfillment of the
requirements for the degree of

DOCTOR OF PHILOSOPHY

WASHINGTON STATE UNIVERSITY
Department of Civil and Environmental Engineering

AUGUST 2001

To the Faculty of Washington State University:

The members of the Committee appointed to examine the dissertation of BRIAN JAMES TUCKER find it satisfactory and recommend that it be accepted.

_____
Co-Chair

_____
Co-Chair

_____

_____

_____

ACKNOWLEDGEMENTS

First and foremost, I would like to thank the professors who served on my committee, Donald A. Bender, David G. Pollock, Michael P. Wolcott, Kenneth J. Fridley, and Lloyd V. Smith. I appreciate their guidance, patience, assistance, criticism, and encouragement. I especially send my regards out to Don and Dave for serving as co-advisors for my committee, who both offered invaluable mentorship not only for my research, but also for my career. Your patience with me is much appreciated.

I thank my family for taking the time to attend my dissertation defense and graduation. Your presence was nerve-racking, but your support was unwavering. Thank you Tom, Charlene, Laura, Mike, Liby, Carl, and Brad. It meant a great deal to me that you made the long journey up to Pullman just to see me graduate. I love you all.

How would I have ever expected to make it through graduate school without having friends to keep me sane? Thanks to Englund "first name Karl" and Dave "Fabio" Harper for the many hours of laughter and flatulence. Your time will come… I'll see to it.

Then, of course, there are the few who have already grown up, are still more mature than myself, and made sure I enjoyed my stay in Pullman: Steven Davidow, Paul Michael Dorsh, Kevin Haiar, Nick Bilunas, Jeff Peters, Scott Lockyear, Scott Kuebler, Steve Kelly, Brian Twitchell, Monique Paynter, Robert Emerson, Brad Vorhees, Thom Spear, Lee French, Joe Galloway, Frank Proctor, Sherell Ehlers, Tim Mealy, Glenn Madden, Nat Wongprasert, John Reed, Darren Sniezak, Tim Shirley, Timothy White, Petra Guerra, and the first friend I made in Washington, Eric "Sneeze" Sniezak. To some degree all of you have made an impact on my life. Thank you.

I cannot leave out my old officemates with whom I've shared many good and bad times (mostly good) and look forward to many future adventures: Judsen and Kristine Williams. I'll meet you in Vegas.

I also wish to thank the only female who was ever been able to put up with me for more than a single month (three years, in fact!) and still I consider to be one of my best friends, Jennifer Knepper.

Not to be forgotten, all of my new friends that have managed to work with me for the past few years and are still here: Scott Peterson, Kristin Meyers, Ted Ryan, Chris Brandt, Doug Pooler, Bill Parsons, Vikram Yadama, and Alejandro Bozo.

Thanks to my old bandmates from PWL: Joe Campbell, Steve Baker, Dave "Rooster" Flores, and Mark Burden. By the way, we're putting the band back together.

If my best friends back home in Durant, OK were left out here, I would never hear the end of it. Thanks for being there since the dawn of my college career: Jeremy Currie and Rodney "side order" Womble… my best friends who have always stuck with me through thick and thin.

Finally, to the person who gave me strength when I needed it most, God.

ULTRASONIC PLATE WAVES IN WOOD-BASED COMPOSITE PANELS

ABSTRACT

by Brian James Tucker, Ph. D.
Washington State University
AUGUST 2001

Co-Chairs: Donald A. Bender and David G. Pollock

Two key shortcomings of current ultrasonic nondestructive evaluation (NDE) techniques for plywood, medium density fiberboard (MDF), and oriented strandboard are the reliance on empirical correlations and the neglect of valuable waveform information. The research reported herein examined the feasibility of using fundamental physical relationships along with advanced signal analysis to evaluate material properties and locate defects in wood-based composite panels. Dispersion curves were constructed exhibiting the variation of ultrasonic flexural plate wave phase velocity with frequency. Based on shear deformation plate wave theory, flexural and transverse shear rigidity values for a variety of wood-based composite panels were obtained from the dispersion curves. Axial rigidity values were obtained directly from extensional plate wave phase velocity. Excellent agreement (within 5%) of flexural rigidity values was obtained between NDE and mechanical testing for thin panels (less than or equal to 6.4 mm). Transverse shear rigidity values were obtained from NDE, but no reliable mechanical results were obtained for comparison. Tensile and compressive axial rigidity values obtained from NDE were from 12% to 31% and from 22% to 41% higher than mechanical tension and compression test results, respectively. These differences between NDE and axial mechanical testing results are likely due to load-rate effects. Nondestructive rigidity results for thicker panels using the setup described herein were either unreliable or not interpretable due to highly attenuated signals and/or violation

of plate wave assumptions. Shear deformation laminated plate theory was used to predict flexural and axial laminate rigidity values of wood-based laminates from NDE measurements to within 3% and 25%, respectively. Plate wave NDE was also used to successfully locate a 60-mm square delaminated area within a 6.4-mm thick MDF laminate. This fundamental research advances the state-of-the-art of wood-based NDE by replacing empirical techniques with a technique based on fundamental mechanics, shear deformation laminated plate theory, and plate wave propagation theory.

TABLE OF CONTENTS

LIST OF TABLES

LIST OF FIGURES

CHAPTER 1: INTRODUCTION AND OBJECTIVES

Medium density fiberboard (MDF) and laminated veneer lumber (LVL) are among the many types of products in the steadily growing field of wood-based composites. A wide variety of process and material variables are associated with the manufacture of these wood-based composites including press time, temperature, moisture content, resin type, thickness, wood species, and so on. These variables, in combination with the inherent variability of wood, can result in unwanted defects and substandard mechanical properties in the final product. Nondestructive evaluation (NDE) techniques have been developed to minimize defects and insure quality control of the final product. These techniques are briefly discussed below.

Ultrasonic techniques have been employed in NDE of wood-based composites due to their ease of integration with in-line production and relatively low cost. Ultrasonic (above 20 kHz) transducers convert electrical energy into mechanical energy, which is propagated through material in the form of waves. Two transducers, placed a known distance apart, can be used to send and receive ultrasonic waves through a material, thus measuring the propagation speed. These waves travel several meters in fractions of a second resulting in rapid measurements, which are essential for in-line inspection. In wood-based NDE, wave speeds are correlated to material stiffness, strength, and quality based on theoretical and empirical relationships. These correlations are used to detect defects in finished products and to sort veneer and grade structural lumber for economical use of material.

Current ultrasonic NDE of wood-based materials, while robust and reliable, has shortcomings that should be addressed. Ultrasonic wave propagation speed in NDE of wood is measured by determining the time required for the waveform's leading edge to reach the receiving transducer after leaving the sending transducer. This method, while reliable for sorting

and grading, relies on empirical correlations and disregards more detailed information about the material contained in the remainder of the waveform. In fact, the received waveform often contains two types of waves, each depending on different elastic material properties. Additional information concerning the inspected material may be obtained through a more in-depth analysis of these waves, which could lead to advancements in ultrasonic wood NDE and improvements in the overall quality of commercial wood products.

A fundamental understanding of ultrasonic wave propagation will help researchers to improve the design of ultrasonic inspection systems for wood composites. These improvements will result in more accurate and informative ultrasonic NDE methods for enhanced qualitative assessment of material and reliable defect detection. To develop a better understanding and employ the additional information available in ultrasonic signals, it is necessary to begin with well-established theories of wave propagation, mechanics of materials, and laminated plates.

Due to the demand for high-modulus fiber composites (including carbon, graphite, aramid, and boron fibers) in aerospace applications, the fiber composites industry has a well-established database of NDE research including advanced ultrasonic techniques and signal processing. These techniques are based on fundamental wave propagation theories with an emphasis on mechanics of thin plates due to their abundant use in aerospace shell applications. Effective elastic properties of composites may be calculated directly from NDE measurements based solely on theoretical relationships. Damage/defect detection can be accomplished by theoretical means as well as empirical attenuation relationships.

High modulus fiber composites and wood-based composites have many similarities including heterogeneity, anisotropy, viscoelasticity, relatively low transverse shear moduli, and relatively thin, layered, plate-like geometry. In addition, both materials exhibit large attenuation

coefficients in the high-frequency ultrasonic range. This attenuation forces ultrasonic NDE into the low frequency, long-wavelength region where the prominent wave propagation modes are plate (Lamb or guided) waves. Plate waves have certain advantages over smaller wavelength ultrasonic inspection techniques when testing composites. Composites and laminates are "perceived" by the wave as homogeneous (through the thickness), orthotropic plates so long as the wavelength remains much larger than the laminate thickness. This "perception" of the material greatly reduces the complexity of the equations needed to describe the wave propagation and determine the overall material properties. Plate wave NDE techniques based on shear deformation laminated plate theory (discussed later) have been successfully used to examine high-modulus fiber composites. It is proposed that these same techniques should be applicable to wood-based composites.

This research will provide a theoretical basis for the development of advanced wood-based NDE techniques. The theoretical basis will be obtained from an improved fundamental understanding of low frequency ultrasonic wave propagation in wood-based composites, including the determination of applicable wave modes (such as plate waves) and mode characteristics (such as phase velocity and dispersion). These plate wave mode characteristics (often ignored in NDE of wood) will then be used to determine effective axial, flexural, and transverse shear stiffnesses and detect delaminations. Advanced wood NDE techniques have the potential to improve raw material utilization and perform more consistent, reliable quality control in the manufacturing process.

The primary objectives of this study relate to the investigation of ultrasonic plate wave propagation in wood-based composites. The specific objectives of this study are as follows:

1) Establish and verify experimental methods for using low-frequency, long-wavelength ultrasonic plate waves to inspect wood-based composites
2) Validate the ability of plate waves to predict effective axial, flexural, and transverse shear rigidities for a variety of homogenous and layered wood-based materials
3) Determine the feasibility of using plate waves to locate internal panel delaminations
4) Assess technical feasibility of the plate wave technique for inspection of wood-based composites

CHAPTER 2: BACKGROUND

Nondestructive evaluation (NDE) of wood has traditionally involved a combination of relatively robust test methods and well-established correlations between NDE measurements and material elastic properties. Predictions of material strength, in turn, rely on empirical relationships observed between elastic and strength properties. Evaluation techniques include impact-induced stress wave, vibration, ultrasonics, and mechanical bending.

Impact-induced stress waves have proven to be an effective in-situ inspection tool for wood structures (Ross and Pellerin 1988, 1991, and 1994). Impact-induced stress wave techniques involve a low frequency stress wave caused by mechanical means, which is often induced by a hammer equipped with an accelerometer. Ultrasonic techniques also involve stress waves, but at higher frequencies often induced by piezoelectric transducers. Speed of the stress wave or ultrasonic wave, which is often measured by determining the first arrival time, is then correlated to multiple material properties. For elastic material properties, a theoretical basis exists for a strong correlation between wave speed and axial stiffness. Previous wood research has shown reasonable correlations between elastic properties and strength; therefore, stress wave speed may also be correlated with internal bond, flexural, and axial strength. These techniques work well for general material evaluation, but they fail to disclose information on wave propagation or behavior of the wave when encountering a defect. In addition, if these techniques are used on plate specimens, slight errors exist due to the assumption of a one-directional stiffness.

Ultrasonic waves have been used to presort veneer for use in laminated veneer lumber (LVL) and are also being investigated for localized in-situ inspection of structural timbers (Ross *et al*. 1999). Ultrasonic angled beam techniques (Dickens *et al.* 1996 and Dickens *et al.* 1997)

have been used to predict the stiffness and strength of particleboard (Tucker *et al.* 1997) by developing correlations to the critically refracted longitudinal (L_{CR}) wave speed. Current commercial applications of ultrasonic wood-based NDE are relatively straightforward and robust; however, they ignore valuable information in the remainder of the transmitted waveform following the leading edge. This shortcoming greatly limits wood NDE for characterizing elastic material properties and reliably detecting defects.

Due to the prominent need for NDE in the aerospace industry, a substantial amount of research has been done on fibrous and metal composites. One of the more recently developed, well-documented aerospace NDE techniques uses low-frequency ultrasonic plate waves to inspect these composites. Effective material elastic constants may be directly calculated based on plate wave propagation theory while material defects may be located using empirical *and* theoretical means. The application of shear deformation plate waves theory has not been used to inspect wood-based composites; however, many similarities exist between fibrous composite and wood-based materials with respect to material behavior and ultrasonic properties. The theory governing plate wave propagation has been well documented by several authors (Auld 1973, Graff 1975, Kolsky 1963, Nayfeh 1995, and Viktorov 1967). The information presented herein may be found in varying degrees throughout the above references.

An ideal bulk wave is a spherical disturbance that originates from a point source and propagates through an infinite medium. A plate wave (also commonly termed Lamb or guided wave) may be thought of as a two-dimensional representation of a bulk wave bounded by an upper and lower surface. There are two distinct types of plate waves 1) extensional (symmetric, *s*) and 2) flexural (antisymmetric, *a*), each of which have an infinite number of modes (s_0, s_1, s_2, …, s_n and a_0, a_1, a_2, …, a_n) at higher frequencies. Representations of the lowest order

extensional and flexural plate wave displacement modes are presented in Figure 1. Plate waves are dispersive by nature, meaning that different frequencies travel at different speeds (phase velocities). Phase velocity is defined as the speed at which a specific phase point within the waveform (e.g. peak or valley) travels through a material.

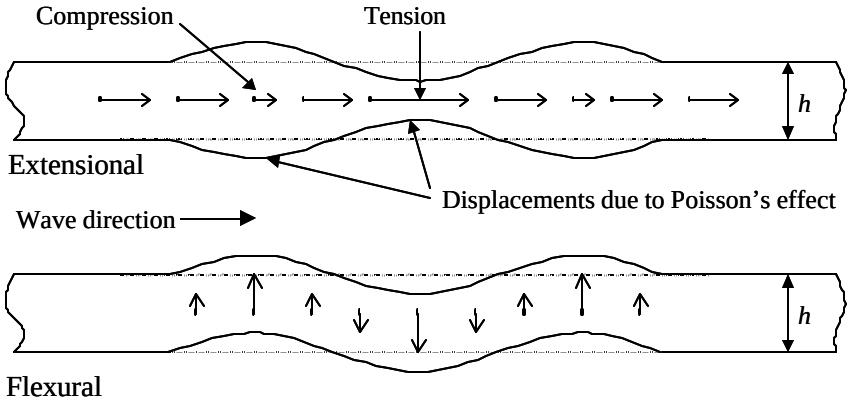

Figure 1: Displacements for plate wave modes

To alleviate wave terminology confusion, the differences between wave speed, phase velocity, and group velocity will be discussed here. Wave speed is a general term that may be defined in many ways. Historically, NDE of wood literature has defined wave speed as the distance between sensors (transducers or accelerometers) divided by the transit time (defined in Figure 2). This transit time is often dependent upon the first crossing of a specified amplitude threshold. In plate wave literature, slightly different and more explicit definitions are given for wave speeds. Phase and group velocities pertain to the phase point transit time of individual peaks within a signal and the centroid transit time of the signal, respectively (Figure 2). To properly measure these velocities, the separation between the two sensors must be changed by a known distance increment. The phase velocity may then be calculated by dividing the change in sensor separation distance by the change in phase point transit time. Group velocity may be calculated by dividing the change in sensor separation distance by the change in centroid transit

time. For nondispersive wave propagation (e.g. bulk waves and extensional plate waves at very low frequencies), phase velocity and group velocity are equal. For dispersive wave propagation, phase velocity could be either higher or lower than group velocity. Differences in phase and group velocity may be observed by examining a wave packet similar to that in Figure 2. For dispersive wave propagation, the individual peaks within the wave packet will move relative to the centroid as the wave propagates through a medium. This phenomenon is observed for surface waves in water.

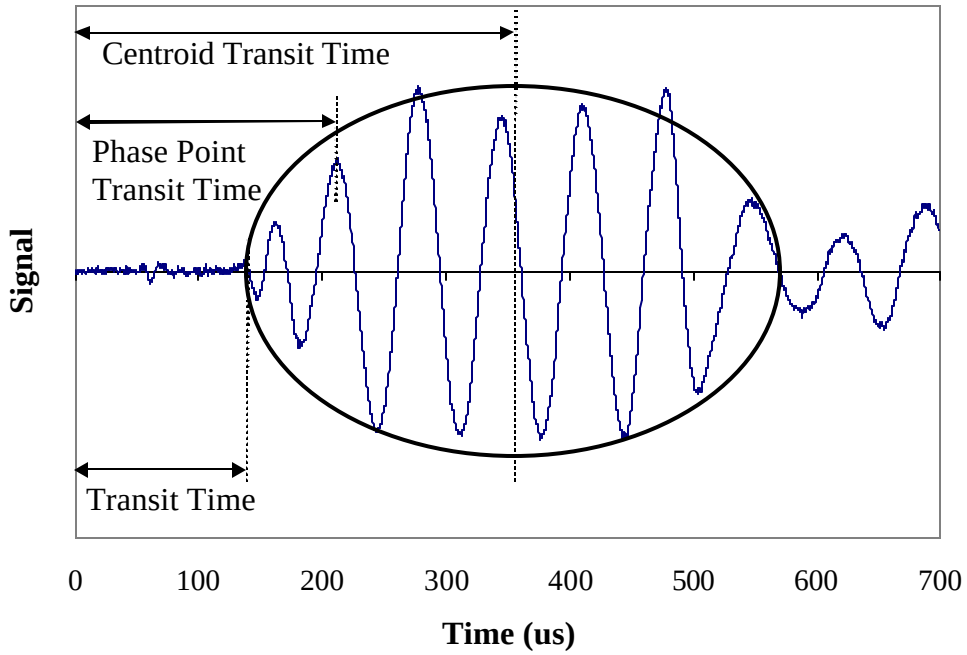

Figure 2: Definitions of transit time for use with different definitions of wave speed

Group velocities can be more difficult to calculate based on centroid transit time discrepancies. The centroid location is defined as the energy center of the wave packet. Interference from plate edge reflections with the wave packet can lead to an incorrect calculation of the wave packet centroid. In addition, edge reflections (observed after the enclosed portion of the signal in Figure 2) can also create difficulties in defining the trailing edge of the wave packet.

Phase velocities calculations are generally more accurate due to the ease of locating phase points. In addition, phase velocities offer compatibility with previously developed plate wave equations.

Dispersion curves (Figure 3) are commonly presented by plotting phase velocity on the y-axis and the frequency-thickness (*fh*) product on the x-axis. Higher modes possess distinct cut-off frequencies below which propagation does not occur; therefore, the fundamental modes may be isolated by using low frequencies (and/or thin plates). Figure 3 illustrates that the flexural mode phase velocity is greatly affected by changes in the frequency-thickness product, unlike the extensional mode.

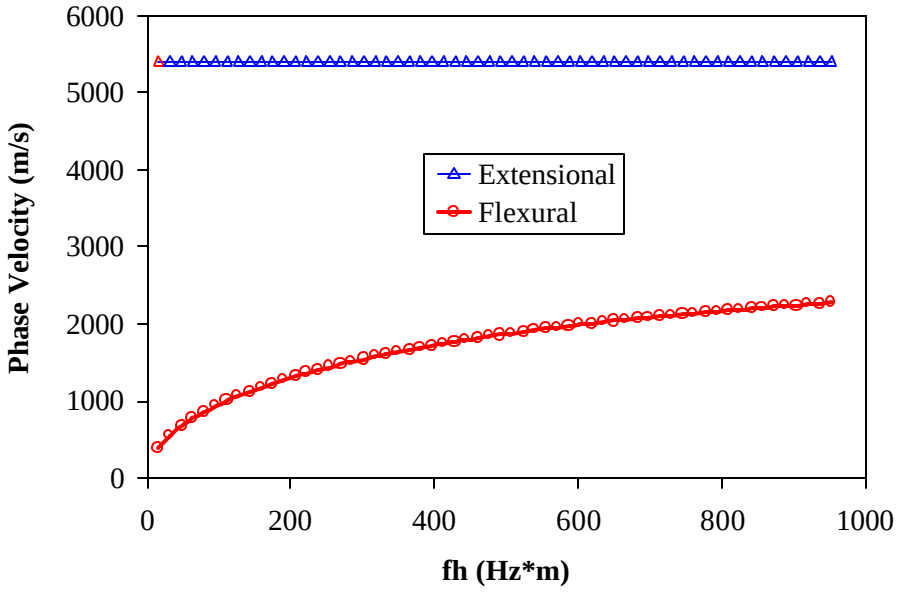

Figure 3: Dispersion curves for plate wave modes

Plate wave propagation occurs when the wavelength, l, is much greater than the thickness, *h*, of the plate ($l >> h$). Bray and Stanley (1997) recommend the wavelength be ten times greater than the thickness ($l > 10h$), while Huang (1999) proposes less stringent wavelength requirements of $l > 5h$ and $l > 3h$ for extensional and flexural waves, respectively. The remaining dimensions (length and width) of the plate must be much greater than the

wavelength. Wavelength is calculated from the phase velocity, c_{ph}, and the frequency, f as shown in Eqn. [1].

$$l = \frac{c_{ph}}{f} \qquad \textbf{[1]}$$

Dispersion relations describing how velocity varies with frequency and thickness may be derived using a fundamental elasticity approach that enforces boundary conditions on the top and bottom surfaces of the plate. While an elasticity approach results in exact dispersion relations, they are not easily applied in a practical sense because they are derived in terms of bulk wave speeds. Alternatively, Tang *et al*. (1988) presented a shear deformation laminated plate theory approximation to plate wave propagation that closely agrees with the elasticity solution. The approximate approach derivation is based on laminate properties instead of bulk wave speeds. The approximate theory was experimentally verified using a 6061-T4 aluminum specimen as well as transversely isotropic, cross-ply, and quasi-isotropic graphite/epoxy laminates. The approximate shear deformation theory is presented in APPENDIX I. Governing equations for the extensional and flexural waves in the two principal directions are presented for a cross-ply composite plate (Eqn. [2] through Eqn. [5]). From these equations, the wave number, k, may be calculated from effective laminate material rigidities (A_{11}, A_{22}, D_{11}, D_{22}, A_{44}, A_{55}) and propagated frequency, w. Effective laminate properties are used due to the low frequency, long-wavelength assumption, which considers the laminate as a homogenous material (through the thickness). Phase velocity, c_{ph}, is then calculated from the radial frequency and wavenumber (Eqn. [6]). Dispersion curves are constructed showing the change in phase velocity with respect to frequency. The inverse problem of obtaining effective stiffnesses from the dispersion curves is difficult due to the dependence on two unknowns; therefore, an iterative solution must be used (Huang *et al*. 1998). Definitions of the effective laminate material properties and the

assumptions associated with Mindlin plate theory (Mindlin 1951 and Yang *et al*. 1966) are presented in APPENDIX I. It is also assumed that all regions of the plate (over the width and length) have similar effective properties. The following expressions are based on Mindlin plate theory, which is also known as shear deformation plate theory.

Extensional 1-Direction
$$A_{11} k_1^{\,2} - \overline{r}\, w^2 = 0 \qquad \textbf{[2]}$$

Extensional 2-Direction
$$A_{22} k_2^{\,2} - \overline{r}\, w^2 = 0 \qquad \textbf{[3]}$$

Flexural 1-Direction
$$\left(D_{11} k_1^{\,2} + A_{55} - I w^2\right)\left(A_{55} k_1^{\,2} - \overline{r}\, w^2\right) - A_{55}^{\,2} k_1^{\,2} = 0 \qquad \textbf{[4]}$$

Flexural 2-Direction
$$\left(D_{22} k_2^{\,2} + A_{44} - I w^2\right)\left(A_{44} k_2^{\,2} - \overline{r}\, w^2\right) - A_{44}^{\,2} k_2^{\,2} = 0 \qquad \textbf{[5]}$$

$$c_{ph} = \frac{w}{k} \qquad \textbf{[6]}$$

A_{11}, A_{22} = effective laminate axial rigidities in principal directions

A_{55}, A_{44} = effective laminate transverse shear rigidities in principal directions

D_{11}, D_{22} = effective laminate bending rigidities in principal directions

c_{ph} = phase velocity

w = radial propagation frequency

k_i = wavenumber (or wave vector) in i-direction

$\overline{r}$ = effective density $\qquad \overline{r} = \int_{-h/2}^{h/2} r\, dz$

I = rotational inertia term $\qquad I = \int_{-h/2}^{h/2} r\, z^2\, dz$

r = mass density

Z = distance from midplane of plate

Several methods have been proposed to excite and receive plate waves in metal and fiber composite materials. These methods include immersion (Bar-Cohen and Chimenti 1986, Chimenti 1997, Karim *et al.* 1990, and Martin and Chimenti 1987), acousto-ultrasonics (AU) (Huang *et al.* 1998, Rodgers *et al.* 1991, Rose *et al.* 1987, Stiffler 1986, Tang *et al*. 1988, Tang and Henneke 1989a, and Tang and Henneke 1989b), laser generated (Han *et al*. 1999), angled beam (Rogers 1995), and air-coupled (Castaings and Cawley 1996). The immersion technique involves excitation and reception of leaky Lamb waves by immersing the specimen in liquid, which is not a feasible option for wood-based composites due to moisture absorption of the specimens. Laser generated Lamb waves require the use of relatively expensive equipment. The high attenuation coefficient in wood presents difficulties with air-coupled ultrasound. AU and angled beam techniques seem to be the most technically and economically feasible approaches to excitation of plate waves in wood-based specimens since sample immersion is not required and equipment is reasonably priced.

The AU technique used by previous researchers involved placing the transducers in direct normal contact on the same side of the specimen. Using very low frequency ultrasonics (VLF UT), plate waves were introduced into the specimen. In order to calculate phase velocity, the same phase point (usually a specific peak) on the received signal was followed as the transducers were moved apart (in the direction of phase velocity). The experimental setup and peak location method are illustrated in Figure 4 and Figure 5, respectively. Phase velocity was calculated by dividing transducer separation distance, *d*, by the change in phase point transit time. This was performed over a range of transducer excitation frequencies for the extensional and flexural modes to construct the phase velocity dispersion curves. Extensional and flexural modes had to

be distinguished in the same received signal; however, Stiffler (1986) found that the extensional mode did not propagate below certain frequencies. This was evident due to much higher phase velocities at higher transducer excitation frequencies. Although Stiffler does not offer any explanation as to why the extensional mode is absent at lower frequencies, Rose (1999) provides some clarification. As the frequency-thickness product increases, the structure of a Lamb wave changes. For extensional waves, the out-of-plane displacement increases as the frequency increases for a given thickness. Since normal contact transducers are only sensitive to out-of-plane motion, this explains the phenomenon observed by Stiffler (1986). The flexural mode may then be easily isolated at lower frequencies. Dispersion curves for the material were constructed by plotting phase velocity versus the frequency-thickness product.

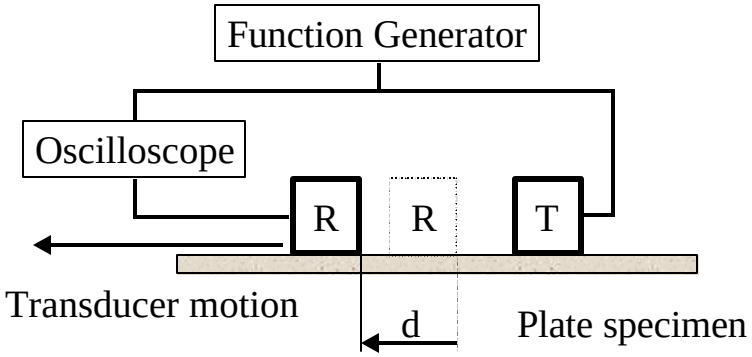

Figure 4: Acousto-Ultrasonic (AU) technique

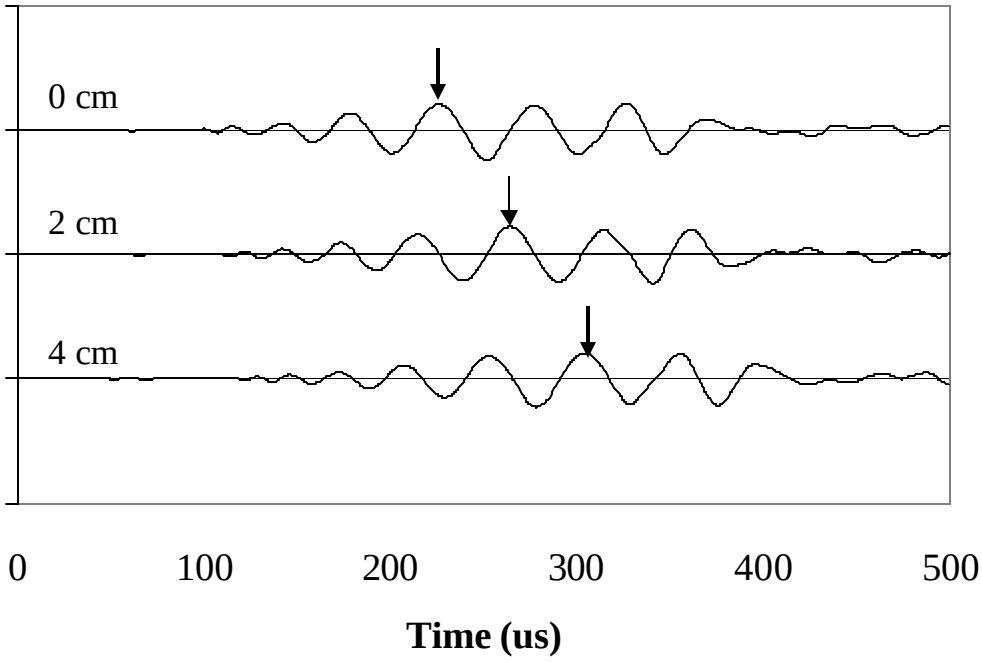

Figure 5: Tracking phase points at distances relative to initial separation distance

The angled beam method of exciting plate waves used by Rogers (1995) to inspect aluminum encompassed two angled wedges in direct contact with the same side of the specimen. This method, while similar to AU, allowed propagation of specific wave modes by selecting the appropriate combination of angles and frequencies. However, Rose *et al*. (1997) noted that for low frequency measurements, transducer directivity is compromised and the incidence angle is not always precise. Rogers (1995) also experimentally observed this behavior. In this case, many different modes were obtainable using one incidence angle. To obtain phase velocities at different frequencies, Rogers (1995) used a phase matching method. The sending transducer was excited with a continuous sine wave at a specific frequency. The receiving transducer was situated such that the received signal was in phase with the transmitted signal. This distance was recorded as X_0. The receiving transducer was moved away from the sending transducer until the received signal was 180° out of phase with the transmitted signal. This distance was recorded as

X_1. The wavelength, l, was calculated by doubling the difference between X_1 and X_0, and phase velocity, c_{ph}, was calculated from the wavelength and the frequency (Eqn. [1]).

Defect detection using plate waves can be performed based on signal attenuation or wave speed. Attenuation is generally an empirical approach whereas a theoretical basis can be applied to determine a reduction in stiffness from wave speed. Many researchers (discussed below) have used the latter approach of stiffness reduction to evaluate high-modulus fiber composites for damage or defects. Coupling, a high source of error for attenuation measurements, is not as critical in wave speed measurements.

Bar-Cohen and Chimenti (1986) examined unidirectional graphite-epoxy laminates using the leaky Lamb wave method in a C-scan type application to measure wave speed. Basing their results on stiffness reduction, they found that flexural Lamb waves are very sensitive to defects. Repeatable measurements were obtained for locating delaminations, porosity, disbonds, and regions of high/low resin content. Since Lamb waves are sensitive not only to defects, but also to changes in thickness, Martin and Chimenti (1987) developed signal processing routines to circumvent the problem of non-uniform thickness.

Tang (1988) and Tang and Henneke (1989a) used the lowest order flexural Lamb mode to monitor stiffness reduction in unidirectional and cross-ply graphite-epoxy laminates exposed to axial cracking. Stiffness reduction was predicted analytically and determined experimentally. The theoretical approach predicted a larger stiffness reduction than the actual experimental results. Results were repeatable to within 1.5% of the average value.

The lowest order flexural Lamb mode was also used by Huang et al (1998) to calculate effective laminate stiffnesses (D_{11}, D_{22}, A_{44}, and A_{55}) in a cross-ply graphite-epoxy laminate.

Changes in these stiffnesses were observed when the specimen exhibited delaminations due to impact damage.

Guo and Cawley (1993) tried a different approach to damage detection based on reflections from the edges of a plate. Using a single transducer for excitation and reception of the lowest order extensional (symmetrical) plate wave, they examined unidirectional and cross-ply graphite-epoxy composites. Analytical and experimental approaches were in good agreement. It was found that the interaction of Lamb waves with delaminations depends critically on the position of the delamination through the thickness of the laminate. Certain locations of delaminations produced no reflections and thus could not be detected.

The most common method of defect detection uses the lowest order flexural Lamb wave to determine effective composite stiffnesses. Defects and damage have a direct effect on the material stiffness and therefore may be detected. The "reflection method" used by Guo and Cawley (1993) is not as robust as the "stiffness reduction method" used by others researchers due to the inability to locate delaminations at certain locations through the thickness. Since the stiffness reduction method of damage/defect detection uses the same NDE techniques as the measurement of effective elastic properties, this method seems the most practical.

The plate wave technique used by Tang *et al*. (1988) was chosen as a basis and refined for used with wood-based composites. Their approach was relatively simply and required readily available equipment. Additional signal processing and mechanical testing were added to the approach used by Tang *et al*. (1988). The chosen method of defect detection was based on stiffness reduction. A scaled-down version from past research was used to simply evaluate the feasibility of detection. These techniques are explained in further detail in the following section.

CHAPTER 3: EXPERIMENTAL PLAN

The materials and methods used to meet the research objectives are discussed in this section. Aluminum was used to calibrate the plate wave test setup and establish procedures for testing wood-based and wheat straw composites with ultrasonic plate waves. Effective axial, flexural, and transverse shear rigidities of the aluminum were obtained, which were compared with tabulated values for aluminum from past research and industry published values. After making slight changes to the experimental procedure, plate waves were then used to inspect wood-based and natural fiber-based composites such as medium density fiberboard (MDF), oriented wheat strawboard (OWS) and plywood. Axial, flexural, and transverse shear rigidities obtained from the plate wave technique were verified by mechanical testing. Panels containing disbonds/delaminations were inspected with plate waves to determine the technical feasibility of defect detection. The materials and test methods used in this research are described in this chapter.

Materials

Material Property Validation Specimens

Wood-based and wheat straw composite and laminated panels with and without defects were fabricated for testing. The following is a list of materials tested and reasons for their inclusion in this research. Unless otherwise noted, all panels were fabricated with a width and length of 610 mm (22 in.). Panel width and length were maximized to minimize edge reflections; however, panel dimensions were limited in size due to bending test apparatus limitations. The panel length and width dimensions were five times that of the largest wavelength of 100 mm (3.94 in.) found in plywood parallel to the grain of the outermost plies.

1) Solid plate of homogeneous, isotropic material (3.2-mm (0.125-in.) thick 6061-T4 aluminum) – for calibration of procedure and comparison with past research using these test methods
2) Solid plate of transversely isotropic, pseudo-homogeneous wood-based material (3.2-mm (0.125-in.) thick MDF) – to reveal experimental procedure adjustments needed for testing a wood-based composite with low material variability within each panel (6 specimens, MDF A-F)
3) Solid plate of unidirectional, pseudo-homogeneous wheat straw (3.2-mm (0.125-in.) thick OWS) – to verify the identification of a preferred material orientation (4 specimens, OWS A-D)
4) Solid plate of transversely isotropic, pseudo-homogeneous wood-based material (6.4-mm (0.25-in.) thick MDF) – to address difficulties associated with testing thicker wood-based composites (2 specimens, MDF G and H)
5) Two-layered, pseudo-homogeneous, transversely isotropic wood-based material (6.4-mm (0.25-in.) thick MDF) – to verify the ability of plate waves to "perceive" laminates as solid sections of the same thickness (1 specimen, MDF Laminate)
6) Three-layered, pseudo-homogeneous, wheat straw cross-ply laminate (9.6-mm (0.375-in.) thick OWS) -- to verify the applicability of shear deformation, laminated plate wave theory for wood-based composites (1 specimen, OWS Laminate)
7) Layered, heterogeneous, wood-based cross-ply laminate (9.6-mm (0.375-in.) thick plywood) -- to determine the feasibility of evaluating a material with high variability (1 specimen, plywood)

This research examined the feasibility of using the plate wave technique with a variety of wood-based and wheat straw composites; therefore, a minimum number of specimens were fabricated for testing. MDF was chosen for the transversely isotropic, pseudo-homogeneous, wood-based material due to its small particle size. Transversely isotropic is defined as having the same material properties in all directions within the plane of the plate and different properties through the thickness. The small particle size of MDF created difficulties in electrostatic fiber alignment (discussed later). Therefore, wheat straw fiber with a particle length of approximately 9.6 mm (0.375 in.) was chosen for the oriented wood-based composite and cross-ply laminate. A smaller wheat straw fiber length could have resulted in a more uniform, homogeneous plate; however, the orientation was more desirable than homogeneity.

MDF panels were manufactured at Washington State University's Wood Materials and Engineering Laboratory (WMEL). Fiber was blended with powdered phenol formaldehyde (PF) resin to produce furnish with 20% resin. Panels were hand-formed by spreading the blended furnish/resin mixture into a prefabricated 750-mm (30-in.) by 750-mm (30-in.) forming box. The target density for all MDF panels was 640 kg/m^3 (40 pcf). A 910-mm (36-in.) by 910-mm (36-in.) press was used to consolidate and cure the panels at a temperature of 177 °C (350 °F). Pressure control was used to close the platens to stops at the desired thickness for each panel. The press cycle is presented in Table 1. A negative setpoint indicates closing of the platens. After pressing, each panel was weighed and measured to determine the average density.

Table 1: Press Schedule for All Panel Fabrication

Segment	Control	Setpoint	Segment Time
1	Fast Position	-0.5 in./s	30 s
2	Pressure	70.0 psi	15 s
3	Pressure	300.2 psi	10 s
4	Pressure	500.1 psi	60 s
5	Pressure	300.2 psi	60 s
6	Pressure	200.0 psi	60 s
7	Pressure	0.0 psi	10 s
8	Pressure	0.0 psi	20 s
9	Fast Position	11.970 in.	15 s

Oriented panels were fabricated using wheat straw fiber (natural or agri-fiber). Commercially available straw bales were purchased and refined using a hammermill. Target particle size was 9.6-mm (0.375-in.) in length and approximately 10-mm (0.39-in.) diameter. All oriented wheat strawboard (OWS) panels were blended with polymeric diphenylmethane diisocyanate (pMDI) resin such that the final furnish had a resin content of 4%. The blended furnish was then electrostatically oriented by dropping the furnish a distance of approximately 1 meter (39 in.) through an electrostatic field between 40 and 50 kV into a 710-mm (28-in.) by 710-mm (28-in.) forming area. All OWS panels had a target density of 640 kg/m^3 (40 pcf). OWS panels were fabricated using the same press schedule as the MDF panels. Finished OWS panels contained areas of skewed particle orientation along the edges, which were removed from the board after pressing and/or avoided during plate wave testing.

The MDF laminate was fabricated by bonding two individual MDF 3.2-mm (0.125-in.) panels together with polyvinyl acetate (PVA) resin. A five percent resin content (wet weight of adhesive / total panel weight) was used to adequately cover one side of a panel. The OWS cross-ply laminate was bonded using a cross-ply [0°/90°/0°] orientation of individual 3.2-mm (0.125-in.) OWS panels with approximately six percent resin.

Commercially produced 9.6-mm (0.375-in.) plywood was purchased from a local retailer. The plywood contained three layers oriented in cross ply [0°/90°/0°] fashion. Small specimens (560 by 560 cm (22 by 22 in.)) were cut from the larger panel to facilitate mechanical testing. Specimens were chosen with no external defects (e.g. knots, or holes) on either side of the panel coincident with the NDE inspection region.

Defect Detection Specimen

A wood-based laminate was constructed with a simulated delamination. MDF panels measuring 3.2-mm (0.125-in.) thick were used due to the material's relative homogeneity. A release agent (Pam cooking spray) was applied to a 60-mm (2.4-in.) square area at the center of the panel. PVA adhesive was applied to both lamina while avoiding the region sprayed with the release agent. The laminate was placed between two aluminum caul sheets (pressing plates) and a uniform load of approximately 7.2 kPa (150 psf) was applied while the adhesive cured.

Methods

Plate Wave Setup

This section discusses the methods used to determine elastic material properties using ultrasonic plate wave propagation including experimental setup, coupling issues, signal acquisition, mode separation, phase velocity calculation, and solving for material properties. Mechanical testing setup and apparatus are also presented.

Plate waves were transmitted and acquired using a method similar to that used by Tang and Henneke (1989a) and Stiffler (1986) since the equipment needed for this technique was readily available. Panametrics V103 broadband transducers with a center frequency of 1 MHz were used to send and receive the ultrasonic signals. A Hewlett Packard 8116A function generator was used to produce five sine bursts (burst = one cycle of a sine wave) for excitation of

the sending transducer. The sine wave burst amplitudes were ±8 volts for aluminum and ±16 volts for wood-based panels. The trigger output of the HP 8116A was connected to the trigger input of a high-speed Gage™ 2125 data acquisition card. The receiving transducer output was sent through a preamplifier located on a Panametrics 5058 pulser/receiver. (The pulser/receiver was located at least 1 meter away from the data acquisition computer monitor to minimize electromagnetic interference with the acquired ultrasonic signals.) The signal was then transmitted into the receiving "R" input of the pulser/receiver, where a filter was used to reduce high frequency noise above 1 MHz. The signal was then transferred out of the "RF" terminal and into the Gage™ data acquisition card. A personal computer was used to observe and save waveforms captured by the acquisition card using Gagescope™ software. The software was configured to average several incoming signals to eliminate noise at higher frequencies. The setup is illustrated in Figure 6.

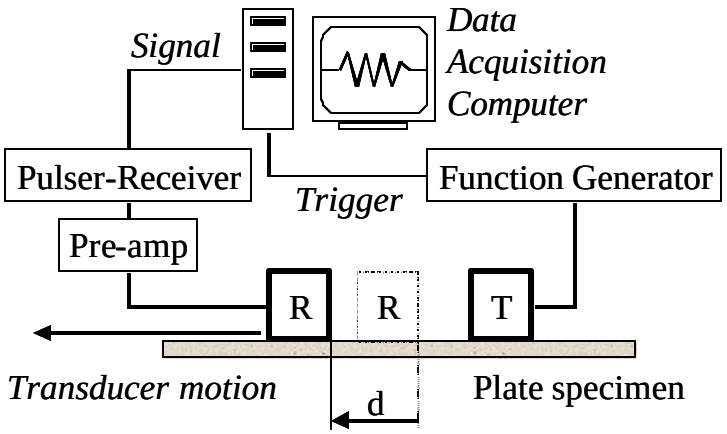

Figure 6: Plate Wave Setup

Coupling of the transducer face to the material surface proved to be a non-trivial task. Direct dry contact of the transducers with constant pressure was first attempted with little success, partially due to small surface irregularities in all materials. Silicone grease was then used in conjunction with elastomeric pads obtained from James Instruments, only to find that the

silicone couplant caused extremely large variations in phase velocity over time without any movement of the transducers. An attempt to circumvent this problem by waiting for the transit time to "settle" over time was not successful. Coupling of the transducer to the specimens was finally achieved using Neoprene pads, Ultragel II from Sonotech Industries, Inc, and a constant contact pressure achieved with 1120-gram (2.47-lb.) weights. The gel was only applied at the interface between the transducer face and the neoprene. This method of coupling provided consistent results on uneven surfaces without absorption of the couplant into the wood specimens.

Plate wave testing required a delicate balance between excitation pulse duration, initial distance between transducers, frequency, plate thickness, and material properties. The following section includes general test setup information that was applied to all specimens. For each material and thickness, the test parameters were optimized in order to achieve coherent signals by separating the different wave modes from each other and from panel edge reflections. Test details for each specimen will be described in the results and discussion section. The receiving transducer was located at an initial distance of approximately 130 mm (5 in.) center to center from the sending transducer. The initial distance was varied for individual panels to reduce reflections as will be discussed later. At the initial distance, the sending transducer was excited with sine bursts at several discrete frequencies. The frequency increment, dependent upon panel thickness and phase velocities, was chosen to achieve a frequency-thickness product increment of approximately 8 kHz-mm (203 kHz-in.). At each frequency, the received signal was recorded and saved to disk. The receiving transducer was moved a known distance away from the sending transducer using a screw-driven Velmex™ slide with an accuracy of 1/100 mm (0.00039 in.). This distance was dependent upon the material phase velocity, which was obtained from

preliminary testing. Locations of the receiving transducer were within ±40 mm (±1.57 in.) of the panel centerline; therefore, only the central 40-80 mm (1.57-3.15 in.) region of the panel was actually tested. Accuracy in relative distance measurements was more important than overall distance due to the method of phase velocity calculation to be discussed later. Signal acquisition over the same discrete frequency range was repeated at the new transducer spacing. This procedure was repeated at several transducer separation distances.

For aluminum and MDF, wave propagation in only one direction was tested due to the isotropic and transversely isotropic nature of the materials, respectively. For the OWS, laminated OWS, and plywood, both directions (parallel and perpendicular to the fiber orientation) were tested to determine the panel rigidities in both 1 and 2-directions.

Thickness measurements were taken at several receiving transducer locations along the inspected region. The average thickness of the inspected region was used to determine the material properties. The average thickness of the *entire* panel was obtained from thickness measurements at five panel locations. The average panel thickness along with the panel weight was used to calculate average panel density.

Plate specimens were supported on Styrofoam blocks except for the area directly beneath the signal path (between the sending and receiving transducers). In the NDE region, a 90-mm (3.5-in.) wide gap was formed underneath the length of the plate specimen such that no wave energy was transmitted into supporting material.

Stiffler (1986) was able to distinguish the transition from flexural to extensional plate wave modes simply by observing a change in phase velocity. However, he did not attempt to separate the co-existing extensional and flexural modes at higher frequencies. This prevented obtaining phase velocities for the flexural plate wave at higher frequencies. For this research,

mode separation was partially achieved by using a large initial distance between transducers. Since the group velocity of the lowest order extensional plate wave is much faster than the lowest order flexural wave, a long propagation distance allowed the symmetric wave to arrive much earlier. The duration of the two wave modes was also shortened so that the trailing edge of the extensional mode did not interfere with the leading edge of the flexural mode. A short number of sinusoidal bursts (4 to 6 cycles) aided in reducing the duration of each wave mode. An example of the two simultaneous modes at one frequency is presented in Figure 7. Another item that assisted in mode separation was the use of different types of Neoprene coupling pads. A hard pad was used when extensional phase velocity was being measured. The hard Neoprene was more sensitive to the out-of-plane displacements of the plate. A softer, less sensitive pad was used when measuring flexural plate phase velocities. The softer pad assisted in "filtering" out the extensional wave mode while allowing the flexural mode possessing more out-of-plane displacement to be detected.

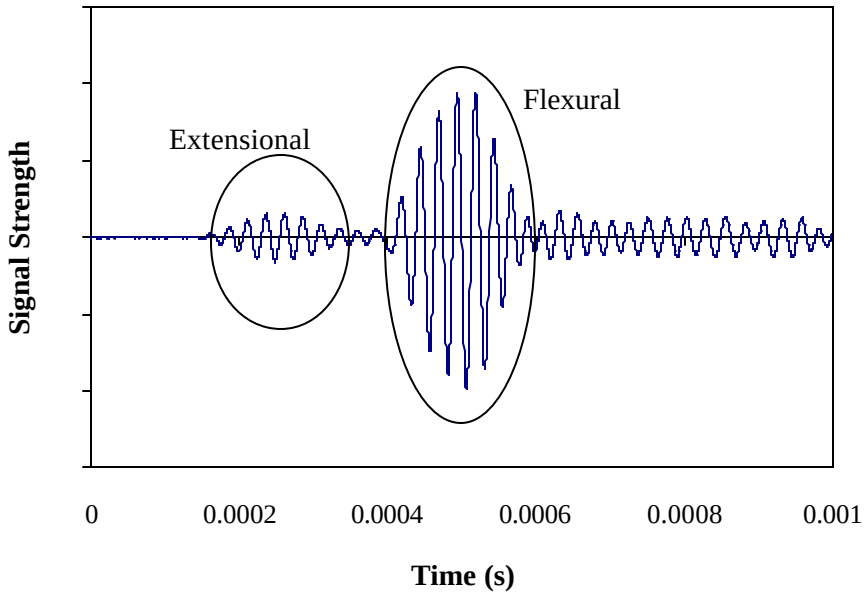

Figure 7: Co-existing Plate Modes

Plate Wave Signal Processing

A Labview virtual instrument (VI) was created to calculate phase velocities at each frequency. The custom VI was capable of viewing the captured signal, gating a portion of the signal, obtaining the temporal location of peaks (or valleys) for several distances, performing linear regression, calculating phase velocity, and estimating the transmitted frequency. The following steps were used to determine phase velocity at a particular frequency.

1) For a given excitation frequency, the signal received at the initial transducer separation distance was displayed.
2) A portion of the signal was gated, usually encompassing five phase points (peaks and valleys) (Figure 8), and displayed in an additional window. (The first few peaks of the signal were ignored due to spurious frequencies arising from dispersion, located at the leading edge of the signal. Phase point selection was susceptible to user bias)
3) The Labview "Peakfinder" function was used to locate the temporal location of the peak (or valley) of the gated signal by fitting a quadratic curve to the points with maximum magnitudes. The number of points used to define the quadratic curve was dependent upon the sampling rate and the excitation frequency. The quadratic fit was then used to find the peak location as opposed to defining a single data point as the peak. This was advantageous for analysis of noisy signals. The phase point times were stored along with the user-specified relative distance (measured from initial receiving transducer position) for subsequent analysis.
4) The next file containing the signal acquired at the second receiving transducer location was opened and steps 2 and 3 were repeated until peak times from all relative distances at a particular excitation frequency were obtained.

5) The relative distances were plotted versus the peak time locations and linear regression was used to fit the data. The slope of the line (relative distance vs. time) was used to calculate phase velocity of each phase point (Figure 9).
6) The *actual* transmitted frequency was determined from the time between consecutive phase points. This frequency was used for later comparison instead of the excitation frequency.
7) This procedure (steps 1 through 5) was repeated for each excitation frequency.

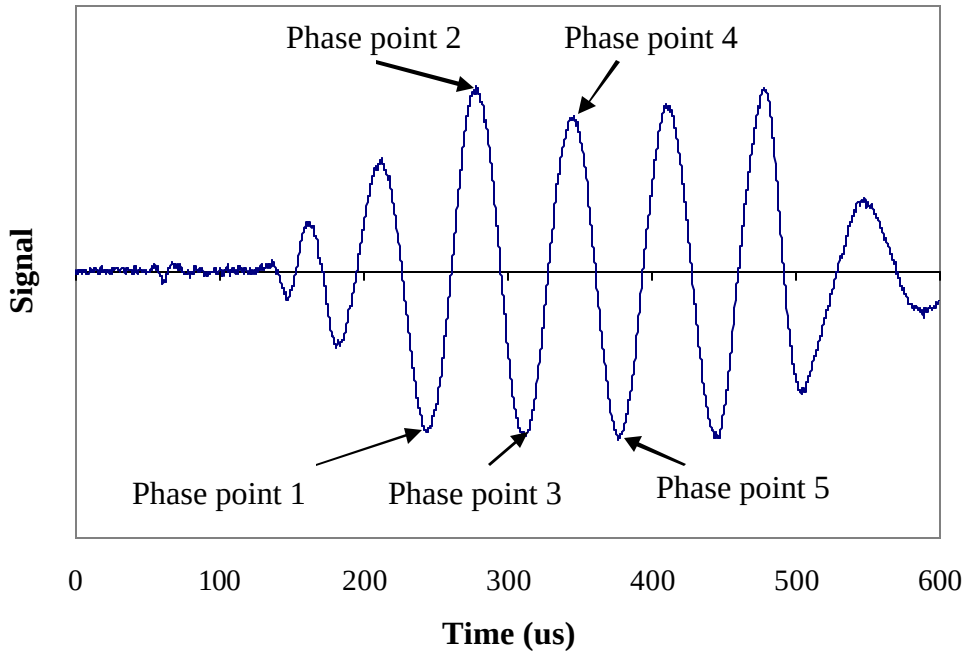

Figure 8: Identification of phase points for calculation of phase velocity

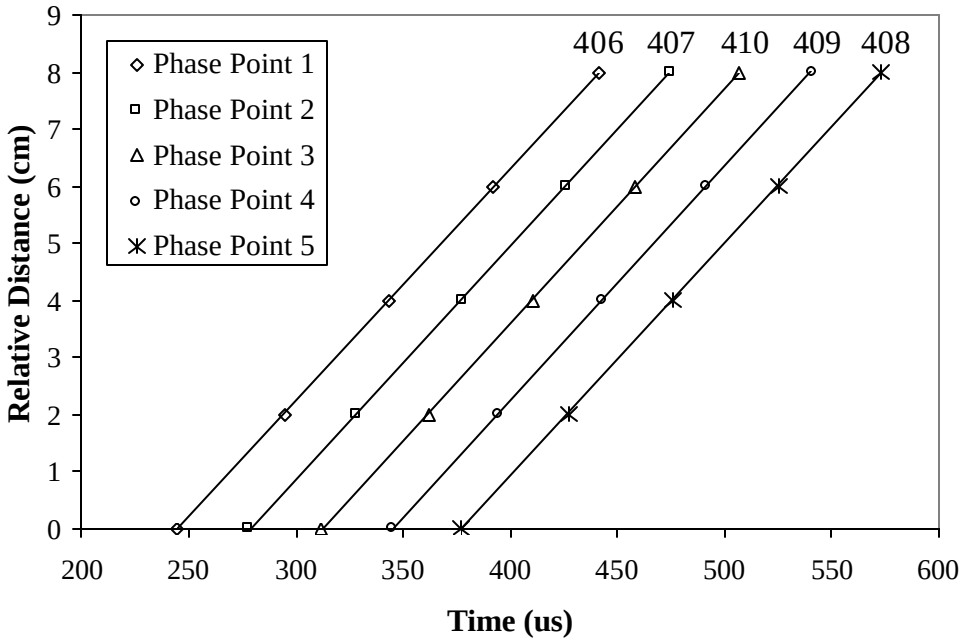

Figure 9: Typical example of linear regression used to determine phase velocities (phase velocities are indicated above each linear fit in m/s)

All frequencies, phase velocities, density, and thickness measurements were entered into an Excel spreadsheet for analysis. A dispersion plot was created with phase velocity versus the frequency-thickness (*fh*) product. The "Solver" function in Excel™ was used to fit the nonlinear dispersion relation(s) (Equations [4] and [5]) to the data (Huang *et al*. 1998). The solver used initial estimates of the flexural and transverse shear rigidities, D_{11} and A_{55} (or D_{22} and A_{44} depending on propagation direction), as input and then varied these values until the error between the experimental data and the dispersion relation was minimized. The fit of the nonlinear dispersion relation to the experimental data directly resulted in values for effective flexural and transverse shear rigidities.

In order to setup the least squares fit of the experimental data, the dispersion relation (Eqn. [4]) was solved explicitly for the wave number, *k*. The solution resulted in four roots, only one of which was real and positive. The real positive expression for wave number was used

to calculate the theoretical wave number from the effective mass density, frequency, rotational inertia, and two initial guesses for flexural and transverse shear rigidity, D_{11} and A_{55}. The experimental wave number was directly calculated from the experimentally obtained phase velocity and frequency. For each frequency, the difference between the theoretical and experimental wave numbers was calculated. Optimal values for flexural and transverse shear rigidity were obtained by minimizing the least squares difference between the experimental and theoretical wave numbers was reached. To check the consistency of the nonlinear fit, different initial guesses for flexural and transverse shear rigidity were used. Initial guesses starting at both above and below the final values were tried to insure that the solver algorithm always resulted in the same final values. The Microsoft Excel Solver uses the Generalized Reduced Gradient (GRG2) nonlinear optimization code developed by Leon Lasdon at the University of Texas at Austin, and Allan Waren, Cleveland State University. Settings for the Excel Solver used for the nonlinear dispersion curve fit are as follows: Precision, 0.00000000001; Tolerance, 0.00001%; Convergence, 0.00000000001; Use automatic scaling; Assume non-negative; Estimates, Quadratic; Derivatives, Central; Search algorithm, Newton.

Extensional phase velocities were obtained in a similar fashion to the flexural phase velocities, but using higher frequencies. Extensional phase velocities were between 5 and 10 times faster than flexural phase velocities. Receiving transducer relative distance increments were 10 mm (0.394 in.). Extensional phase velocities do not vary with frequency; therefore, the average phase velocity over all frequencies was used for calculation of axial stiffness (A_{11} or A_{22}).

For each plate specimen, one NDE test was performed. Accuracy of method was assessed using a numerical uncertainty analysis (APPENDIX V). Based on the variability of

transit times (also found in APPENDIX V), flexural rigidity was calculated within ±1% and transverse shear deformation was also calculated within ±1%.

Defect Detection Setup

To determine the feasibility of defect detection with plate waves, the plate wave test setup was used with a few differences in technique. Instead of moving the receiving transducer as needed for determination of the phase velocity, the transducers were kept at a constant 178-mm (7-in.) distance apart. The transducer pair was moved along the plate at approximately 15-mm (0.59-in.) increments with the inspection area located between the transducers (Figure 10). This procedure was used to imitate roller transducers in a process control system. At each location, several excitation frequencies were used to transmit plate waves from the sending transducer to the receiving transducer. Each received signal was saved for later analysis.

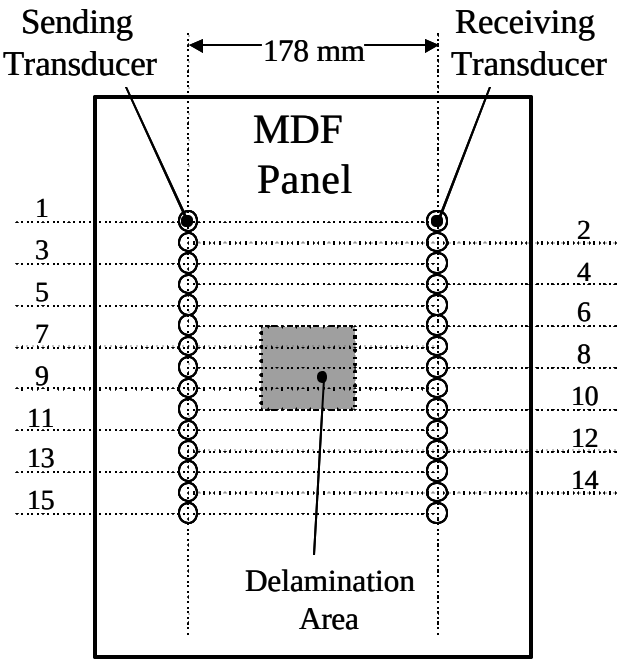

Figure 10: Defect detection setup

Defect Detection Signal Processing

For each frequency and transducer pair location, signals were analyzed and phase points (Figure 8) were tracked similar to the method used to determine phase velocity. Phase point transit times were plotted versus the transducer pair location to observe any time shifts. When phase points were not clearly defined in the acquired signal, no measurement was taken in an effort to prevent the selection of incorrect phase points. Indistinguishable signals occurred coincident with the transition between bonded and unbonded regions of the plate.

Mechanical Plate Bending

Plate wave flexural rigidity values were verified by mechanical bending. ASTM D198-99 Appendix X.4 (ASTM 1999) outlines a method to determine both the flexural and transverse shear properties of wood products; however, some of the required test spans (38 mm (1.5 in.) and less) were too small to facilitate feasible testing due to small plate thicknesses. In addition, the method for obtaining transverse shear rigidity is very sensitive to small testing errors. Therefore, plates were only tested for flexural rigidity at a span of 40 times the plate thickness to minimize the effect of transverse shear deformations. An Instron™ screw-driven test frame was used to load the plates in bending. Knife-edge supports and a line load facilitated a three-point bending setup. A 222-N (50-lb) capacity SSM-50 Interface™ load cell was used to determine the line load on the plate. Weights were placed on the plate edges directly above the supports to insure that contact between the specimens and supports was maintained especially for slightly warped specimens. Two Sensotec™ model 060-3587-04 linear variable differential transducers (LVDTs) with a ± 5.1-mm (±0.2-in.) stroke were located beneath the line load at midspan 152 mm (6 in.) on either side of the center of the panel (Figure 11). A strain rate of 1.0 percent per min was used to deflect the panel to a maximum strain of 0.5 percent. Strain was estimated from

the loading configuration and the crosshead deflection. The line load across the width of the plate, p_0, was calculated by dividing the total load, P, by the plate width, w. A load-displacement curve was constructed by plotting the line load, p_0, versus the average displacement, d, of the two LVDTs. The average displacement was used to account for any twisting of the panel during testing. Linear regression was performed to determine the slope, p_0/d, of the load-displacement curve. Flexural rigidity, D_{11}, was then calculated (Eqn. [7]) based upon the slope and span. This value was used for comparison with NDE results.

$$D_{11} = \left(\frac{p_0}{d} \right) \frac{L^3}{48} \qquad \textbf{[7]}$$

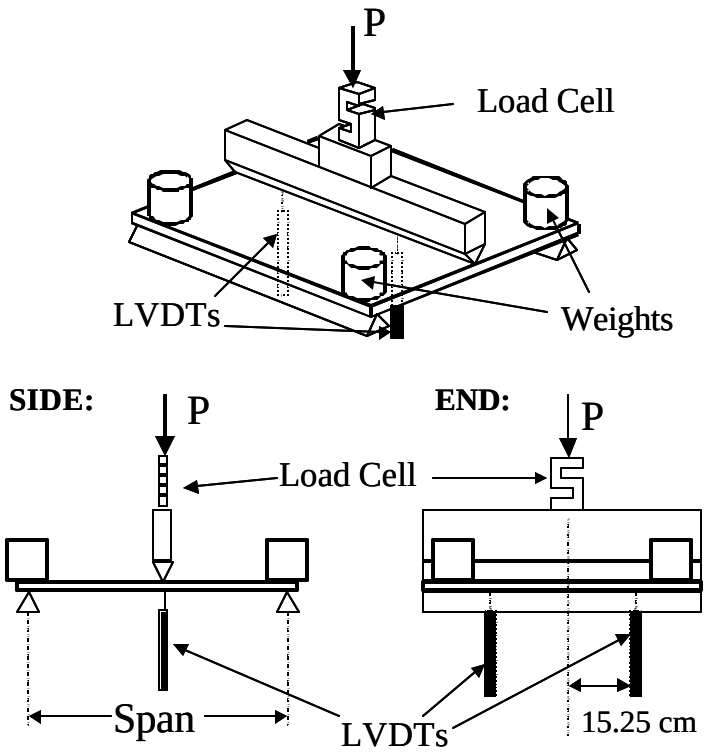

Figure 11: Plate Bending Setup

Mechanical Coupon Tests

After NDE and full plate bending tests were conducted on each panel, small coupons were cut from the panels to facilitate bending and axial testing. Bending specimens were fabricated to supplement full plate bending results and examine material taken directly from the NDE test region, minimizing any spatial variability effects. Tensile and compression coupons were fabricated primarily for obtaining axial rigidity values to compare with NDE. Due to their similar geometry, bending coupons doubled as compression coupons after they were cut down to size following the mechanical bending tests. Three coupons were cut for each test (bending and tension) and for each primary material direction (parallel and perpendicular to orientation). For MDF, only three bending and three tension specimens were needed due to the transversely isotropic nature of the material. For the OWS, OWS laminate, and plywood, twelve total specimens were obtained from each panel: three tensile and three bending in each direction.

Coupon bending specimens were removed from the center of the panel coincident with the location of the NDE test region. Tensile specimens were taken from the panel as close as possible to the center. For oriented panels, 1-direction (parallel to orientation) bending specimens were removed from the center of the plate. Bending specimens for the 2-direction (perpendicular to orientation) were obtained as close as possible to the center after the 1-direction bending specimens were removed. Tensile specimens were then taken from the remaining material. Tensile specimens were sized according to ASTM 638-00 (ASTM 2000) using Type I coupons for the 3.2-mm (0.125-in.) and 6.4-mm (0.25-in.) specimens and type IV for the thicker specimens. Bending specimens were sized according to ASTM D 790-97 (ASTM 1997) to 12.7 mm (0.5 in.) in width. The initial testing span of the coupons was 16 times the specimen depth according to ASTM; however, for reasons discussed in the results section, the

span length was increased to 24 times the specimen thickness. After testing, the bending specimens were cut into compression specimens according to ASTM D 695 – 96 (ASTM 1996). A total of six samples were obtained for each panel. The actual thickness and width of each coupon were measured at three locations along the gage length. These dimensions were averaged for calculation of area and area moment of inertia for the axial and bending specimens, respectively.

Three-point bending and axial tests were conducted using an Instron™ 4466 screw-driven 10-kN (2.2-kip) load frame. For bending tests, a 222-N (50-lb) capacity SSM-50 Interface™ load cell was used to accurately determine the load while the built-in LVDT from the Instron™ load frame was used to measure deflection. For tensile tension testing, a 10-kN (2.2-kip) Instron™ load cell and an MTS model 634.12E-24 extensometer were used. The extensometer had a gage width of 25.4 mm (1 in.). Compression specimens used the same equipment as the tensile tests with the addition of a support jig defined in ASTM D 695 – 96 (ASTM 1996). Each specimen was loaded five times to a maximum strain of 0.5 percent to obtain material stiffness and minimize damage. Plywood specimens were only loaded to a maximum strain of 0.3 percent to prevent failure. Linear regression was used to determine the slope of the load-displacement curves obtained from bending and axial testing. Slope of the load-displacement curve was then used to calculate the axial and flexural rigidities per unit width (EA/w and EI/w) for each specimen. Mechanical values from coupon testing were compared with values from full size plate testing and NDE values.

CHAPTER 4: RESULTS AND DISCUSSION

Development of Experimental Plate Wave Technique

Several plate wave setups were evaluated in order to imitate and reproduce the results of the experimental setup used by Tang *et al.* (1988) and Stiffler (1986). In addition, the setup had to be capable of obtaining accurate, reproducible, and reliable results. Using a variety of transducer frequencies, transducer placement, and coupling methods, inspection methods were tailored for each type of panel.

Since the upper range of applicable frequencies for wood-based composites was found to be around 200 kHz, an assortment of broadband transducers capable of producing frequencies within this range were used. It was found that low frequency transducers possessing a larger diameter contact face resulted in greater inconsistencies in wave transit times. It was decided to use a set of 1-MHz broadband transducers with a 15.9-mm (0.625-in.) diameter transducer face capable of efficiently transmitting signals in the 5 to 200 kHz range as well as providing consistent transit times.

Some of the excitation frequencies were in the 5 to 20 kHz range, which is within the audible range of human hearing and below the range definition of "ultrasonic". This led to problems with corrupted signals from surrounding ambient sources. Since the frequency of the noise was approximately equal to that of the excitation frequency, filters were not an option. Instead, several received signals (approximately 30+) were averaged to reduce the effect of noise.

Due to the range of frequencies used for testing, a large range of wavelengths and phase velocities was also present. This range of values created difficulties in locating phase points when a single receiving transducer increment was used. For a wavelength smaller than the

receiving transducer distance increment, the possibility existed for choosing an incorrect phase point. In addition, with a phase velocity slower than group velocity, phase points could move through the group of sinusoidal bursts and disappear at the trailing edge, resulting in no phase points to choose from if the receiving transducer was moved too far. At lower frequencies where large wavelengths existed, phase points were easily followed using a receiving transducer location increment of 30 mm. However, at higher frequencies with smaller wavelengths, a 30-mm shift made it difficult to correctly locate the same phase points at every increment. Therefore, testing was divided into segments using a larger receiving transducer increment at lower frequencies (larger wavelengths) and a smaller increment at higher frequencies (smaller wavelengths). At lower frequencies, the receiving transducer was moved 20 or 30 mm (0.79 or 1.18 in.) between measurements. At higher frequencies, 10-mm (0.39-in.) receiving transducer distance increments were used. This minimized the difficulty in locating the correct phase points at each distance interval.

For each location of the receiving transducer, a signal was acquired for each excitation frequency. As mentioned in the experimental methods section, the frequency of the *transmitted* waveform was determined. Even though the excitation frequency was identical at each receiving transducer increment, the transmitted frequency was not identical. For each received waveform, the actual transmitted frequency was calculated by measuring the transit time between peaks and valleys. It was found that the transmitted frequency was different at each receiving transducer location. Therefore, the transmitted frequencies were averaged over all receiving transducer locations. The average transmitted frequency and phase velocity (calculated at the transmitted frequency) were used to construct the dispersion curve.

Verification of Plate Wave Technique

To obtain agreement with past research and calibrate the plate wave setup, an aluminum plate specimen measuring 3.2-mm (0.125-in.) thick was tested according to the experimental methods outlined earlier. Five sinusoidal bursts at 8 volts peak to peak were used to excite the sending transducer. The received signal voltage was substantially reduced by approximately 40 dB using the attenuator located on the pulser/receiver to prevent overloading the data acquisition card input. Frequencies used ranged from 10 kHz to 120 kHz at 10 kHz increments. Phase velocities ranged from approximately 540 m/s (1770 ft/s) to 1700 m/s (5580 ft/s). A dispersion curve based on experimental values was constructed (Figure 12) and found to closely agree with the theoretically constructed dispersion curve based on tabulated values for aluminum 6061-T4. Effective flexural and transverse shear rigidities, D_{11} and A_{55}, were calculated from the experimental dispersion curve based on equation [4] and are presented in Table 2 along with the theoretical plate rigidity values. Extensional 200-kHz waves were also propagated through the plate. Average phase velocity of the extensional plate wave was determined to be approximately 5450 m/s (17,900 ft/s). The effective axial plate rigidity, A_{11}, was calculated from the phase velocity and compared well with the theoretically obtained value for axial rigidity.

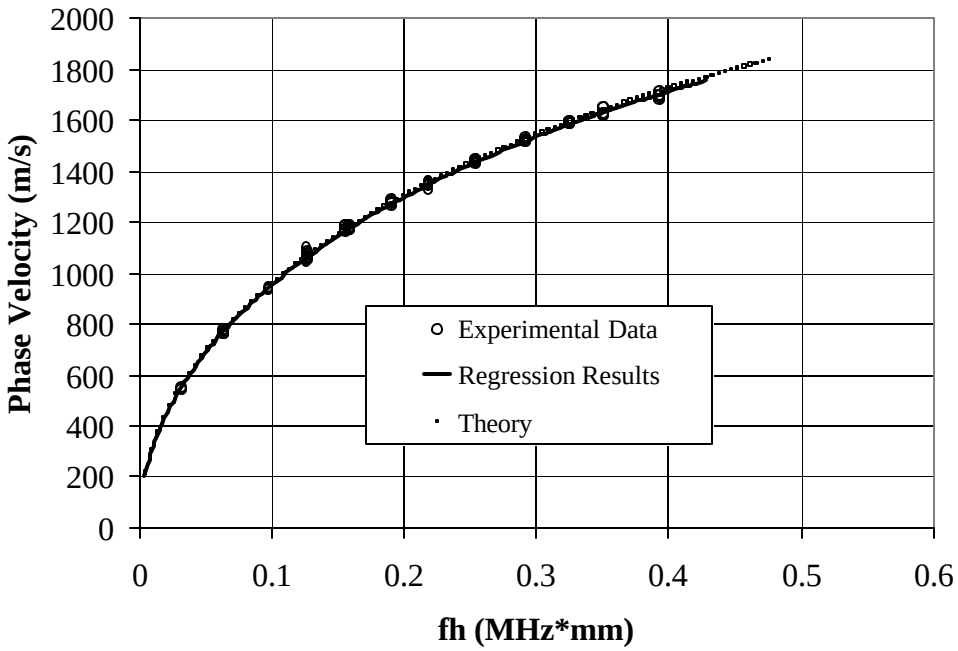

Figure 12: Experimental and theoretical dispersion curves for 3.2-mm (0.125-in.) aluminum specimen

For aluminum (an isotropic material), $D_{22} = D_{11}$, $A_{22} = A_{11}$, and $A_{44} = A_{55}$; therefore, only one set of values was obtained from one propagation direction. Using the experimentally obtained axial rigidity, A_{11}, and the published Poisson's ratio for aluminum ($n = 0.33$), the plane stress stiffness, Q_{11}, and Young's modulus, E, may be calculated (Table 2). The NDE obtained Young's modulus was within 1% of the published value, which also agrees with the research performed by Tang *et al*. (1988) and Stiffler (1986). A similar check was performed using the flexural stiffness, D_{11}, to obtain the plane stress stiffness, Q_{11}, and Young's modulus, E. These values were also in close agreement with published values and previous research. The NDE obtained shear rigidity, A_{55}, was used in conjunction with a shear correction coefficient ($k = 0.833$ for rectangle) to calculate shear modulus, G. The shear modulus was within 7% of the published value. This error is likely due to the inability of the plate wave test setup to produce data points for the flexural plate mode in the higher frequency-thickness range where transverse

shear stiffness has the largest effect. As the wavelength approaches the receiving transducer face diameter, cancellation could occur, resulting in an effective total displacement of zero. The dispersion curve fit of the data relies on the accuracy of the higher frequency-thickness data points to estimate the remainder of the dispersion curve in the transverse shear affected region. Lack of data in the higher frequency region and a poor dispersion curve fit led to an inaccurate calculation of transverse shear rigidity.

Table 2: Comparison of experimental and theoretical values for 3.2-mm (0.125-in.) thick aluminum specimen

Material Property	**Experimental**	**Theoretical**
Axial Rigidity, A_{11} (MN/m)	250	246
Flexural Rigidity, D_{11} (N-m)	208	206
Transverse Shear Rigidity, A_{55} (MN/m)	64.8	69.3
Axial Stiffness, Q_{11}, from A_{11} (GPa)	78.8	77.4
Young's modulus, E, from A_{11}	70.3	68.9
Axial Stiffness, Q_{11}, from D_{11} (GPa)	77.9	77.4
Young's modulus, E, from D_{11} (GPa)	69.5	68.9
Shear modulus, G (GPa)	24.5	26.2

Plate Wave Setup for Wood-Based and Wheat Straw Composites

For plate wave testing of wood-based and wheat straw composites, the maximum peak-to-peak voltage (16 volts) of the function generator was used to transmit the signals through the highly attenuative wood medium. Attenuation of the received signal was set close to zero on the pulser/receiver. Due to differences in stiffness and ultrasonic signal attenuation between aluminum and wood-based composites, much lower frequencies were needed to use the plate wave technique. In addition, the attenuative nature of wood reduced the amount of surrounding noise present in the acquired signals. A typical signal obtained from flexural plate wave propagation in a 3.2-mm (0.125-in.) thick medium density fiberboard specimen is presented in (Figure 8).

Applicable frequencies and phase velocities for flexural wave propagation in wood-based and wheat straw composites are presented in Table 3. Upper frequency-thickness, *fh*, limits for testing were often based on the quality of signal (e.g. strength of signal and ability to distinguish the transmitted sinusoidal pulses). Lower frequencies were needed for adequate inspection of thicker panels such as the OWS laminate and plywood. These same panels also exhibited higher phase velocities indicating higher flexural stiffness than the thinner panels. Directionality of the OWS, OWS laminate, and plywood panels was apparent from relatively higher phase velocities in the 1-direction (parallel to the particle orientation) than in the 2-direction (perpendicular to particle orientation).

Table 3: Range of values for flexural plate wave specimen testing

Panel	Frequency [kHz]	Phase Velocity c_{ph} [m/s]	Wavelength Limit Reached	fh limit [MHz-mm] (f limit [kHz])
MDF-A	5 – 65	240 – 690	N	-
MDF-B	5 – 62.5	220 – 650	N	-
MDF-C	5 – 60	230 – 680	N	-
MDF-D	5 – 47.5	230 – 630	N	-
MDF-E	5 – 70	275 – 700	N	-
MDF-F	5 – 60	220 – 690	N	-
OWS-A 1-dir	5 – 50	275 – 645	N	-
OWS-A 2-dir	5 – 47.5	210 – 450	Y	0.1514 (47.5)
OWS-B 1-dir	5 – 50	290 – 650	N	-
OWS-B 2-dir	5 – 50	210 – 450	N	-
OWS-C 1-dir	5 – 50	290 – 660	N	-
OWS-C 2-dir	5 – 45	210 – 455	N	-
OWS-D 1-dir	5 – 50	280 – 620	N	-
OWS-D 2-dir	5 – 37.5	200 – 390	N	-
MDF-G	5 – 55	320 – 700	Y	0.2182 (35)
MDF-H	5 – 55	320 – 738	Y	0.2340 (37.5)
MDF Laminate	5 – 50	330 – 735	Y	0.2331 (37.5)
OWS Laminate 1-dir	4 – 19	380 – 535	Y	0.1722 (17)
OWS Laminate 2-dir	4 – 18	310 – 480	Y	0.1601 (16)
Plywood 1-dir	5 – 48	520 – 950	Y	0.2402 (27.5)
Plywood 2-dir	6 – 25	320 – 625	N	-

High attenuation of signals was noted in the 2-direction of the OWS specimens compared to the 1-direction possibly due to anisotropy and/or heterogeneity. However, since wood possesses a higher attenuation coefficient in the perpendicular-to-grain direction than in the parallel, this could also explain the higher attenuation properties of the composite materials. It was also noted that thicker panels were more attenuative than the thinner panels, likely due to the greater amount of material available to absorb and attenuate the signal.

Difficulties were encountered when testing the OWS laminate in the 2-direction. Due to faster phase velocity in the OWS 1-direction (for both flexural and extensional modes), waves reflected from the specimen edges reached the receiving transducer coincident with the wave traveling along the 2-direction. This difficulty was also observed for plywood. To remedy this, a smaller initial distance between transducers was used.

After all signals had been acquired for a given panel, the relative receiving transducer distance was plotted versus the phase point transit time for each frequency. Linear regression was performed to determine the slope of the line. Phase velocity at each frequency was equal to the slope obtained from linear regression as illustrated with the 3.2-mm (0.125-in.) medium density fiberboard panel (Figure 9). A good linear regression fit indicated that the material within the NDE test region was approximately homogeneous. All panels exhibited material homogeneity in the NDE test region for flexural wave propagation.

For each panel, wavelength was calculated at each excitation frequency and compared to the panel thickness to ensure that the assumed conditions existed for flexural plate wave propagation ($l >> 3h$). Wavelengths for each panel were either very close to or fell below the $3h$ limit (Table 3), suggesting that the limitations of the plate wave technique had been reached. For

transmitted frequencies having wavelengths below the minimum limit, phase velocities were plotted for reporting purposes, but were not used in the calculation of plate rigidities.

Extensional plate waves were transmitted at higher excitation frequencies, due to their small out-of-plane motion at lower frequencies. At higher frequencies, the sinusoidal burst was of shorter duration, which reduced interference with the simultaneously occurring, slower traveling flexural plate wave. Phase velocities of the extensional wave were measured at several frequencies. Since the extensional wave is non-dispersive, phase velocities were averaged over all frequencies. The transmitted frequencies, average phase velocities, and phase velocity coefficients of variation for each panel are presented in Table 4.

Table 4: Range of values for extensional plate wave testing of various plate specimens

Panel	Frequency [kHz]	Average Phase Velocity [m/s]	Phase Velocity CV
MDF-A	50 - 120	2470	1.8%
MDF-B	70 – 120	2300	0.5%
MDF-C	70 – 120	2440	2.4%
MDF-D	70 – 120	2390	1.6%
MDF-E	70 – 120	2430	1.0%
MDF-F	70 – 120	2270	2.0%
OWS-A 1-dir	80 – 100	3400	2.9%
OWS-A 2-dir	80 – 100	1850	2.3%
OWS-B 1-dir	80 – 100	3720	2.8%
OWS-B 2-dir	80 – 100	1810	2.5%
OWS-C 1-dir	95 – 120	3530	1.6%
OWS-C 2-dir	95 – 100	1960	3.7%
OWS-D 1-dir	90 – 130	3370	2.6%
OWS-D 2-dir	90	1730	9.5%
MDF-G	35 – 60	2200	3.1%
MDF-H	35 – 60	2200	3.6%
MDF Laminate	40 – 60	2430	6.0%
OWS Laminate 1-dir	100 – 110	3330	8.6%
OWS Laminate 2-dir	45 – 52.5	2070	2.9%
Plywood 1-dir	50 – 57.5	6460	8.0%
Plywood 2-dir	-	-	-

Note: High attenuation in the 2-direction of plywood prevented location of phase points

Wavelengths were calculated to determine if the 5*h* assumption for extensional waves was violated. For the OWS laminate, wavelengths fell below the limit at all frequencies and in both directions; hence, axial rigidity values from these tests were not computed.

No values for extensional phase velocity were obtained for plywood either in the 1 (strong) or 2 (weak) direction. Extensional plate waves in the plywood 2-direction were significantly attenuated (Figure 13) and thus, no phase points could be reliably identified. In the plywood 1-direction, strong extensional plate wave signals were obtained; however, poor linear regression results were observed (Figure 14) during the determination of phase velocity. A nonlinear data trend suggests that the material exhibits heterogeneity in the NDE test region, which violates as assumption of plate wave theory. Therefore, reliable axial rigidity values were not obtained for plywood in either the 1 or 2 material directions.

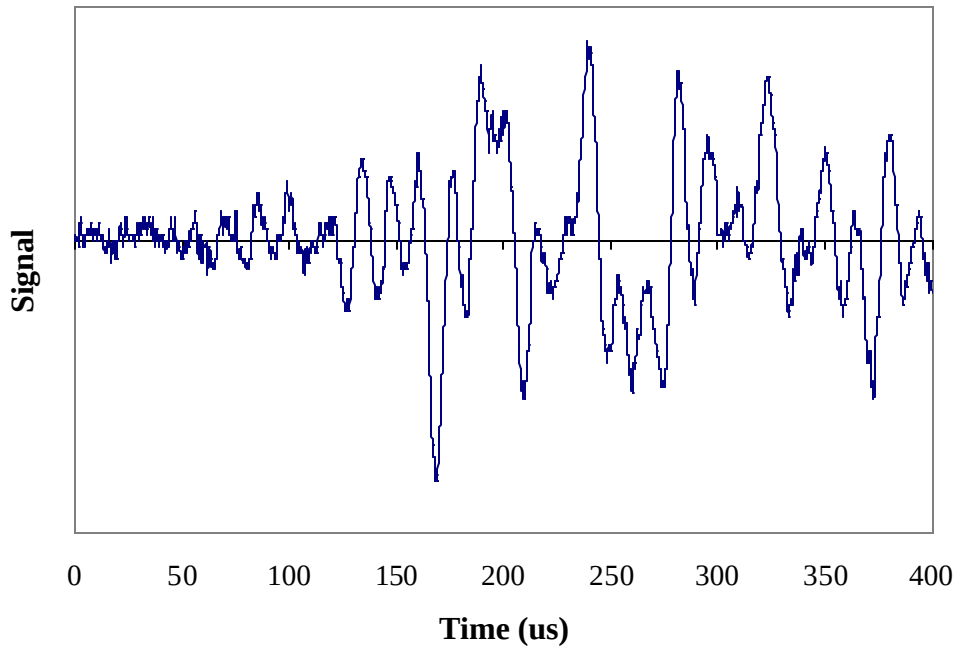

Figure 13: Highly attenuated signal obtained from plywood 2-direction at 70 kHz

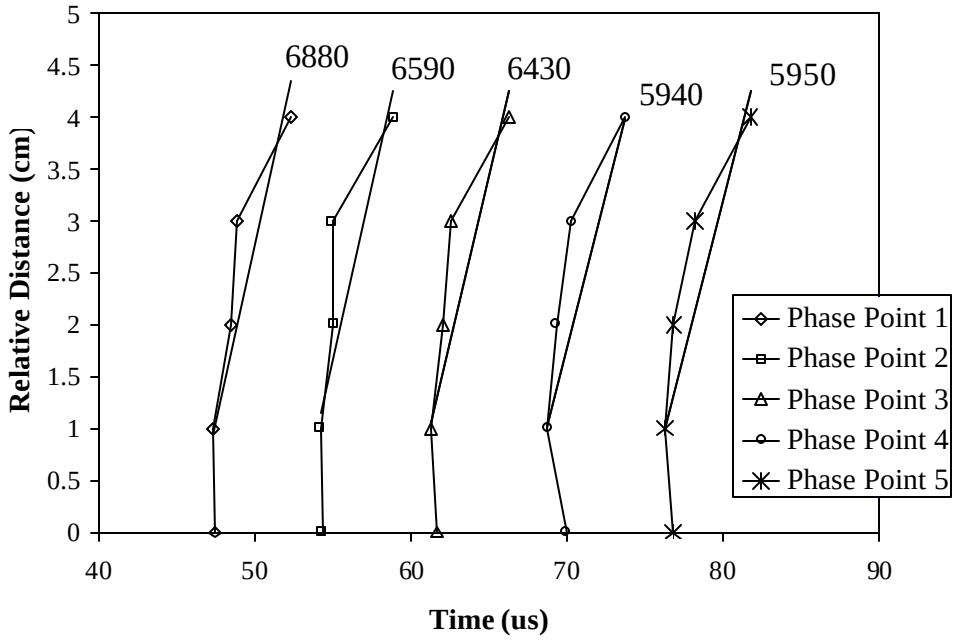

Figure 14: Linear regression of phase points extensional plate wave in 1-direction of plywood (phase velocities are indicated above in m/s)

Extensional phase velocities for relatively homogenous materials such as MDF panels with different thicknesses were comparable (e.g. MDF-F versus MDF-G), validating the fact that extensional phase velocity was independent of thickness. For the solid OWS panels, extensional phase velocity in the 1-direction was approximately two times greater than that in the 2-direction, suggesting directionality had been achieved due to orientation of fiber during panel fabrication.

The extensional phase velocity obtained from the MDF laminate was approximately 10% greater than the phase velocity obtained from either MDF-G or MDF-H panels. This is partially due to the higher modulus of the thinner panels (MDF-A and MDF-D) used to fabricate the laminate. These differences will be discussed later in this chapter. Adhesive also increases the overall axial rigidity of the laminate (assuming that the adhesive is indeed stiffer than the individual lamina).

Flexural Plate Wave Dispersion Curves

After signal analysis was performed on the acquired waveforms to determine phase velocities, dispersion curves were constructed. Due to the large number of plots, all dispersion curves may be found in APPENDIX II, except for a few selected curves of interest. The phase velocities were plotted versus the frequency-thickness product, *fh*, which was obtained from the average transmitted frequency. Two dispersion curves (one for each direction of particle orientation) were constructed on the same graph for oriented panels such as OWS, OWS laminate, and plywood. Properties of dispersion curves for comparison of panels will be discussed in addition to the difficulties encountered while plotting dispersion curves for thicker panels and laminates.

It was noted for all panels that as the wavelength approached the lower 3*h* limit assumed for flexural plate wave propagation, phase velocities became increasingly scattered within the same sinusoidal burst. For phase velocities where the wavelength fell below the 3*h* limit, the points were plotted, but were disregarded in the nonlinear regression procedure for determination of plate rigidities. The point at which the wavelengths fell below the limit is indicated on each relevant dispersion curve. Erratic phase velocities at higher frequencies could be due to another wave propagation mode (e.g. bulk) not necessarily associated with plate waves.

The dispersion curve for plywood in the 1-direction (Figure 15) began to slope upward at a frequency-thickness product of approximately 0.15 MHz-mm. At this point the wavelength was approaching the 3*h* limit. It is believed that another form of wave propagation was present at these higher frequencies. In the plywood 2-direction, dispersion curve results were not interpretable (Figure 15). This could be due to discontinuities, defects, or heterogeneities in the plywood. Based on the inability of the dispersion relation (Eqn. [4]) to adequately fit the

scattered experimental data, the flexural and transverse shear rigidity results obtained from the were deemed suspect. Therefore, plywood NDE results were not presented or used in comparisons with mechanical testing.

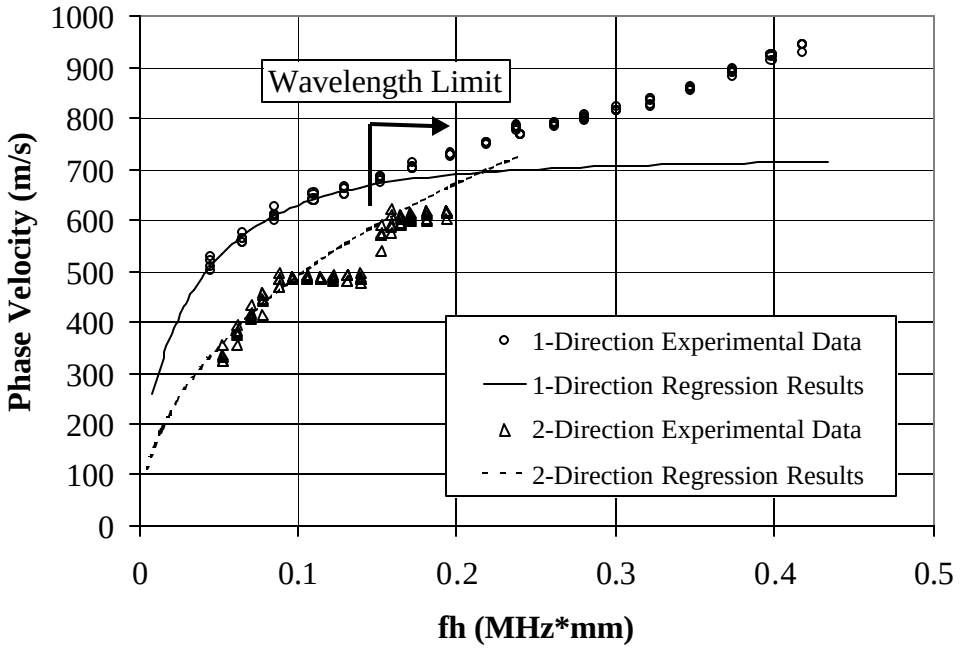

Figure 15: Dispersion curves for 9.6-mm (0.375-in.) [0/90/0] plywood

The minimum wavelength limit in the 1-direction of plywood was violated when the excitation frequency reached approximately 27.5 kHz (Table 3). At excitation frequencies beyond this point, it was noted that the phase velocities increased in approximately a linear fashion up to 50 kHz, where the test was halted. This behavior is believed to be due to another wave propagation mode. Even though no defects were observed in the panel either on the surface or after cutting the panel into coupons, the transmitted signal could have possibly been confined in the top layer of the plywood having a thickness of approximately 2.9 mm (0.11 in.). The behavior observed at higher *fh* values suggests that the wave might have only traveled through a single veneer at some point, suggesting a poor bond, or a heterogeneous material. In

summary, much larger wavelengths (lower frequencies) are needed for adequate plate wave inspection of 9.6-mm (0.375-in.) thick plywood.

Dispersion curves are generally plotted as the phase velocities relative to the *fh* product in order to normalize the curves for plates having different thicknesses, but made of the same material. In an effort to demonstrate this phenomenon, dispersion curves from 3.2 mm (0.125-in) thick MDF-B and 6.4 mm (0.25-in.) thick MDF-H were overlaid on the same graph (Figure 16). As can be seen, these two curves closely approximate each other. However, they possess markedly different flexural rigidities. Therefore, it is also valid to normalize dispersion curves by thickness for wood-based composites.

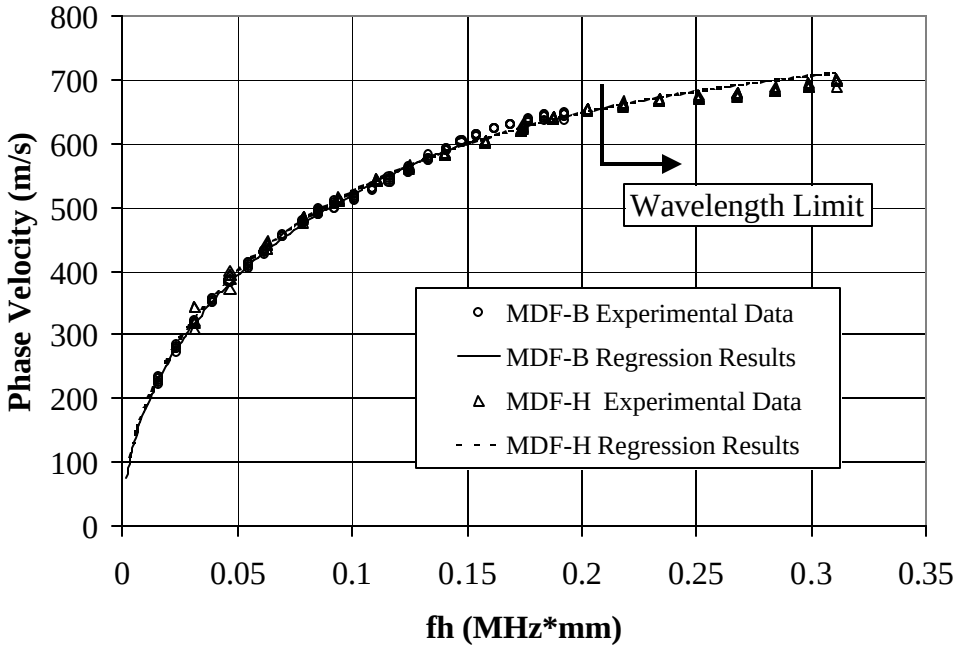

Figure 16: Overlaid dispersion curves for MDF-B and MDF-H

A laminate and a solid plate, both of the same thickness, were compared to determine if the plate wave technique would "perceive" a laminate as a solid piece of material. The MDF laminate and solid MDF-B panels were used to demonstrate this property of plate waves. Dispersion curves for both plates (laminate and solid) were overlaid on the same plot (Figure

17). As can be seen, similar curves with small differences were obtained for both panels. The MDF laminate exhibited higher flexural and transverse shear rigidities (approximately 10% and 25%, respectively) than the solid MDF specimen. This difference is due to a higher material modulus in the individual lamina used to fabricate the laminate. From NDE it was determined that axial stiffnesses, Q_{11}, of the individual panels used to make up the laminate were higher (approximately 15%) than the axial stiffness of the solid MDF panel. This is discussed in more detail during the validation of lamination theory section located later in this chapter. Identical dispersion curves would have been observed had the laminated panel and the solid panel possessed the same moduli.

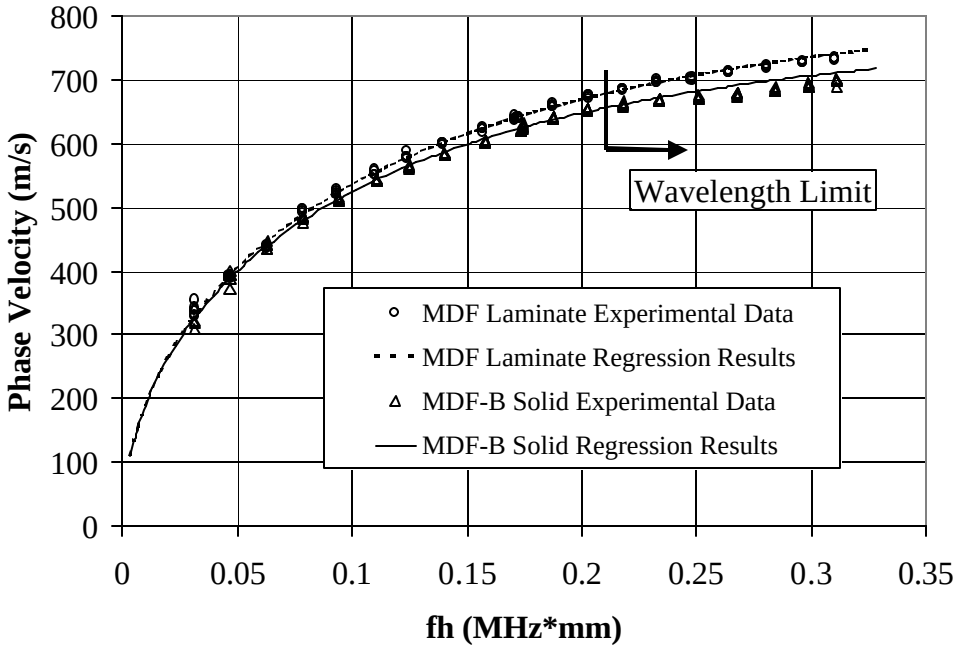

Figure 17: Overlaid dispersion curves for MDF Laminate and MDF-H

Validation of Plate Wave Technique

The following section discusses the nondestructive and mechanical tests used for validation of the plate wave technique for use with wood-based and wheat straw composites.

Comparisons between NDE and mechanical testing results are analyzed. The applicability of lamination theory is discussed based on results from NDE testing.

NDE Results

Using nonlinear regression to fit the dispersion relation to the experimental data, flexural and transverse shear rigidities were obtained for each panel (Table 5). Axial rigidity values for each panel were obtained from average extensional plate wave phase velocities (Table 6). Using the results from flexural plate wave tests, approximate Young's to shear modulus (E/G) ratios were calculated for each panel. The ratio is considered approximate because an estimate of Poisson's ratio is needed to determine Young's modulus, E. Ratios for two different estimates of Poisson's ratio are presented in Table 7. This information is taken into consideration later when spans for bending tests are being setup.

Table 5: Flexural and Transverse Shear Rigidities Obtained from Plate Wave NDE

Panel	Flexural Rigidity D_{11} **or** D_{22} **[N-m]**	Transverse Shear Rigidity A_{55} **or** A_{44} **[MN/m]**
MDF-A	7.98	2.01
MDF-B	6.26	1.55
MDF-C	7.28	1.92
MDF-D	6.77	1.92
MDF-E	7.05	1.71
MDF-F	7.06	1.21
OWS-A 1-dir	15.1	0.969
OWS-A 2-dir	4.98	0.492
OWS-B 1-dir	16.8	1.06
OWS-B 2-dir	5.46	0.474
OWS-C 1-dir	17.1	1.20
OWS-C 2-dir	5.08	0.569
OWS-D 1-dir	15.7	0.905
OWS-D 2-dir	4.30	0.389
MDF-G	52.4	2.12
MDF-H	53.7	2.46
MDF Laminate	61.3	3.14
OWS Laminate 1-dir	351	1.79
OWS Laminate 2-dir	161	1.56

Table 6: Axial rigidity results from extensional plate wave testing

Panel	Axial Rigidity A_{11} or A_{22} [MN/m]
MDF-A	12.7
MDF-B	10.9
MDF-C	12.4
MDF-D	11.9
MDF-E	12.4
MDF-F	10.7
OWS-A 1-dir	23.0
OWS-A 2-dir	6.79
OWS-B 1-dir	26.7
OWS-B 2-dir	6.32
OWS-C 1-dir	25.8
OWS-C 2-dir	8.05
OWS-D 1-dir	22.0
OWS-D 2-dir	5.82
MDF-G	18.2
MDF-H	18.6
MDF Laminate	25.6

Table 7: Comparison of average E/G ratios for each panel type

Panel(s)	E/G ratio (n = 0.33)	E/G ratio (n = 0.1)
MDF (0.32 cm)	4.0	4.4
OWS 1-Direction	14	16
OWS 2-Direction	9.7	11
MDF (0.64 cm)	5.3	5.9
MDF Laminate	4.5	5
OWS Laminate 1-Dir	17	19
OWS Laminate 2-Dir	9.1	10

Mechanical Testing Results

Full plate bending, coupon bending, and axial coupon tension specimens were tested according to the methods outlined in the experimental procedures section. The experimental results are summarized in this section. For all tests, five repetitions of loading were used to obtain five load-displacement curves. It was noted during testing that the first loading of each specimen generally resulted in a lower slope from the load-displacement curve. This was

especially evident in the full plate tests where slopes differed by as much as 4%. The difference in load-displacement slope could be due to 1) crushing or settling of the specimen at the point of load application and/or supports or 2) creep effects associated with the viscoelastic nature of the material. Load-displacement values obtained from the first loading repetition were omitted from the calculation of average material rigidity, which was used for comparison with NDE results.

Full Plate Testing

Flexural rigidity results from full plate bending tests are presented in Table 8. Directionality was observed in the OWS, OWS laminate, and plywood based on the different plate rigidity values obtained in the two material directions. Plate rigidities for thicker composites were much greater than those for thinner panels of the same material due to their larger plate section moduli. It was also noted that the OWS laminate in the 2-direction had a higher rigidity value than did plywood in the 2-direction. In the 1-direction, the OWS laminate had a lower rigidity than plywood. In this sense, plywood has a higher degree of directionality than the OWS laminate.

Table 8: Flexural rigidity values obtained from full plate mechanical bending

Panel	Flexural Rigidity D_{11} [N-m]
MDF-B	6.24
MDF-C	7.08
MDF-E	6.45
MDF-F	6.08
OWS-B 1-dir	16.6
OWS-B 2-dir	4.10
MDF-G	51.0
MDF-H	55.0
MDF Laminate	60.6
OWS Laminate 1-dir	523
OWS Laminate 2-dir	169
Plywood 1-dir	763
Plywood 2-dir	71.5

Flexural Coupon Testing

Coupon bending results were presented as flexural rigidity per unit width (EI/w) for relative comparison with results from full plate bending tests (Table 9). The difference between full plate bending and coupon bending values is that D_{11} is based on plane stress stiffness, Q_{11}, while EI/w is based on one-dimensional stiffness, E_1. The difference, which is dependent upon Poisson's ratio squared, is often considered negligible.

While considering different spans during the coupon bending test setup, large differences were observed in apparent material stiffness at different spans. This was especially apparent for OWS. Closer examination of OWS NDE results revealed a high Young's modulus to shear modulus (E/G) ratio (Table 7). For these conditions, span length becomes more critical in the determination of bending stiffness, EI/w, due to the increased deflections associated with shear deformation. Future testing should examine the sensitivity of span on the apparent bending stiffness of OWS. For this research, the longest possible span governed by the coupon length was used for bending tests.

Table 9: Results of mechanical coupon bending tests

Panel	EI/w Avg [N-m]	EI/w StDev [N-m]	EI/w CV
MDF-B	6.13	0.36	5.8%
OWS-B 1-Dir	13.0	0.19	1.5%
OWS-B 2-Dir	3.34	0.06	1.8%
MDF-H	57.4	1.63	2.8%
MDF Laminate	65.1	6.33	9.7%
OWS Laminate 1-Dir	369	11.7	3.2%
OWS Laminate 2-Dir	141	4.88	3.5%
Plywood 1-Dir	893	73.5	8.2%
Plywood 2-Dir	37.5	5.56	14.8%

Axial Coupon Testing

Results of the axial tension and compression coupon tests were reported in axial rigidity per unit width (Table 10) and (Table 11), *EA/w*, to facilitate comparison with axial rigidity results, A_{11}, from NDE extensional plate wave tests. Average values, standard deviation, and coefficient of variation are presented for all samples tested from each panel. As with the flexural coupons, there is a small difference when comparing coupon and NDE results due to the use of one-dimensional stiffness instead of the plane stress stiffness.

Table 10: Results of mechanical coupon uni-axial tension tests

Panel	EA/w [MN/m]	EA/w StDev [MN/m]	EA/w CV
MDF-B	9.55	0.72	7.6%
OWS-B 1-Dir	18.7	1.3	7.0%
OWS-B 2-Dir	4.73	0.29	6.1%
MDF-H	15.5	0.31	2.0%
MDF Laminate	21.6	0.47	2.2%
OWS Laminate 1-Dir	39.6	3.0	7.5%
OWS Laminate 2-Dir	33.2	4.4	13%
Plywood 1-Dir	107	16.4	15%
Plywood 2-Dir	47.0	27.4	58%

Table 11: Results of mechanical coupon uni-axial compression tests

Panel	EA/w [MN/m]	EA/w StDev [MN/m]	EA/w CV
MDF-B	8.45	0.89	11%
OWS-B 1-Dir	18.6	2.29	12%
OWS-B 2-Dir	4.98	0.29	5.8%
MDF-H	15.2	1.09	7.2%
MDF Laminate	18.0	2.59	14%

Comparison of NDE and Mechanical Values

Results of NDE, full plate, and coupon bending tests are presented in Figure 18, Figure 19, and Figure 20 and Table 12. Several panels were not cut into coupon specimens because they were used to fabricate laminates or panels with defects for later testing. Before laminate fabrication, all panels were tested nondestructively and mechanically to determine panel properties. However, the mechanical bending tests were deemed invalid and inconsistent due to incorrect calibration factors and inaccurate measurements of deflection, respectively. Therefore, full plate mechanical test results were not available for panels used to fabricate laminates.

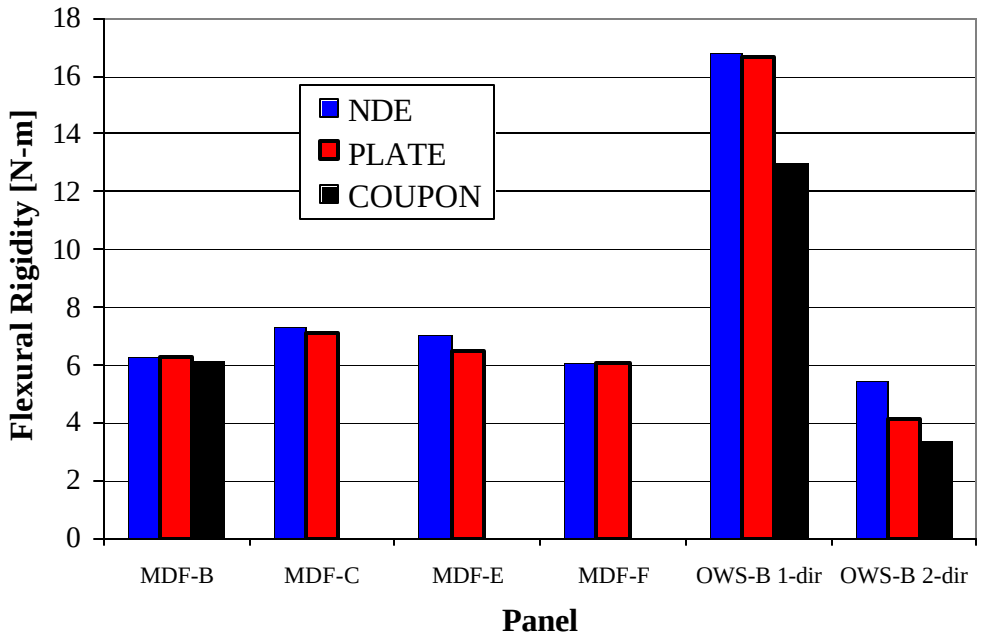

Figure 18: Comparison of NDE results with full plate and coupon mechanical bending tests for panels with relatively low flexural rigidity

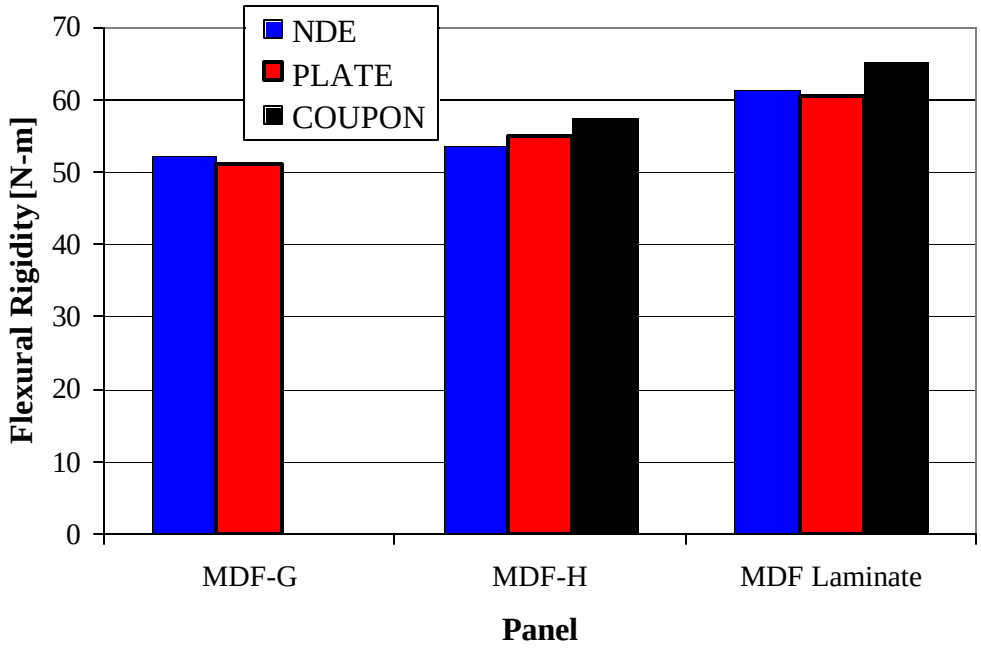

Figure 19: Comparison of NDE results with full plate and coupon mechanical bending tests for panels with a relatively medium flexural rigidity

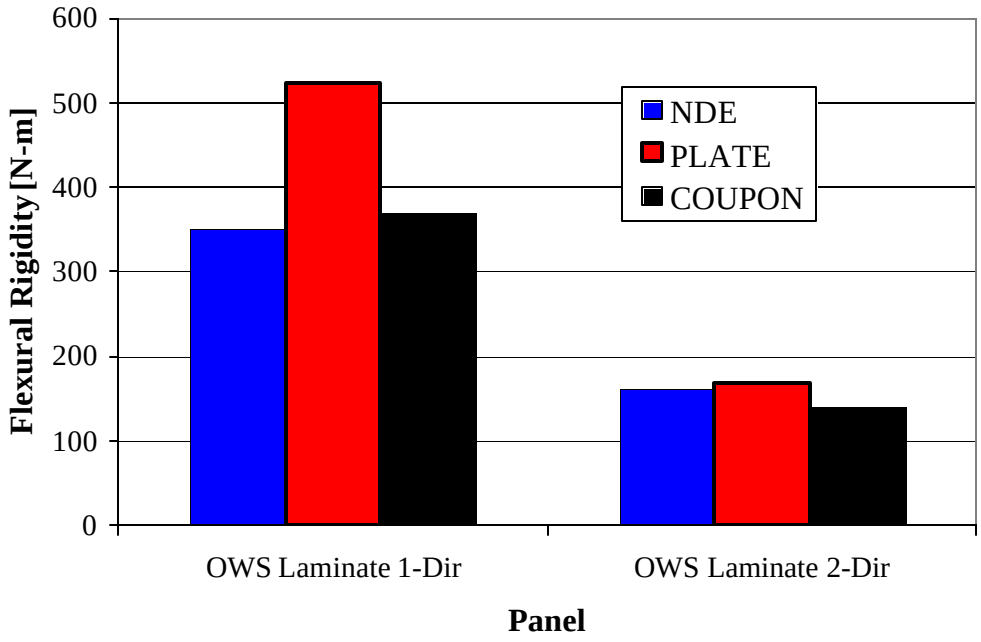

Figure 20: Comparison of NDE results with full plate and coupon mechanical bending tests for panels with a relatively large flexural rigidity

Table 12: Comparison of NDE and mechanical flexural rigidity values

Panel	NDE D_{11} [N-m]	Plate Bending D_{11} [N-m]	Coupon Bending EI/w [N-m]	Difference (NDE-Plate)/Plate
MDF-B	6.26	6.24	6.13	0.3%
MDF-C	7.28	7.08	-	2.8%
MDF-E	7.05	6.45	-	9.3%
MDF-F	7.06	6.08	-	16%
OWS-B 1-dir	16.8	16.6	13.0	1.2%
OWS-B 2-dir	5.46	4.10	3.34	33%
MDF-G	52.4	51.0	-	2.7%
MDF-H	53.7	55.0	57.4	2.4%
MDF Laminate	61.3	60.6	65.1	1.2%
OWS Laminate 1-dir	351	523	369	33%
OWS Laminate 2-dir	161	169	141	4.7%

For all panels, it was not anticipated that the coupon bending and NDE values would exactly agree with the full plate bending tests due to spatial variability in the plate. NDE and coupon testing were only used to inspect a small region in the middle of each plate whereas plate

bending was dependent on the overall properties of the plate. If material differences existed throughout the plate, the overall flexural rigidity of the plate would differ from coupon results. Such differences were observed in MDF-E, MDF-F, and the OWS laminate.

Coupon specimens were taken from the center of the plate coincident with the NDE inspection area; therefore, these values should exhibit close correlation with NDE values. However, the plane stress assumption is violated when coupons are cut from the surrounding plate material. The coupons should have resulted in a slightly lower stiffness. The small inconsistency in stress states between NDE and coupons could explain the differences observed in some panels; however, coupon tests resulted in higher flexural rigidity values than NDE for MDF-H and the MDF Laminate.

One reason for differences between mechanical coupon and full plate bending tests was the use of a different span-to-depth ratio. This would have the largest affect on materials with a high Young's modulus to shear modulus (E/G) ratio. It was observed from NDE testing that OWS exhibited a high E/G ratio (Table 7). Coupon testing resulted in flexural rigidity values well below those obtained from NDE as can be seen in Figure 18 and Table 12. Had a longer span been used, deflection due to shear deformations would have been reduced relative to the bending deflections, thus resulting in a higher value for flexural rigidity.

In past wood research, a load-rate effect has been noted when comparing NDE and mechanical bending results (Halabe *et al.* 1997). However, that effect seems to be negligible when comparing values from full plate bending and plate wave NDE. This could be due to the similarity between mechanical loading configuration and wave propagation where a flexural wave was used for comparison to flexural bending instead of an extensional wave. Although the NDE flexural load rate (dynamic) was much faster than mechanical bending (static), the loading

configurations were similar. Differences in the type of loading could possibly be the primary reason for differences between past NDE research and mechanical testing results. Future research should be conducted to compare NDE and mechanical test results from identical loading configurations instead of citing load-rate effects when a difference exists between NDE and static testing.

Comparisons of axial rigidity obtained from mechanical coupon testing and NDE are presented in Figure 21 and Table 13. Plywood and OWS laminate comparisons were excluded due to violation of the wavelength limit discussed earlier. As can be seen, axial stiffness values obtained from NDE were consistently higher than those obtained from mechanical testing (Table 13). This stiffness difference agrees with previous NDE where the "dynamic loading effect" was cited. Differences in NDE and coupon results could be due to a combination of several reasons including spatial variability, differing stress states, and load rate. Differences between tensile and compressive rigidity could be due to either spatial variability within the plate or differences between compressive and tensile moduli.

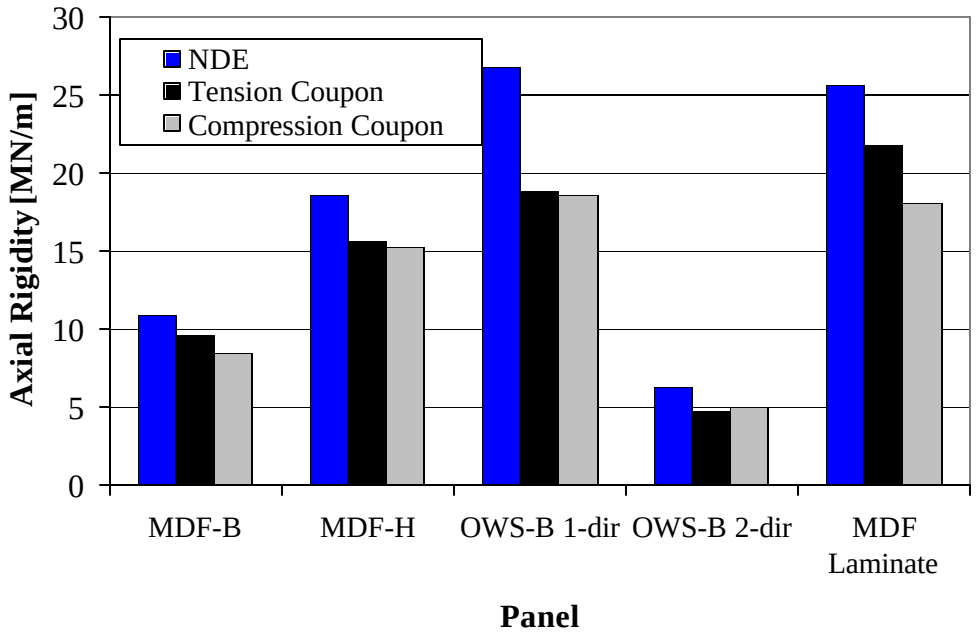

Figure 21: Comparison of NDE and axial mechanical coupon results

Table 13: Comparison of NDE and axial mechanical coupon results

Panel	Mechanical Axial Rigidity EA/w [MN/m]	NDE Axial Rigidity A_{11} [MN/m]	Difference Relative to EA/w
MDF-B	10.0	10.9	12%
OWS-B 1-Dir	16.2	26.7	17%
OWS-B 2-Dir	19.6	6.32	31%
MDF-H	4.95	18.6	26%
MDF Laminate	22.7	25.6	16%

Tensile coupons used to obtain axial rigidity, *EA*, were not taken from a portion of the panel coincident with the NDE inspection region. Any spatial variability within the plate with respect to axial rigidity would present a difference in results. The difference in results could be lower or higher. Axial compression coupons were cut from mechanical bending specimens, which were coincident with the NDE inspection region.

Another inconsistency exists due to the different stress state in coupons versus plates. When the coupons were removed from the plate, the plane stress assumption used to develop

plate wave propagation was violated due to the absence of surrounding material. During testing of the coupons, only a unidirectional state of tensile stress existed when freed from surrounding material and Poisson's effects associated with plane stress stiffness. Using the NDE value for axial plate rigidity, A_{11}, and assuming a Poisson's ratio, ($n = 0.2$), to calculate axial coupon rigidity per unit width, AE/w, the two values may be compared. A reasonable range of values for Poisson's ratio was explored, but only small improvements in agreement between NDE and mechanical testing were observed. These small improvements were not enough to account for the entire difference.

A third possible reason for inconsistencies in NDE and mechanical testing is the difference in load rate between the tests (Halabe *et al*. 1997). Mechanical loading of the coupon specimens was performed with a strain rate of 1.0 percent per minute, whereas extensional plate waves load and unload the material more than a million times faster. Since wood behaves in a viscoelastic manner, different rates of loading will result in different values of Young's modulus. Faster loading will result in higher modulus values. This behavior has been witnessed using stress wave speed as an indicator for Young's modulus in lumber. If the exact load-rate effect were known for each specimen, correction factors could be applied. In this case, it is only speculated that NDE values should produce a higher modulus and thus, after application of a correction factor, values could compare better with mechanical tests.

Comparison of Laminate Properties

Prediction of laminate properties using 3-dimensional classical lamination plate theory (CLT) was performed using two laminates: 1) two-ply MDF and 2) three-ply [0/90/0] OWS. Plane stress stiffness values, Q_{11} and Q_{22}, for the individual lamina were obtained from NDE, used as input for CLT, and compared with NDE and mechanical testing of the final laminate.

Instead of using Young's modulus, E, as input for CLT, the plane stress stiffnesses, Q_{11} and Q_{22}, were back-calculated from the NDE flexural plate rigidity values, D_{11} and D_{22} (Eqns. [8] and [9]). The plane stress stiffnesses were input directly into the effective laminate property matrices (A, B, D) (APPENDIX I, Section B, Eqns. [36] through [39]), which eliminated the need to assume a Poisson's ratio, n, for calculation of Young's modulus. The product of shear correction coefficient and shear modulus, kG, obtained from NDE was used as input to account for shear deformations. By keeping kG together and using the term directly as input for CLT, the need for assuming a shear correction coefficient is eliminated. The plane stress stiffness values for each lamina could also be obtained from the axial panel rigidities, A_{11} and A_{22} (Eqn. [10] and Eqn. [11]); however, it was noted that these values were higher than those obtained from the flexural panel rigidities. The results of CLT from axial rigidity values were primarily used for calculation of laminate axial rigidities, not flexural rigidity. Both the axial and flexural rigidity obtained plane stress stiffnesses were used as input for CLT as indicated in Table 14 and Table 15. The CLT MathCAD™ worksheets for the MDF and OWS laminates are presented in APPENDIX IV.

$$D_{11} = \frac{Q_{11} h^3}{12} \qquad \textbf{[8]}$$

$$D_{22} = \frac{Q_{22} h^3}{12} \qquad \textbf{[9]}$$

$$A_{11} = Q_{11} h \qquad \textbf{[10]}$$

$$A_{22} = Q_{22} h \qquad \textbf{[11]}$$

From CLT, theoretical predictions of A_{11}, A_{22}, D_{11}, D_{22}, A_{44}, and A_{55} were obtained. (Only A_{11}, D_{11}, and A_{55} were obtained for MDF due to its transversely isotropic nature) Results

from CLT as well as NDE and mechanical testing of the entire laminates are presented in Table 14 and Table 15.

MDF Laminate

Table 14: MDF laminate comparison of theory with NDE and mechanical testing

Property	CLT (from D_{11})	CLT (from A_{11})	NDE	Plate Testing	Coupon Testing
A_{11} [MN/m]	18.7	24.6	25.6	-	21.7
D_{11} [N-m]	59.2	-	61.3	60.6	65.1
A_{55} [MN/m]	3.94	-	3.14	-	-

For the MDF laminate, CLT provided an excellent prediction of flexural rigidity, D_{11}, with values differing by only 2.3% relative to full plate bending tests. Any increase in mechanical bending or NDE values versus CLT could be due to adhesive properties, which were neglected in the lamination theory. As discussed earlier, the MDF laminate and solid MDF panel flexural and transverse shear rigidities differed by 10% and 25%, respectively, due to the higher material properties existing in the individual lamina used to fabricate the laminate. CLT accounted for the higher lamina material properties, which were observed with both NDE and full plate bending.

Based on the laminate NDE results, CLT over predicted transverse shear rigidity by 25%, relative to the NDE results. It was speculated that the NDE value would be higher due to adhesive effects. These differences in results could also have been due to inaccurate CLT input from NDE results.

MDF laminate axial rigidity, A_{11}, determined from NDE and full plate testing was much higher than that predicted by CLT. When plane stress stiffness from axial lamina rigidity was used as input into CLT, a higher laminate axial rigidity, A_{11}, was obtained (Table 14), which improved the agreement with mechanical and NDE laminate tests. This superior agreement

suggests that similar plate wave propagation modes are required for accurate comparison between individual lamina and final laminate. For example, plane stress stiffnesses obtained from flexural rigidity of the individual lamina should be used as input for CLT to predict the overall flexural rigidity of the entire laminate. NDE results of axial rigidity were slightly higher than CLT results (approximately 4% relative to NDE results), but this may be attributed to adhesive effects or irregularities resulting from the laminate fabrication.

Coupon testing resulted in a 9% (relative to coupon bending) higher flexural rigidity value than CLT possibly due to spatial variability. A 14% (relative to coupon results) higher axial rigidity was obtained from tensile coupon tests compared with CLT (from D_{11}) results, again likely due to spatial variability. A 13% lower axial rigidity was obtained relative to the CLT (from A_{11}) results, possibly due to load-rate effects inherent in the extensional plate wave. Good agreement (within 4%) was found between the NDE obtained and CLT (from A_{11}) obtained axial rigidity. The latter comparison used results from individual lamina extensional plate wave tests as input for CLT and compared the CLT output with extensional plate wave results for the entire laminate.

OWS Laminate

Table 15: OWS laminate comparison of theory with NDE and mechanical testing

Property	CLT (initial) (from D_{11})	CLT (adjusted) (from D_{11})	CLT (adjusted) (A_{11})	NDE	Plate Testing	Coupon Testing
A_{11} [MN/m]	45.0	48.6	57.5	-	-	39.6
A_{22} [MN/m]	32.7	35.4	41.7	-	-	33.2
D_{11} [N-m]	412	522	-	351	523	369
D_{22} [N-m]	140	177	-	161	169	141
A_{55} [MN/m]	2.45	2.64	-	1.79	-	-
A_{44} [MN/m]	2.09	2.26	-	1.56	-	-

For the OWS laminate, initial results from CLT revealed poor agreements with full plate bending tests (21% and 17% difference D_{11} and D_{22}, respectively). It was noted; however, that the OWS laminate had an overall thickness 8.3% greater than the sum of the lamina. This increase in thickness could have been due to unrecoverable moisture swell from the adhesive. Therefore, initial CLT results of flexural rigidity, under predicted values obtained from full plate bending tests. In an effort to correct the difference in thickness, the overall increase in thickness was calculated, and divided evenly among the individual lamina for use as CLT input. This resulted in much more accurate predictions of overall laminate properties as can be seen in Table 15.

OWS coupon values for flexural rigidity were much lower than expected when compared to results from full plate bending tests and CLT. By accounting for the different stress states (i.e. plane stress versus uni-axial stress) using a range of Poisson's ratios, slight improvements in agreement between results were observed, but not enough to account for the full difference. In addition, consideration of shear deformations would not place the results in complete agreement. Another possible reason for the discrepancy between CLT and coupon tests could be that low quality material or a poor adhesive bond was located in the center region of the laminate. This theory is enforced by the fact that NDE and coupon results (both taken from the same region of the laminate) are similar.

For the OWS laminate, transverse shear rigidity values from CLT did not agree with those obtained from NDE, which was the only measure of shear rigidity available for this research. It is possible that a localize defect or irregularity was present in the center of the OWS laminate panel coincident with the NDE inspection region due a fabrication flaw. This hypothesis was enforced by the fact that flexural plate wave and coupon bending results (both

taken from the center of the panel) were in close agreement (Table 15), whereas the full plate bending and CLT (from D_{11}) results were much higher.

Extensional plate wave rigidity values, A_{11} and A_{22}, were used to calculate plane stress stiffnesses, Q_{11} and Q_{22}, for use as CLT input and resulted in higher axial rigidity values than those obtained using the plane stress stiffness from flexural rigidity values (Table 15). CLT values were significantly higher (45% and 26% for A_{11} and A_{22}, respectively) than coupon results. These differences are consistent with the previous comparisons discussed earlier due to the fact that CLT input was based on NDE obtained values.

Excellent agreement (within 0.2% and 5% for D_{11} and D_{22}, respectively) was found between CLT and full plate bending tests when flexural rigidity values were compared. This is consistent with the MDF laminate comparisons. Based on the results presented here, it is proposed that NDE could be used to accurately obtain individual lamina properties, the results of which could be used as input for CLT. Final laminate properties could then be accurately predicted using CLT as opposed to NDE inspection, which presented difficulties in testing thicker composites.

Defect Detection

A defective laminate was tested according to the methods described earlier. Five phase point locations were tracked and transit times recorded for each location at frequencies of 10, 15, 20, 25, and 30 kHz. Results of the testing for each frequency are presented in APPENDIX III and are summarized here (Table 16). A typical transit time shift plot is presented in Figure 22. A range of frequencies was used to determine which frequencies were most sensitive to delaminations. Findings revealed that lower frequencies were more sensitive to the delamination than higher frequencies. This may be deduced by comparing the shifts in transit time at the

different frequencies (Table 16). This is contrary to other types of ultrasonic NDE where a higher frequency produces a smaller wavelength and thus, is more sensitive to defects.

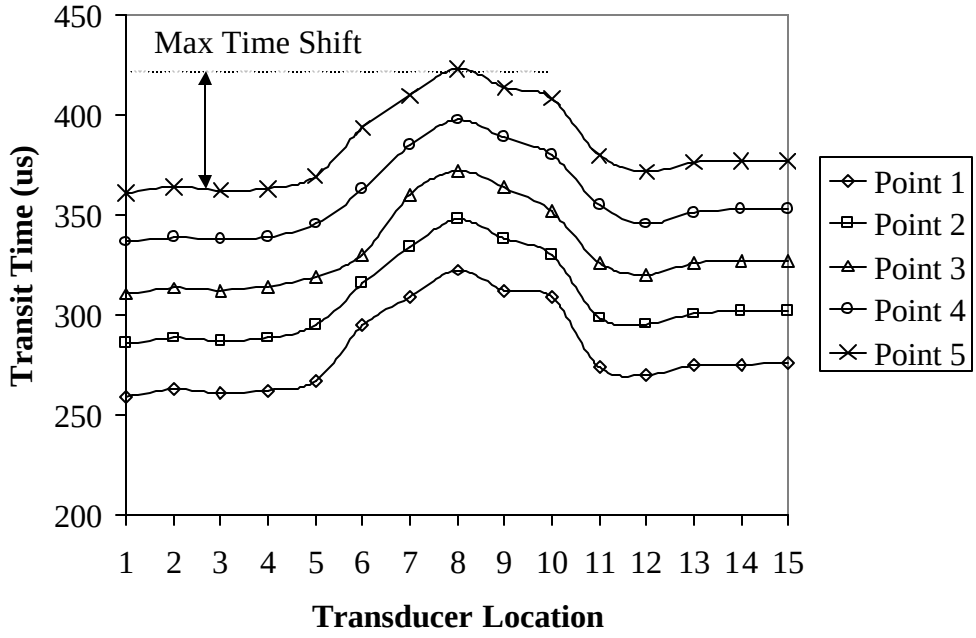

Figure 22: Typical transit time shift of various phase points (Figure 8) within the waveform (maximum time shift is shown)

One explanation for the transit time shift at lower frequencies may reside within the characteristic dispersion curve shape. While the flexural wave is traveling through the solid, defect-free region at a particular frequency, this coincides with a distinct point on the dispersion curve with a specific phase velocity and *fh*. When the wave reaches the defect region, the thickness is reduced and thus, *fh* is reduced. In the case of a two-ply laminate, *fh* is halved. This now corresponds to a different location on the dispersion curve with a different phase velocity. At lower frequencies, the dispersion curve has a steeper slope than at higher frequencies. Therefore, by halving *fh*, the phase velocity is reduced more at lower frequencies than at higher frequencies.

Table 16: Maximum phase point time shifts for defective laminate

Frequency (kHz)	Maximum Phase Point Time Shift (ms)
10	80
15	65
20	60
25	55
30	15

Increased sensitivity in the high frequency range may be increased with more advanced signal processing methods that are not susceptible to user-defined phase points. Due to the nature of the dispersive flexural plate waves, an inaccurate selection of phase points is a potential source of error. Another possible approach would be to use group velocity instead of phase velocity. The use of group velocity would eliminate the need to locate specific phase points with and without defects; however, it would require an accurate calculation of the pulse centroid. Group velocity also varies more in the lower frequency range, which could result in an increase in defect sensitivity. Overall, the flexural plate wave is sensitive to delaminations and has the ability to easily locate these defects.

Technical Feasibility

Based on the results presented in this chapter, the plate wave technique appears to be a technically feasible option for inspection of wood-based composites. Interpretable waveforms were transmitted through the wood-based panels and further signal processing resulted in coherent, reasonable dispersion curves. The theories that govern plate wave propagation were applied and showed good agreement with mechanical results. A fabricated delamination was easily located within a laminated panel. These results indicate that the technique is feasible and with further refinements could be used in a manufacturing quality control scenario.

Comparison of plate wave NDE and mechanical tests revealed that the flexural rigidity was within 5% for most of the thinner panels (less than or equal to 0.64 cm (0.25 in.) thick). Differences between NDE and mechanical results could be attributed to spatial variability within the panels. Due to lack of results from mechanical testing, no firm conclusions could be drawn regarding the accuracy of NDE transverse shear rigidity results. Axial rigidity values from NDE were between 12% and 31% higher than values obtained from tensile coupon tests and between 22% and 41% greater than compressive coupon values. For thicker panels, unreliable and/or indiscernible NDE measurements were obtained due to high attenuation of signals or violation of the assumptions necessary for plate wave propagation.

Using classical lamination plate theory in combination with NDE lamina results, predictions of laminate rigidities were obtained. Flexural rigidity of an oriented wheat strawboard three-ply laminate was predicted to within 1% and 4% of mechanical testing results in the directions parallel and perpendicular to the particle orientation, respectively. Flexural rigidity of a MDF two-ply laminate was predicted to within 2.3% of full plate mechanical bending results.

A 60-mm (2.36-in.) square defect within a laminated MDF panel was successfully located using plate waves. Low frequencies were more sensitive to the defect than higher. Time shifts of 80 μs and 15 μs were observed for flexural plate waves at 10 and 30 kHz, respectively. The defective region was approximately 33% of the entire inspection region; therefore, smaller defects (relative to the inspection region between the transducers) might appear as subtle changes in material properties as opposed to actual defects.

CHAPTER 5: CONCLUSIONS AND RECOMMENDATIONS

Summary

An NDE procedure was developed for using ultrasonic plate waves to determine material properties in wood-based composite panels. A pair of 1-MHz broadband ultrasonic transducers was used to transmit extensional and flexural plate waves through a variety of wood-based and wheat straw panels. Neoprene pads were used to transmit the ultrasonic energy from the face of the transducer into the panels without the need for water-based couplant. Flexural waves were propagated over a frequency range from 5 kHz to 50 kHz using five bursts of a sinusoidal pulse. Extensional waves were propagated at higher frequencies between 35 kHz and 130 kHz. Phase velocities were calculated at each frequency. Dispersion curves were constructed for the flexural plate waves by plotting phase velocities versus the frequency-thickness product. Nonlinear regression was performed to fit the dispersion relationship to the experimental data, from which the flexural and transverse shear panel rigidities were determined. Axial rigidities were calculated directly from extensional plate wave phase velocities.

Conclusions

In order to verify the capability of the plate wave technique setup to determine material properties, an aluminum plate was tested to determine its flexural and transverse shear rigidity values. From the experimentally obtained plate rigidity values, both Young's modulus and shear modulus were calculated to within 1% and 6.5%, respectively, of nominal values for the 6061-T4 aluminum specimen. These results also agree with past plate wave research results on an aluminum plate. Based on these findings, it was concluded that the plate wave setup used in this research was both accurate and repeatable.

After the technique's accuracy was characterized, a variety of wood-based and wheat straw panels were nondestructively and mechanically tested to evaluate the flexural, transverse shear and axial rigidity values. Based on the results of this research, the evaluation of flexural and axial rigidity for thin (less than 6.4 mm thick) wood-based (or natural fiber-based) panels has shown to be technically feasible. Comparison of NDE and mechanical tests revealed that the flexural rigidity was within 5% for most of the thinner panels (less than or equal to 0.64 cm (0.25 in.) thick). Differences between NDE and mechanical results could be attributed to spatial variability within the panels. Due to lack of results from mechanical testing, no firm conclusions could be drawn regarding the accuracy of NDE transverse shear rigidity results. Axial rigidity values from NDE were between 12% and 31% higher than values obtained from tensile coupon tests and between 22% and 41% greater than compressive coupon values. For thicker panels, unreliable and/or indiscernible NDE measurements were obtained due to high attenuation of signals or violation of the wavelength assumption necessary for plate wave propagation.

The 6.4-mm (0.25-in.) limit for plate wave inspection is not a rigid one. This limit is dependent upon material properties, wavelengths, applicable frequencies, and material homogeneity. For this research, the thicker panels that exceeded the 6.4-mm (0.25-in.) thickness limit were laminated and/or heterogeneous (OWS laminate and plywood). Based on these material types alone, the plate wave technique cannot be precluded from applicable testing of all wood-based materials with a thickness greater than 6.4 mm (0.25-in.). To investigate the plate wave technique's ability for inspection of thicker panels, a solid piece of pseudo-homogenous material (e.g. MDF) should be used. Results of these tests could reveal more information for inspection of wood-based composites concerning plate wave thickness limitations.

Using classical lamination plate theory in combination with NDE lamina results, predictions of laminate rigidities were obtained. Flexural rigidity of an oriented wheat strawboard three-ply laminate was predicted to within 1% and 4% of mechanical testing results in the directions parallel and perpendicular to the particle orientation, respectively. Flexural rigidity of a MDF two-ply laminate was predicted to within 2.3% of full plate mechanical bending results.

Based on this research, detection of internal panel delaminations in wood-based laminates appears technically feasible using the plate wave technique. A 60-mm (2.36-in.) square defect within a laminated MDF panel was successfully located using plate waves. Low frequencies were more sensitive to the defect than higher. Time shifts of 80 μs and 15 μs were observed for flexural plate waves at 10 and 30 kHz, respectively. The defective region was approximately 33% of the entire inspection region; therefore, smaller defects (relative to the inspection region between the transducers) might appear as subtle changes in material properties as opposed to actual defects.

Based on the excellent agreement between NDE and mechanical test results for thin panels, inspection of wood-based composites using the plate wave technique is technically feasible. With refinements, the technique could conceivably be used in a process control scenario. Since the technique only requires two transducers (sending and receiving), less equipment is needed compared with the current wood panel NDE systems. In addition, with advanced signal processing, more information is available concerning the panel material properties such as flexural, axial, and transverse shear rigidity. Based on the potential reduction in required equipment and increased information availability, the plate wave technique could be more economically efficient than current wood-based panel NDE systems.

Recommendations

Recommendations for future research include refinements of both equipment and procedures. Air-coupled and/or angled flat frequency response transducers would eliminate the need for coupling pads, but would potentially introduce difficulties regarding impedance mismatch. Higher transmission power would help to cut down on surrounding noise and produce cleaner signals in the highly attenuative wood composites. An amplitude-modulated excitation burst would help to reduce extraneous frequencies at the front and rear of a signal burst resulting in more accurate pinpointing of a particular phase point. The measurement of group velocity instead of phase velocity could possibly help to expedite the determination of material properties by reducing the time required for actual testing.

Group velocity eliminates the need to locate and correctly follow phase points within the transmitted signal. Instead, the centroid of the burst is used to determine group velocity, which is potentially faster than locating phase points. More advanced signal processing algorithms (e.g. wavelet transforms) could be used to quickly determine group velocities of particular frequencies from a burst containing a wide range of frequency content. This would eliminate the large number of signals required to determine phase velocity as was used in this research. However, from the group velocity values, phase velocities would still have to be calculated in order to determine the panel rigidities.

Future research should explore consistent methods for mechanical determination of transverse shear plate rigidity for validation of NDE results. Nondestructive plate wave methods for determining transverse shear rigidity could then be compared to determine the accuracy and reliability. In addition, load configurations and load-rate effects should be researched to determine the physical cause for over prediction of mechanical properties from extensional plate

wave NDE. Using this information, more accurate prediction of axial panel properties could be obtained from NDE.

CHAPTER 6: REFERENCES

Achenbach, J.D. 1973. Wave Propagation in Elastic Solids. North-Holland Publishing Company, Amsterdam.

American Society for Testing and Materials. 1996. Standard test method for compressive properties of rigid plastics. ASTM D 695-96. ASTM, West Conshohocken, PA.

American Society for Testing and Materials. 1997. Standard test methods for flexural properties of unreinforced and reinforced plastics and electrical insulating materials. ASTM D 790-97. ASTM, West Conshohocken, PA.

American Society for Testing and Materials. 1999. Standard methods of static tests of timbers in structural sizes. ASTM D 198-99. ASTM, West Conshohocken, PA.

American Society for Testing and Materials. 2000. Standard Test Method for Tensile Properties of Plastics. ASTM D 638-00. ASTM, West Conshohocken, PA.

Auld, B.A. 1973. Acoustic Fields and Waves in Solids, Vol. I & II. John Wiley & Sons, Inc., New York, NY.

Bar-Cohen, Y. and D.E. Chimenti. 1986. Nondestructive evaluation of composite laminates by leaky Lamb waves. Review of Progress in Quantitative NDE, ed. D.O. Thompson and D.E. Chimenti, Vol. 5B, 1199-206. Plenum Press, New York, NY.

Bray, Don E., and R.K. Stanley. 1997. Nondestructive Evaluation: A Tool in Design, Manufacturing, and Service. CRC Press, New York, NY.

Castaings, M. and P. Cawley. 1996. The generation, propagation, and detection of Lamb waves in plates using air-coupled ultrasonic transducers. The Journal of the Acoustical Society of America 100(5):3070-7.

Chimenti, D.E. 1997. Guided waves in plates and their use in materials characterization. Applied Mechanics Reviews, 50(5):247-84.

Dickens, J.R., D.E. Bray, and D.A. Bender. 1997. Beam profiles in wood from critically refracted longitudinal wave probes. Materials Evaluation 55(6):721-725.

Dickens, J.R., D.A. Bender, and D.E. Bray. 1996. A critical-angle ultrasonic technique for the inspection of wood parallel-to-grain. Wood and Fiber Science 28(3): 380-388.

Gibson, Ronald F. 1994. Principles of Composite Material Mechanics. McGraw-Hill, Inc., New York, NY.

Graff, Karl. 1975. Wave Motion in Elastic Solids. Ohio State University Press.

Guo, N. and P. Cawley. 1993. The interaction of Lamb waves with delaminations in composite laminates. Journal of the Acoustical Society of America 94(4):2240-6

Halabe, Udaya B., Gangadhar M. Bidigalu, Hota V.S. GangaRao, and Robert J. Ross. 1997. Nondestructive evaluation of green wood using stress wave and transverse vibration techniques. Materials Evaluation, 55(9): 1013-8.

Han, Jun-Bo, Jian-Chun Cheng, Tie-Hai Wang, and Yves Berthelot. 1999. Mode analyses of laser-generated transient ultrasonic Lamb waveforms in a composite plate by wavelet transform. Materials Evaluation 57(8):837-40.

Huang, W., S.M. Ziola, J.F. Dorighi, and M.R. Gorman. 1998. Stiffness measurement and defect detection in laminated composites by dry-coupled plate waves. In: Proceedings of SPIE, ed. R.H. Bossi, and D.M. Pepper. March 31- April 2, San Antonio, TX.

Huang, W. 1999. Verbal communication. Digital Wave Corporation, Englewood, CO.

Huggins, L.F. 1983. Analysis and interpretation. Instrumentation and Measurement for Environmental Sciences 2nd ed. B.W. Mitchell, ed. American Society of Agricultural Engineers, St. Joseph, MI.

Karim, M.R., A.K. Mal, and Y. Bar-Cohen. 1990. Determination of the elastic constants of composites through the inversion of leaky Lamb wave data. Review of Progress in Quantitative Nondestructive Evaluation 9A:109-16.

Kolsky, H. 1963. Stress Waves in Solids. Dover Publications, Inc. New York, NY.

Martin, R.W. and D.E. Chimenti. 1987. Signal processing of leaky Lamb wave data for defect imaging in composite laminates. Review of Progress in Quantitative NDE, ed D.O. Thompson and D.E. Chimenti, Vol. 6A, 815-24. Plenum Press, New York, NY.

Mindlin, R. D. 1951. Influence of rotatory inertia and shear on flexural motions of isotropic, elastic plates. Journal of Applied Physics 18: 31-8.

Nayfeh, Adnan H. 1995. Wave Propagation in Layered Anisotropic Media: with applications to composites. Elsevier, New York.

Rodgers, J.M., A.T. Green, and S.W. Borup. 1991. Acousto-ultrasonic measurement of internal bond strength in composite wood products. Materials Evaluation 49(5):566-571.

Rogers, W.P. 1995. Elastic property measurement using Rayleigh-Lamb waves. Research in Nondestructive Evaluation 6:185-208.

Rose, W.R. 1999. Ultrasonic Waves in Solid Media. Cambridge University Press, Cambridge, UK.

Rose, W.R., S.I. Rokhlin, and L. Alder. 1987. Evaluation of anisotropic properties of graphite-epoxy composites using Lamb waves. Review of Progress in Quantitative Nondestructive Evaluation 6B:1111-8.

Ross, Robert J. and Roy F. Pellerin. 1988. NDE of wood-based composites with longitudinal stress waves. Forest Products Journal 38(5):39-45.

Ross, Robert J. and Roy F. Pellerin. 1991. Nondestructive evaluation of wood - past, present, and future. Proceedings of the Fourth International Symposium on Nondestructive Characterization of Materials. Plenum Press. New York, NY.

Ross, Robert J, and Roy F. Pellerin. 1994. Nondestructive testing for assessing wood members in structures: a review, General Technical Report FPL-GTR-70 (Rev.). USDA Forest Service, Forest Products Laboratory, Madison, WI.

Ross, Robert J., Roy F. Pellerin, Norbert Volny, William W. Salsig, and Robert H. Falk. 1999. Inspection of timber bridges using stress wave timing nondestructive evaluation tools, General Technical Report FPL-GTR-114. USDA Forest Products Laboratory, Madison, WI.

Stiffler, R.C. 1986. Wave Propagation in Composite Plates. Ph.D. Dissertation, College of Engineering, Virginia Polytechnic Institute and State University, Blacksburg, VA.

Tang, B. 1988. Lamb Wave Propagation in Laminated Composite Plates. Ph.D. Dissertation. College of Engineering, Virginia Polytechnic Institute and State University, Blacksburg, VA.

Tang, B. and E.G. Henneke II. 1989a. Lamb wave monitoring of axial stiffness reduction of laminated composite plates. Materials Evaluation 47(8):928-32.

Tang, B. and E.G. Henneke II. 1989b. Long wavelength approximation for Lamb wave characterization of composites laminates. Research in Nondestructive Evaluation 1:51-64.

Tang, B., E.G. Henneke II, R.C. Stiffler. 1988. Low Frequency Flexural Wave Propagation in Laminated Composite Plates. Acousto-Ultrasonics: Theory and Application, ed. J.C. Duke Jr. Plenum Press, New York, NY. 45-65.

Tucker, J.L., D.A. Bender, and D.E. Bray. 1997. Angled-beam ultrasonic evaluation of particleboard. Proceedings of Workshop on Nondestructive Testing of Panel Products, pp. 61-67, Llandudno, UK, October 11, 1997.

Viktorov, Igor Aleksandrovich. 1967. Rayleigh and Lamb Waves: Physical Theory and Applications. Plenum Press, New York, NY.

Yang, P. Constance, Charles H. Norris, and Yehuda Stavsky. 1966. Elastic wave propagation in heterogeneous plates. International Journal of Solids and Structures 2: 665-84.

APPENDIX I. DERIVATION OF SHEAR DEFORMATION LAMINATED PLATE WAVE THEORY

The derivation of dispersion relations for plate waves in laminated composite plates is somewhat lengthy, but can be broken into three distinct parts: elasticity, lamination theory, and plate wave propagation theory. Each part of the derivation follows well-established theories that have been experimentally verified. Several material and laminate geometry assumptions are made along the way and are stated when they become relevant to the derivation. The entire derivation is based upon Mindlin plate theory, which takes into account the transverse shear deformations and rotational inertia normally neglected in Kirchoff plate theory. The inclusion of transverse shear deformations is especially needed for materials with a high ratio of Young's modulus to shear modulus.

Section A. Elasticity

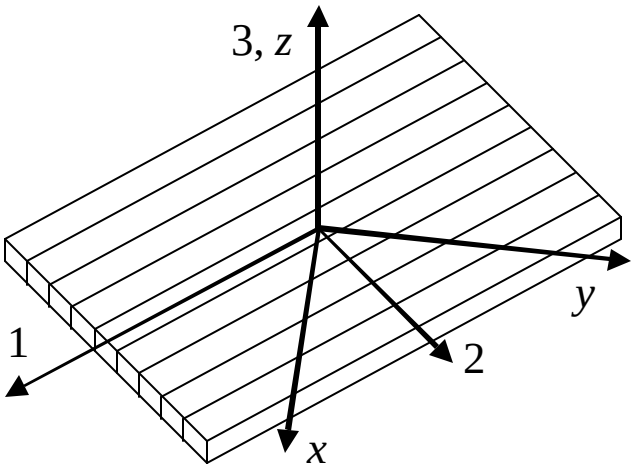

Figure 23: Material directions

The material illustrated in Figure 23 must be described mathematically. Therefore, the general elasticity approach is used with an assumption of an orthotropic material.

$$\underline{g}_1 = \underline{\underline{S}}\,\underline{s}_1 \qquad \textbf{[12]}$$

$\underline{g}_1$ strain tensor in the principal material directions

$\underline{\underline{S}}$ compliance matrix

$\underline{s}_1$ stress tensor in the principal material directions

Since the stress and strain tensors are symmetric, the familiar compacted notation may be used resulting in the familiar forms.

$$\underline{g}_1 = \begin{Bmatrix} e_1 \\ e_2 \\ e_3 \\ g_{23} \\ g_{31} \\ g_{12} \end{Bmatrix} \quad \underline{\underline{S}} = \begin{bmatrix} \frac{1}{E_1} & \frac{-n_{12}}{E_1} & \frac{-n_{13}}{E_1} & 0 & 0 & 0 \\ \frac{-n_{21}}{E_2} & \frac{1}{E_2} & \frac{-n_{23}}{E_2} & 0 & 0 & 0 \\ \frac{-n_{31}}{E_3} & \frac{-n_{32}}{E_3} & \frac{1}{E_3} & 0 & 0 & 0 \\ 0 & 0 & 0 & \frac{1}{G_{23}} & 0 & 0 \\ 0 & 0 & 0 & 0 & \frac{1}{G_{31}} & 0 \\ 0 & 0 & 0 & 0 & 0 & \frac{1}{G_{12}} \end{bmatrix} \quad \underline{s}_1 = \begin{Bmatrix} s_1 \\ s_2 \\ s_3 \\ t_{23} \\ t_{31} \\ t_{12} \end{Bmatrix} \qquad \textbf{[13]}$$

E_i Young's modulus in the i-direction
G_{ij} shear modulus in the i-j plane
n_{ij} Poisson's ratio (negative of the transverse strain in the j-direction over the strain in the i-direction when stress is applied in the i-direction)

Due to the plate-like geometry, the 6 by 6 compliance matrix, $\underline{\underline{S}}$, may be reduced to a 5 by 5, which is the two-dimensional plane stress compliance matrix including transverse shear stresses.

$$\underline{g}_1 = \begin{Bmatrix} e_1 \\ e_2 \\ g_{23} \\ g_{31} \\ g_{12} \end{Bmatrix} \quad \underline{\underline{S}} = \begin{bmatrix} \frac{1}{E_1} & \frac{-n_{12}}{E_1} & 0 & 0 & 0 \\ \frac{-n_{21}}{E_2} & \frac{1}{E_2} & 0 & 0 & 0 \\ 0 & 0 & \frac{1}{G_{23}} & 0 & 0 \\ 0 & 0 & 0 & \frac{1}{G_{31}} & 0 \\ 0 & 0 & 0 & 0 & \frac{1}{G_{12}} \end{bmatrix} \quad \underline{s}_1 = \begin{Bmatrix} s_1 \\ s_2 \\ t_{23} \\ t_{31} \\ t_{12} \end{Bmatrix} \qquad \textbf{[14]}$$

Inverting the compliance matrix and assuming a plane stress state (Achenbach 1973), the plane stress stiffness matrix, $\underline{\underline{Q}}$, is obtained with the added transverse shear terms.

$$\underline{\underline{Q}} = \underline{\underline{S}}^{-1} \qquad \underline{\sigma}_1 = \underline{\underline{Q}}\,\underline{\varepsilon}_1 \qquad \underline{\underline{Q}} = \begin{bmatrix} \frac{E_1}{1-\nu_{12}\nu_{21}} & \frac{E_1\nu_{21}}{1-\nu_{12}\nu_{21}} & 0 & 0 & 0 \\ \frac{E_2\nu_{12}}{1-\nu_{12}\nu_{21}} & \frac{E_2}{1-\nu_{12}\nu_{21}} & 0 & 0 & 0 \\ 0 & 0 & G_{23} & 0 & 0 \\ 0 & 0 & 0 & G_{31} & 0 \\ 0 & 0 & 0 & 0 & G_{12} \end{bmatrix} \qquad \textbf{[15]}$$

The properties can be obtained for any arbitrary x-y coordinate system by using the transformation matrix, $\underline{\underline{T}}$, in conjunction with the stiffness matrix, $\underline{\underline{Q}}$, to obtain the transformed stiffness matrix, $\underline{\underline{\overline{Q}}}$(Q-bar). If a lamination layer is oriented in the 0-degree direction, then the transformed stiffness matrix $\underline{\underline{\overline{Q}}}$ is simply equal to the stiffness matrix $\underline{\underline{Q}}$.

$$\underline{\sigma}_x = \underline{\underline{\overline{Q}}}\,\underline{\varepsilon}_x \qquad \underline{\underline{\overline{Q}}} = \underline{\underline{T}}^{-1}\underline{\underline{Q}}\,\underline{\underline{T}}^{-T} \qquad \underline{\underline{T}} = \begin{bmatrix} c^2 & s^2 & 0 & 0 & 2cs \\ s^2 & c^2 & 0 & 0 & -2cs \\ 0 & 0 & c & s & 0 \\ 0 & 0 & -s & c & 0 \\ -cs & cs & 0 & 0 & c^2-s^2 \end{bmatrix} \qquad \textbf{[16]}$$

c cosine of angle between x-axis and 1-direction
s sine of angle between x-axis and 1-direction
$\underline{\varepsilon}_x$ strain tensor in the transformed material direction
$\underline{\sigma}_x$ stress tensor in the transformed material direction

Finally, the two-dimensional stress-strain relation including transverse shear deformation is achieved.

$$\begin{Bmatrix} \sigma_x \\ \sigma_y \\ \tau_{yz} \\ \tau_{xz} \\ \tau_{xy} \end{Bmatrix} = \begin{bmatrix} \overline{Q_{11}} & \overline{Q_{12}} & 0 & 0 & \overline{Q_{16}} \\ \overline{Q_{21}} & \overline{Q_{22}} & 0 & 0 & \overline{Q_{26}} \\ 0 & 0 & \overline{Q_{44}} & \overline{Q_{45}} & 0 \\ 0 & 0 & \overline{Q_{54}} & \overline{Q_{55}} & 0 \\ \overline{Q_{61}} & \overline{Q_{62}} & 0 & 0 & \overline{Q_{66}} \end{bmatrix} \begin{Bmatrix} \varepsilon_x \\ \varepsilon_y \\ \gamma_{yz} \\ \gamma_{xz} \\ \gamma_{xy} \end{Bmatrix} \qquad \textbf{[17]}$$

$\overline{Q}_{ij}$ i,j = 1, 2, 6 plane stress stiffnesses
$\overline{Q}_{ij}$ i,j = 4, 5 transverse shear stiffnesses

Section B. Lamination theory

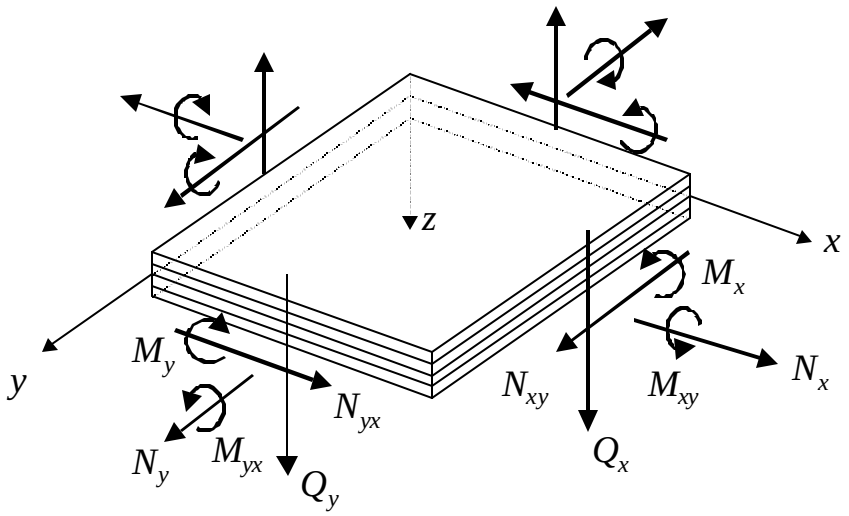

Figure 24: Laminate with applied surface tractions

When several layers (lamina, plies) of material are stacked and bonded together to form a single piece (laminate), the effective properties of the piece are functions of the individual lamina and the sequence in which they were stacked. Lamination theory takes into account the laminate geometry and individual material properties and represents the entire laminate with a set of effective stiffnesses. The assumptions that underlie Mindlin plate theory (shear deformable plate) are as follows (Gibson 1994):

1) The plate consists of orthotropic lamina bonded together, with the principal material axes of the orthotropic lamina oriented along arbitrary directions with respect to the *xy* axes.
2) The thickness of the laminate, *h*, is much smaller than the length along the plate edges.
3) The displacements, *u*, *v*, and *w*, are small compared with the plate thickness.
4) The in-plane strains, e_x, e_y, and g_{xy}, are small compared with unity.
5) The transverse normal strain e_z is negligible.
6) Each lamina obeys Hooke's law.
7) The plate thickness, *h*, is constant.
8) Transverse shear stresses, t_{xz} and t_{yz}, vanish on the plate surfaces defined by $z = \pm h/2$

The assumed displacement field for a Mindlin plate (Yang *et al*. 1966) is as follows.

$$\begin{aligned} u &= u_0(x,y,t) + z\,a(x,y,t) \\ v &= v_0(x,y,t) + z\,b(x,y,t) \\ w &= w(x,y,t) \end{aligned} \qquad \textbf{[18]}$$

The variables, *u*, *v*, and *w*, represent the displacements in the *x*, *y*, and *z*-directions, respectively. Midplane displacements are noted by u_0 and v_0 whereas the rotations are represented by a and b.

Note that a and b are not assumed as functions of w. The strain-displacement relations can then be written in terms of the assumed displacement field.

$$e_x = \frac{\partial u}{\partial x} = \frac{\partial u_0}{\partial x} + z\frac{\partial a}{\partial x}$$

$$e_y = \frac{\partial v}{\partial y} = \frac{\partial v_0}{\partial y} + z\frac{\partial b}{\partial y}$$

$$e_z = \frac{\partial w}{\partial z}$$

$$g_{xz} = 2e_{xz} = 2\left(\frac{1}{2}\right)\left(\frac{\partial u}{\partial z} + \frac{\partial w}{\partial x}\right) = a + \frac{\partial w}{\partial x} \qquad \textbf{[19]}$$

$$g_{yz} = 2e_{yz} = 2\left(\frac{1}{2}\right)\left(\frac{\partial v}{\partial z} + \frac{\partial w}{\partial y}\right) = b + \frac{\partial w}{\partial y}$$

$$g_{xy} = 2e_{xy} = 2\left(\frac{1}{2}\right)\left(\frac{\partial u}{\partial y} + \frac{\partial v}{\partial x}\right) = \frac{\partial u_0}{\partial y} + \frac{\partial v_0}{\partial x} + z\left(\frac{\partial a}{\partial y} + \frac{\partial b}{\partial x}\right)$$

The force and moment resultants (per unit length) may be defined according to Figure 24.

$$N_x = \int_{-h/2}^{h/2} s_x\,dz = \sum_{k=1}^{N}\left\{\int_{z_{k-1}}^{z_k} (s_x)_k\,dz\right\} \qquad \textbf{[20]}$$

$$N_y = \int_{-h/2}^{h/2} s_y\,dz = \sum_{k=1}^{N}\left\{\int_{z_{k-1}}^{z_k} (s_y)_k\,dz\right\} \qquad \textbf{[21]}$$

$$N_{xy} = \int_{-h/2}^{h/2} t_{xy}\,dz = \sum_{k=1}^{N}\left\{\int_{z_{k-1}}^{z_k} (t_{xy})_k\,dz\right\} \qquad \textbf{[22]}$$

$$M_x = \int_{-h/2}^{h/2} s_x\,z\,dz = \sum_{k=1}^{N}\left\{\int_{z_{k-1}}^{z_k} (s_x)_k\,z\,dz\right\} \qquad \textbf{[23]}$$

$$M_y = \int_{-h/2}^{h/2} s_y\,z\,dz = \sum_{k=1}^{N}\left\{\int_{z_{k-1}}^{z_k} (s_y)_k\,z\,dz\right\} \qquad \textbf{[24]}$$

$$M_{xy} = \int_{-h/2}^{h/2} t_{xy}\,z\,dz = \sum_{k=1}^{N}\left\{\int_{z_{k-1}}^{z_k} (t_{xy})_k\,z\,dz\right\} \qquad \textbf{[25]}$$

$$Q_x = \int_{-h/2}^{h/2} t_{xz}\, dz = \sum_{k=1}^{N} \left\{ \int_{z_{k-1}}^{z_k} \left(t_{xz}\right)_k dz \right\} \qquad \textbf{[26]}$$

$$Q_y = \int_{-h/2}^{h/2} t_{yz}\, dz = \sum_{k=1}^{N} \left\{ \int_{z_{k-1}}^{z_k} \left(t_{yz}\right)_k dz \right\} \qquad \textbf{[27]}$$

Substituting the expressions for stress (Eqn. [17]) and the strain field (Eqn. [19]), the force and moment resultants (Eqns. [20] through [27]) take on the following forms.

$$N_x = \sum_{k=1}^{N} \int_{-h/2}^{h/2} \left\{ \left(\overline{Q}_{11}\right)_k \left(\frac{\partial u_0}{\partial x} + z\frac{\partial a}{\partial x} \right) + \left(\overline{Q}_{12}\right)_k \left(\frac{\partial v_0}{\partial y} + z\frac{\partial b}{\partial y} \right) + \left(\overline{Q}_{16}\right)_k \left[\frac{\partial u_0}{\partial y} + \frac{\partial v_0}{\partial x} + z\left(\frac{\partial a}{\partial y} + \frac{\partial b}{\partial x} \right) \right] \right\} dz \qquad \textbf{[28]}$$

$$N_y = \sum_{k=1}^{N} \int_{-h/2}^{h/2} \left\{ \left(\overline{Q}_{21}\right)_k \left(\frac{\partial u_0}{\partial x} + z\frac{\partial a}{\partial x} \right) + \left(\overline{Q}_{22}\right)_k \left(\frac{\partial v_0}{\partial y} + z\frac{\partial b}{\partial y} \right) + \left(\overline{Q}_{26}\right)_k \left[\frac{\partial u_0}{\partial y} + \frac{\partial v_0}{\partial x} + z\left(\frac{\partial a}{\partial y} + \frac{\partial b}{\partial x} \right) \right] \right\} dz \qquad \textbf{[29]}$$

$$N_{xy} = \sum_{k=1}^{N} \int_{-h/2}^{h/2} \left\{ \left(\overline{Q}_{61}\right)_k \left(\frac{\partial u_0}{\partial x} + z\frac{\partial a}{\partial x} \right) + \left(\overline{Q}_{62}\right)_k \left(\frac{\partial v_0}{\partial y} + z\frac{\partial b}{\partial y} \right) + \left(\overline{Q}_{66}\right)_k \left[\frac{\partial u_0}{\partial y} + \frac{\partial v_0}{\partial x} + z\left(\frac{\partial a}{\partial y} + \frac{\partial b}{\partial x} \right) \right] \right\} dz \qquad \textbf{[30]}$$

$$M_x = \sum_{k=1}^{N} \int_{-h/2}^{h/2} \left\{ \left(\overline{Q}_{11}\right)_k \left(\frac{\partial u_0}{\partial x} + z\frac{\partial a}{\partial x} \right) + \left(\overline{Q}_{12}\right)_k \left(\frac{\partial v_0}{\partial y} + z\frac{\partial b}{\partial y} \right) + \left(\overline{Q}_{16}\right)_k \left[\frac{\partial u_0}{\partial y} + \frac{\partial v_0}{\partial x} + z\left(\frac{\partial a}{\partial y} + \frac{\partial b}{\partial x} \right) \right] \right\} z\, dz \qquad \textbf{[31]}$$

$$M_y = \sum_{k=1}^{N} \int_{-h/2}^{h/2} \left\{ \left(\overline{Q}_{21}\right)_k \left(\frac{\partial u_0}{\partial x} + z\frac{\partial a}{\partial x} \right) + \left(\overline{Q}_{22}\right)_k \left(\frac{\partial v_0}{\partial y} + z\frac{\partial b}{\partial y} \right) + \left(\overline{Q}_{26}\right)_k \left[\frac{\partial u_0}{\partial y} + \frac{\partial v_0}{\partial x} + z\left(\frac{\partial a}{\partial y} + \frac{\partial b}{\partial x} \right) \right] \right\} z\, dz \qquad \textbf{[32]}$$

$$M_{xy} = \sum_{k=1}^{N} \int_{-h/2}^{h/2} \left\{ \left(\overline{Q}_{61}\right)_k \left(\frac{\partial u_0}{\partial x} + z\frac{\partial a}{\partial x} \right) + \left(\overline{Q}_{62}\right)_k \left(\frac{\partial v_0}{\partial y} + z\frac{\partial b}{\partial y} \right) + \left(\overline{Q}_{66}\right)_k \left[\frac{\partial u_0}{\partial y} + \frac{\partial v_0}{\partial x} + z\left(\frac{\partial a}{\partial y} + \frac{\partial b}{\partial x} \right) \right] \right\} z\, dz \qquad \textbf{[33]}$$

$$Q_x = \sum_{k=1}^{N} \int_{-h/2}^{h/2} \left\{ \left(\overline{Q}_{54}\right)_k \left(b + \frac{\partial w}{\partial y} \right) + \left(\overline{Q}_{55}\right)_k \left(a + \frac{\partial w}{\partial x} \right) \right\} dz \qquad \textbf{[34]}$$

$$Q_y = \sum_{k=1}^{N} \int_{-h/2}^{h/2} \left\{ \left(\overline{Q}_{44}\right)_k \left(b + \frac{\partial w}{\partial y} \right) + \left(\overline{Q}_{45}\right)_k \left(a + \frac{\partial w}{\partial x} \right) \right\} dz \qquad \textbf{[35]}$$

In accordance with lamination theory, the effective laminate property matrices are defined.

A	effective extensional laminate stiffness matrix
B	effective extensional-flexural coupling laminate stiffness matrix
D	effective flexural laminate stiffness matrix
z_{k-1}	distance from x-y plane (z = 0) to bottom of lamina k
z_k	distance from x-y plane (z = 0) to top of lamina k

K_i, K_j shear correction factors due to the assumption of constant transverse shear stress throughout the laminate thickness

$$A_{ij} = \sum_{k=1}^{N} \left(\overline{Q}_{ij}\right)_k \left(z_k - z_{k-1}\right) \qquad i, j = 1, 2, 6 \qquad \textbf{[36]}$$

$$A_{ij} = K_i K_j \sum_{k=1}^{N} \left(\overline{Q}_{ij}\right)_k \left(z_k - z_{k-1}\right) \qquad i, j = 4, 5 \qquad \textbf{[37]}$$

$$B_{ij} = \frac{1}{2} \sum_{k=1}^{N} \left(\overline{Q}_{ij}\right)_k \left(z_k{}^2 - z_{k-1}{}^2\right) \qquad i, j = 1, 2, 6 \qquad \textbf{[38]}$$

$$D_{ij} = \frac{1}{3} \sum_{k=1}^{N} \left(\overline{Q}_{ij}\right)_k \left(z_k{}^3 - z_{k-1}{}^3\right) \qquad i, j = 1, 2, 6 \qquad \textbf{[39]}$$

Equations [28] through [35] may be rewritten using the effective laminate stiffnesses, thereby eliminating the integrals and summations.

$$N_x = A_{11} \frac{\partial u_0}{\partial x} + A_{12} \frac{\partial v_o}{\partial y} + A_{16} \left(\frac{\partial u_0}{\partial y} + \frac{\partial v_o}{\partial x} \right) + B_{11} \frac{\partial a}{\partial x} + B_{12} \frac{\partial b}{\partial y} + B_{16} \left(\frac{\partial a}{\partial y} + \frac{\partial b}{\partial x} \right) \qquad \textbf{[40]}$$

$$N_y = A_{12} \frac{\partial u_0}{\partial x} + A_{22} \frac{\partial v_o}{\partial y} + A_{26} \left(\frac{\partial u_0}{\partial y} + \frac{\partial v_o}{\partial x} \right) + B_{12} \frac{\partial a}{\partial x} + B_{22} \frac{\partial b}{\partial y} + B_{26} \left(\frac{\partial a}{\partial y} + \frac{\partial b}{\partial x} \right) \qquad \textbf{[41]}$$

$$N_{xy} = A_{16} \frac{\partial u_0}{\partial x} + A_{26} \frac{\partial v_o}{\partial y} + A_{66} \left(\frac{\partial u_0}{\partial y} + \frac{\partial v_o}{\partial x} \right) + B_{16} \frac{\partial a}{\partial x} + B_{26} \frac{\partial b}{\partial y} + B_{66} \left(\frac{\partial a}{\partial y} + \frac{\partial b}{\partial x} \right) \qquad \textbf{[42]}$$

$$M_x = B_{11} \frac{\partial u_0}{\partial x} + B_{12} \frac{\partial v_o}{\partial y} + B_{16} \left(\frac{\partial u_0}{\partial y} + \frac{\partial v_o}{\partial x} \right) + D_{11} \frac{\partial a}{\partial x} + D_{12} \frac{\partial b}{\partial y} + D_{16} \left(\frac{\partial a}{\partial y} + \frac{\partial b}{\partial x} \right) \qquad \textbf{[43]}$$

$$M_y = B_{12} \frac{\partial u_0}{\partial x} + B_{22} \frac{\partial v_o}{\partial y} + B_{26} \left(\frac{\partial u_0}{\partial y} + \frac{\partial v_o}{\partial x} \right) + D_{12} \frac{\partial a}{\partial x} + D_{22} \frac{\partial b}{\partial y} + D_{26} \left(\frac{\partial a}{\partial y} + \frac{\partial b}{\partial x} \right) \qquad \textbf{[44]}$$

$$M_{xy} = B_{16} \frac{\partial u_0}{\partial x} + B_{26} \frac{\partial v_o}{\partial y} + B_{66} \left(\frac{\partial u_0}{\partial y} + \frac{\partial v_o}{\partial x} \right) + D_{16} \frac{\partial a}{\partial x} + D_{26} \frac{\partial b}{\partial y} + D_{66} \left(\frac{\partial a}{\partial y} + \frac{\partial b}{\partial x} \right) \qquad \textbf{[45]}$$

$$Q_y = A_{44} \left(b + \frac{\partial w}{\partial y} \right) + Q_{45} \left(a + \frac{\partial w}{\partial x} \right) \qquad \textbf{[46]}$$

$$Q_x = A_{45} \left(b + \frac{\partial w}{\partial y} \right) + Q_{55} \left(a + \frac{\partial w}{\partial x} \right) \qquad \textbf{[47]}$$

Equations [40] through [47] can be rewritten in the familiar matrix form.

$$\begin{Bmatrix} N_x \\ N_y \\ Q_y \\ Q_x \\ N_{xy} \\ M_x \\ M_y \\ M_{xy} \end{Bmatrix} = \begin{bmatrix} A_{11} & A_{12} & 0 & 0 & A_{16} & B_{11} & B_{12} & B_{16} \\ A_{12} & A_{22} & 0 & 0 & A_{26} & B_{12} & B_{22} & B_{26} \\ 0 & 0 & A_{44} & A_{45} & 0 & 0 & 0 & 0 \\ 0 & 0 & A_{54} & A_{55} & 0 & 0 & 0 & 0 \\ A_{16} & A_{26} & 0 & 0 & A_{66} & B_{16} & B_{26} & B_{66} \\ B_{11} & B_{12} & 0 & 0 & B_{16} & D_{11} & D_{12} & D_{16} \\ B_{12} & B_{22} & 0 & 0 & B_{26} & D_{12} & D_{22} & D_{26} \\ B_{16} & B_{26} & 0 & 0 & B_{66} & D_{16} & D_{26} & D_{66} \end{bmatrix} \begin{Bmatrix} \partial u_0/\partial x \\ \partial v_0/\partial y \\ b + \partial w/\partial y \\ a + \partial w/\partial x \\ \partial u_0/\partial y + \partial v_0/\partial x \\ \partial a/\partial x \\ \partial b/\partial y \\ \partial a/\partial y + \partial b/\partial x \end{Bmatrix} \qquad \textbf{[48]}$$

Section C. Plate wave propagation theory

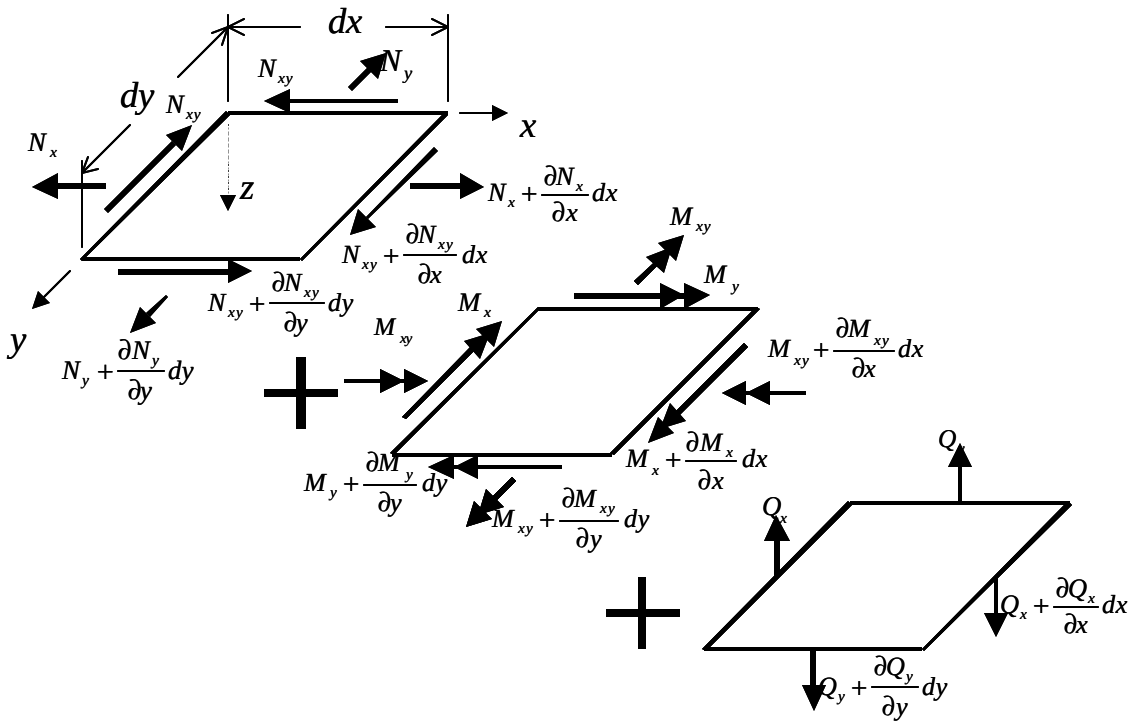

Figure 25: Differential plate element with applied surface tractions

In order to apply plate wave propagation theory to laminates, the wavelength must be much larger than the laminate thickness ($l >> h$). With this condition met, the equations of motion can be written according to Figure 25 taking only surface tractions and inertia into account.

$$\partial N_x/\partial x + \partial N_{xy}/\partial y = \overline{r}\,\partial^2 u_0/\partial t^2 + R\,\partial^2 a/\partial t^2 \qquad \textbf{[49]}$$

$$\partial N_{xy}/\partial x + \partial N_y/\partial y = \overline{r}\,\partial^2 v_0/\partial t^2 + R\,\partial^2 b/\partial t^2 \qquad \textbf{[50]}$$

$$\partial Q_x/\partial x + \partial Q_y/\partial y = \overline{r}\,\partial^2 w/\partial t^2 \qquad \textbf{[51]}$$

$$\partial M_x/\partial x + \partial M_{xy}/\partial y - Q_x = R\,\partial^2 u_0/\partial t^2 + I\,\partial^2 a/\partial t^2 \qquad \textbf{[52]}$$

$$\partial M_{xy}/\partial x + \partial M_y/\partial y - Q_y = R\,\partial^2 v_0/\partial t^2 + I\,\partial^2 b/\partial t^2 \qquad \textbf{[53]}$$

$$\overline{r} = \int_{-h/2}^{h/2} r\,dz \qquad R = \int_{-h/2}^{h/2} r\,z\,dz \qquad I = \int_{-h/2}^{h/2} r\,z^2\,dz \qquad \textbf{[54]}$$

$\overline{r}$ effective laminate mass density
R normal-rotational inertia coupling coefficient
I rotational inertia coefficient
r mass density

Substituting the expressions defined in Eqn. [48] into the equations of motion, Eqn. [49] through Eqn.[53], the following lengthy expressions result.

$$\begin{aligned} &A_{11}\partial^2 u_0/\partial x^2 + 2A_{16}\,\partial^2 u_0/\partial x\partial y + A_{66}\,\partial^2 u_0/\partial y^2 + A_{16}\,\partial^2 v_0/\partial x^2 \\ &+ (A_{12}+A_{66})\partial^2 v_0/\partial x\partial y + A_{26}\,\partial^2 v_0/\partial y^2 + B_{11}\,\partial^2 a/\partial x^2 + 2B_{16}\,\partial^2 a/\partial x\partial y \\ &+ B_{66}\,\partial^2 a/\partial y^2 + B_{16}\,\partial^2 b/\partial x^2 + (B_{12}+B_{66})\partial^2 b/\partial x\partial y + B_{26}\,\partial^2 b/\partial y^2 \\ &\quad = \overline{r}\,\partial^2 u_0/\partial t^2 + R\,\partial^2 a/\partial t^2 \end{aligned} \qquad \textbf{[55]}$$

$$\begin{aligned} &A_{16}\partial^2 u_0/\partial x^2 + (A_{12}+A_{66})\partial^2 u_0/\partial x\partial y + A_{26}\,\partial^2 u_0/\partial y^2 + A_{66}\,\partial^2 v_0/\partial x^2 \\ &+ 2A_{26}\,\partial^2 v_0/\partial x\partial y + A_{22}\,\partial^2 v_0/\partial y^2 + B_{16}\,\partial^2 a/\partial x^2 + (B_{12}+B_{66})\partial^2 a/\partial x\partial y \\ &+ B_{26}\,\partial^2 a/\partial y^2 + B_{66}\,\partial^2 b/\partial x^2 + 2B_{26}\,\partial^2 b/\partial x\partial y + B_{22}\,\partial^2 b/\partial y^2 \\ &\quad = \overline{r}\,\partial^2 v_0/\partial t^2 + R\,\partial^2 b/\partial t^2 \end{aligned} \qquad \textbf{[56]}$$

$$\begin{aligned} &A_{55}(\partial a/\partial x + \partial^2 w/\partial x^2) + A_{45}(\partial a/\partial y + \partial b/\partial x + 2\partial^2 w/\partial x\partial y) \\ &+ A_{44}(\partial b/\partial y + \partial^2 w/\partial y^2) = \overline{r}\,\partial^2 w/\partial t^2 \end{aligned} \qquad \textbf{[57]}$$

$$
\begin{aligned}
&B_{11}\,\partial^2 u_0/\partial x^2 + 2\,B_{16}\,\partial^2 u_0/\partial x\partial y + B_{66}\,\partial^2 u_0/\partial y^2 + B_{16}\,\partial^2 v_0/\partial x^2 \\
&+ (B_{12} + B_{66})\,\partial^2 v_0/\partial x\partial y + B_{26}\,\partial^2 v_0/\partial y^2 + D_{11}\,\partial^2 a/\partial x^2 + 2\,D_{16}\,\partial^2 a/\partial x\partial y \\
&+ D_{66}\,\partial^2 a/\partial y^2 + D_{16}\,\partial^2 b/\partial x^2 + (D_{12} + D_{66})\,\partial^2 b/\partial x\partial y + D_{26}\,\partial^2 b/\partial y^2 \\
&- A_{55}\,(a + \partial w/\partial x) - A_{45}\,(b + \partial w/\partial y) = R\,\partial^2 u_0/\partial t^2 + I\,\partial^2 a/\partial t^2
\end{aligned}
\qquad \textbf{[58]}
$$

$$
\begin{aligned}
&B_{16}\,\partial^2 u_0/\partial x^2 + (B_{12} + B_{66})\,\partial^2 u_0/\partial x\partial y + B_{26}\,\partial^2 u_0/\partial y^2 + B_{66}\,\partial^2 v_0/\partial x^2 \\
&+ 2\,B_{26}\,\partial^2 v_0/\partial x\partial y + B_{22}\,\partial^2 v_0/\partial y^2 + D_{16}\,\partial^2 a/\partial x^2 + (D_{12} + D_{66})\,\partial^2 a/\partial x\partial y \\
&+ D_{26}\,\partial^2 a/\partial y^2 + D_{66}\,\partial^2 b/\partial x^2 + 2\,D_{26}\,\partial^2 b/\partial x\partial y + D_{22}\,\partial^2 b/\partial y^2 \\
&- A_{45}\,(a + \partial w/\partial x) - A_{44}\,(b + \partial w/\partial y) = R\,\partial^2 v_0/\partial t^2 + I\,\partial^2 b/\partial t^2
\end{aligned}
\qquad \textbf{[59]}
$$

For unsymmetric laminates, all five equations remain coupled. However, for balanced laminates, the coupling stiffnesses, B_{ij}, and the coupling normal-rotational inertia coefficients, R, are identically zero. With this simplification, the equations are decoupled into two sets of equations governing the in-plane (extensional) and transverse (flexural) motions separately.

$$
\begin{aligned}
&A_{11}\,\partial^2 u_0/\partial x^2 + 2\,A_{16}\,\partial^2 u_0/\partial x\partial y + A_{66}\,\partial^2 u_0/\partial y^2 + A_{16}\,\partial^2 v_0/\partial x^2 \\
&+ (A_{12} + A_{66})\,\partial^2 v_0/\partial x\partial y + A_{26}\,\partial^2 v_0/\partial y^2 = \bar{r}\,\partial^2 u_0/\partial t^2
\end{aligned}
\qquad \textbf{[60]}
$$

$$
\begin{aligned}
&A_{16}\,\partial^2 u_0/\partial x^2 + (A_{12} + A_{66})\,\partial^2 u_0/\partial x\partial y + A_{26}\,\partial^2 u_0/\partial y^2 + A_{66}\,\partial^2 v_0/\partial x^2 \\
&+ 2\,A_{26}\,\partial^2 v_0/\partial x\partial y + A_{22}\,\partial^2 v_0/\partial y^2 = \bar{r}\,\partial^2 v_0/\partial t^2
\end{aligned}
\qquad \textbf{[61]}
$$

$$
\begin{aligned}
&A_{55}\left(\partial a/\partial x + \partial^2 w/\partial x^2\right) + A_{45}\left(\partial a/\partial y + \partial b/\partial x + 2\,\partial^2 w/\partial x\partial y\right) \\
&+ A_{44}\left(\partial b/\partial y + \partial^2 w/\partial y^2\right) = \bar{r}\,\partial^2 w/\partial t^2
\end{aligned}
\qquad \textbf{[62]}
$$

$$
\begin{aligned}
&D_{11}\,\partial^2 a/\partial x^2 + 2\,D_{16}\,\partial^2 a/\partial x\partial y + D_{66}\,\partial^2 a/\partial y^2 + D_{16}\,\partial^2 b/\partial x^2 \\
&+ (D_{12} + D_{66})\,\partial^2 b/\partial x\partial y + D_{26}\,\partial^2 b/\partial y^2 - A_{55}\,(a + \partial w/\partial x) \\
&- A_{45}\,(b + \partial w/\partial y) = I\,\partial^2 a/\partial t^2
\end{aligned}
\qquad \textbf{[63]}
$$

$$
\begin{aligned}
&D_{16}\,\partial^2 a/\partial x^2 + (D_{12} + D_{66})\,\partial^2 a/\partial x\partial y + D_{26}\,\partial^2 a/\partial y^2 + D_{66}\,\partial^2 b/\partial x^2 \\
&+ 2\,D_{26}\,\partial^2 b/\partial x\partial y + D_{22}\,\partial^2 b/\partial y^2 - A_{45}\,(a + \partial w/\partial x) \\
&- A_{44}\,(b + \partial w/\partial y) = I\,\partial^2 b/\partial t^2
\end{aligned}
\qquad \textbf{[64]}
$$

Further simplifications may be made for symmetric, cross-ply laminates with lamina in only the 0° and 90° orientations ($A_{16} = A_{26} = A_{45} = D_{16} = D_{26} = 0$).

$$
A_{11}\,\partial^2 u_0/\partial x^2 + A_{66}\,\partial^2 u_0/\partial y^2 + A_{66}\,\partial^2 v_0/\partial x\partial y = \bar{r}\,\partial^2 u_0/\partial t^2
\qquad \textbf{[65]}
$$

$$A_{66}\,\partial^2 u_0/\partial x\partial y + A_{66}\,\partial^2 v_0/\partial x^2\ A_{22}\,\partial^2 v_0/\partial y^2 = \overline{r}\,\partial^2 v_0/\partial t^2 \qquad \textbf{[66]}$$

$$A_{55}\left(\partial a/\partial x + \partial^2 w/\partial x^2\right) + A_{44}\left(\partial b/\partial y + \partial^2 w/\partial y^2\right) = \overline{r}\,\partial^2 w/\partial t^2 \qquad \textbf{[67]}$$

$$D_{11}\,\partial^2 a/\partial x^2 + D_{66}\,\partial^2 a/\partial y^2 + D_{66}\,\partial^2 b/\partial x\partial y - A_{55}\left(a + \partial w/\partial x\right) = I\,\partial^2 a/\partial t^2 \qquad \textbf{[68]}$$

$$D_{66}\,\partial^2 a/\partial x\partial y + D_{66}\,\partial^2 b/\partial x^2 + D_{22}\,\partial^2 b/\partial y^2 - A_{44}\left(b + \partial w/\partial y\right) = I\,\partial^2 b/\partial t^2 \qquad \textbf{[69]}$$

The following expressions are considered as displacement solutions for the equations of motion ([65] through [69]).

$$\begin{aligned} u &= \mathbf{U}\exp\{i[k(l_1 x + l_2 y) - w t]\} \\ v &= \mathbf{V}\exp\{i[k(l_1 x + l_2 y) - w t]\} \\ w &= \mathbf{W}\exp\{i[k(l_1 x + l_2 y) - w t]\} \\ a &= \mathbf{?}\ \exp\{i[k(l_1 x + l_2 y) - w t]\} \\ b &= \mathbf{?}\ \exp\{i[k(l_1 x + l_2 y) - w t]\} \end{aligned} \qquad \textbf{[70]}$$

U	maximum magnitude of displacement in the x-direction
V	maximum magnitude of displacement in the y-direction
W	maximum magnitude of displacement in the w-direction
A	maximum magnitude of rotation about the y-axis
B	maximum magnitude of rotation about the x-axis
i	square root of –1 (imaginary)
k	wave number (or wave vector) ($k = 2p\ /\ l$) (radians per length)
l_1	direction cosine between wave propagation direction and x-axis
l_2	direction cosine between wave propagation direction and y-axis
w	frequency of propagated wave (radians/time)
t	time

Concentrating on the first two equations of motion ([65] and [66]) for extensional wave propagation, the following expressions are evaluated:

$$\begin{aligned}
\partial^2 u_0/\partial x^2 &= -\mathbf{U} k^2 l_1^2 \exp\{i[k(l_1 x + l_2 y) - w t]\} \\
\partial^2 u_0/\partial y^2 &= -\mathbf{U} k^2 l_2^2 \exp\{i[k(l_1 x + l_2 y) - w t]\} \\
\partial^2 u_0/\partial x \partial y &= -\mathbf{U} k^2 l_1 l_2 \exp\{i[k(l_1 x + l_2 y) - w t]\} \\
\partial^2 u_0/\partial t^2 &= -\mathbf{U} w^2 \exp\{i[k(l_1 x + l_2 y) - w t]\} \\
\partial^2 v_0/\partial x^2 &= -\mathbf{V} k^2 l_1^2 \exp\{i[k(l_1 x + l_2 y) - w t]\} \\
\partial^2 v_0/\partial y^2 &= -\mathbf{V} k^2 l_2^2 \exp\{i[k(l_1 x + l_2 y) - w t]\} \\
\partial^2 v_0/\partial x \partial y &= -\mathbf{V} k^2 l_1 l_2 \exp\{i[k(l_1 x + l_2 y) - w t]\} \\
\partial^2 v_0/\partial t^2 &= -\mathbf{V} w^2 \exp\{i[k(l_1 x + l_2 y) - w t]\}
\end{aligned} \qquad \textbf{[71]}$$

The sign and exponent cancel out, from which the following expressions for extensional wave propagation result (sub Eqn. [71] into [65] and [66]).

$$A_{11}\mathbf{U}k^2 l_1^2 + A_{66}\mathbf{U}k^2 l_2^2 + A_{66}\mathbf{V}k^2 l_1 l_2 = \mathbf{U}\overline{r}w^2 \qquad \textbf{[72]}$$

$$A_{66}\mathbf{U}k^2 l_1 l_2 + A_{66}\mathbf{V}k^2 l_1^2 + A_{22}\mathbf{V}k^2 l_2^2 = \mathbf{V}\overline{r}w^2 \qquad \textbf{[73]}$$

For wave propagation in the x-direction ($l_1 = 1$, $l_2 = 0$) the equations reduce to the following

$$\begin{aligned}
A_{11}k^2 &= \overline{r}w^2 \\
A_{66}k^2 &= \overline{r}w^2
\end{aligned} \qquad \textbf{[74]}$$

For wave propagation in the y-direction ($l_2 = 1$, $l_1 = 0$) the equations reduce to the following

$$\begin{aligned}
A_{66}k^2 &= \overline{r}w^2 \\
A_{22}k^2 &= \overline{r}w^2
\end{aligned} \qquad \textbf{[75]}$$

These expressions present a linear relationship between the wave number, *k*, and the frequency of the wave, *w*. Therefore, the extensional (symmetric) waves are nondispersive as they travel through the plate (i.e. phase velocity is not dependent upon frequency). The equations possessing the A_{66} term refer to shear horizontal (SH) wave propagation, which is outside the scope of this research.

Concentrating on the last three equations of motion ([67], [68], and [69]) for flexural wave propagation, the following expressions are evaluated:

$$
\begin{aligned}
\partial w/\partial x &= i\,\mathbf{W}\,k\,l_1 \exp\{i[k(l_1 x + l_2 y) - w t]\} \\
\partial^2 w/\partial x^2 &= -\mathbf{W}\,k^2\,l_1{}^2 \exp\{i[k(l_1 x + l_2 y) - w t]\} \\
\partial w/\partial y &= i\,\mathbf{W}\,k\,l_2 \exp\{i[k(l_1 x + l_2 y) - w t]\} \\
\partial^2 w/\partial y^2 &= -\mathbf{W}\,k^2\,l_2{}^2 \exp\{i[k(l_1 x + l_2 y) - w t]\} \\
\partial^2 w/\partial x \partial y &= -\mathbf{W}\,k^2\,l_1\,l_2 \exp\{i[k(l_1 x + l_2 y) - w t]\} \\
\partial^2 w/\partial t^2 &= -\mathbf{W} w^2 \exp\{i[k(l_1 x + l_2 y) - w t]\} \\
\partial a/\partial x &= i\,\mathbf{A}\,k\,l_1 \exp\{i[k(l_1 x + l_2 y) - w t]\} \\
\partial^2 a/\partial x^2 &= -\mathbf{A}\,k^2\,l_1{}^2 \exp\{i[k(l_1 x + l_2 y) - w t]\} \\
\partial^2 a/\partial y^2 &= -\mathbf{A}\,k^2\,l_2{}^2 \exp\{i[k(l_1 x + l_2 y) - w t]\} \\
\partial^2 a/\partial x \partial y &= -\mathbf{A}\,k^2\,l_1\,l_2 \exp\{i[k(l_1 x + l_2 y) - w t]\} \\
\partial^2 a/\partial t^2 &= -\mathbf{A} w^2 \exp\{i[k(l_1 x + l_2 y) - w t]\} \\
\partial^2 b/\partial x^2 &= -\mathbf{B}\,k^2\,l_1{}^2 \exp\{i[k(l_1 x + l_2 y) - w t]\} \\
\partial b/\partial y &= i\,\mathbf{B}\,k\,l_2 \exp\{i[k(l_1 x + l_2 y) - w t]\} \\
\partial^2 b/\partial y^2 &= -\mathbf{B}\,k^2\,l_2{}^2 \exp\{i[k(l_1 x + l_2 y) - w t]\} \\
\partial^2 b/\partial x \partial y &= -\mathbf{B}\,k^2\,l_1\,l_2 \exp\{i[k(l_1 x + l_2 y) - w t]\} \\
\partial^2 b/\partial t^2 &= -\mathbf{B} w^2 \exp\{i[k(l_1 x + l_2 y) - w t]\}
\end{aligned}
\qquad \textbf{[76]}
$$

Again, dropping the sign and exponent for brevity, the following expressions for flexural wave propagation result.

$$A_{55}\left(i\,\mathbf{A}\,k\,l_1 - \mathbf{W}\,k^2\,l_1{}^2\right) + A_{44}\left(i\,\mathbf{B}\,k\,l_2 - \mathbf{W}\,k^2\,l_2{}^2\right) + \mathbf{W}\,\overline{r}\,w^2 = 0 \qquad \textbf{[77]}$$

$$D_{11}\left(-\mathbf{A}\,k^2\,l_1{}^2\right) + D_{66}\left(-\mathbf{B}\,k^2\,l_1\,l_2 - \mathbf{A}\,k^2\,l_2{}^2\right) - A_{55}\left(\mathbf{A} + i\,\mathbf{W}\,k\,l_1\right) + I\,\mathbf{A} w^2 = 0 \qquad \textbf{[78]}$$

$$D_{22}\left(-\mathbf{B}\,k^2\,l_2{}^2\right) + D_{66}\left(-\mathbf{A}\,k^2\,l_1\,l_2 - \mathbf{B}\,k^2\,l_1{}^2\right) - A_{44}\left(\mathbf{B} + i\,\mathbf{W}\,k\,l_2\right) + I\,\mathbf{B} w^2 = 0 \qquad \textbf{[79]}$$

These equations can be rearranged and placed in matrix form.

$$\begin{bmatrix} \begin{pmatrix} D_{11}\,k^2\,l_1{}^2 + A_{55} \\ + D_{66}\,k^2\,l_2{}^2 - I\,w^2 \end{pmatrix} & D_{66}\,k^2\,l_1\,l_2 & i\,A_{55}\,k\,l_1 \\ D_{66}\,k^2\,l_1\,l_2 & \begin{pmatrix} D_{22}\,k^2\,l_2{}^2 + A_{44} \\ + D_{66}\,k^2\,l_1{}^2 - I w^2 \end{pmatrix} & i\,A_{44}\,k\,l_2 \\ i\,A_{55}\,k\,l_1 & i\,A_{44}\,k\,l_2 & -A_{55}\,k^2\,l_1{}^2 - A_{44}\,k^2\,l_2{}^2 + \overline{r}\,w^2 \end{bmatrix} \begin{Bmatrix} \mathrm{A} \\ \mathrm{B} \\ \mathrm{W} \end{Bmatrix} = \begin{Bmatrix} 0 \\ 0 \\ 0 \end{Bmatrix} \qquad \textbf{[80]}$$

Setting the determinant of the 3 by 3 matrix equal to zero will result in the dispersion relations for flexural plate wave propagation. To simplify the calculation of the determinant, values of l_1 and l_2 may be substituted. For flexural wave propagation in the x-direction ($l_1 = 1$, $l_2 = 0$), the matrix simplifies to the following:

$$\det\begin{bmatrix} D_{11}k^2 + A_{55} - Iw^2 & 0 & iA_{55}k \\ 0 & A_{44} + D_{66}k^2 - Iw^2 & 0 \\ iA_{55}k & 0 & -A_{55}k^2 + \bar{r}w^2 \end{bmatrix} = 0 \qquad \textbf{[81]}$$

whereupon the dispersion equation for flexural wave propagation in the x-direction results. The wave number subscript, "1", is included for clarification of propagation in the x-direction.

$$\left(D_{11}k_1^2 + A_{55} - Iw^2\right)\left(A_{55}k_1^2 - \bar{r}w^2\right) - A_{55}^2 k_1^2 = 0 \qquad \textbf{[82]}$$

Likewise, in the y-direction ($l_1 = 0$, $l_2 = 1$), the matrix simplifies to the following:

$$\det\begin{bmatrix} A_{55} + D_{66}k^2 - Iw^2 & 0 & 0 \\ 0 & D_{22}k^2 + A_{44} - Iw^2 & iA_{44}k \\ 0 & iA_{44}k & -A_{44}k^2 + \bar{r}w^2 \end{bmatrix} = 0 \qquad \textbf{[83]}$$

Therefore, the dispersion relation for flexural wave propagation in the y-direction is developed. Again, a subscript, "2", has been used with the wave number to indicate wave propagation in the y-direction.

$$\left(D_{22}k_2^2 + A_{44} - Iw^2\right)\left(A_{44}k_2^2 - \bar{r}w^2\right) - A_{44}^2 k_2^2 = 0 \qquad \textbf{[84]}$$

Note that equations [82] and [84] represent a nonlinear relationship between wave number, k, and frequency, w. In this case, flexural (antisymmetric) waves are dispersive as they travel through the plate (i.e. phase velocity is dependent upon frequency).

APPENDIX II. DISPERSION CURVES

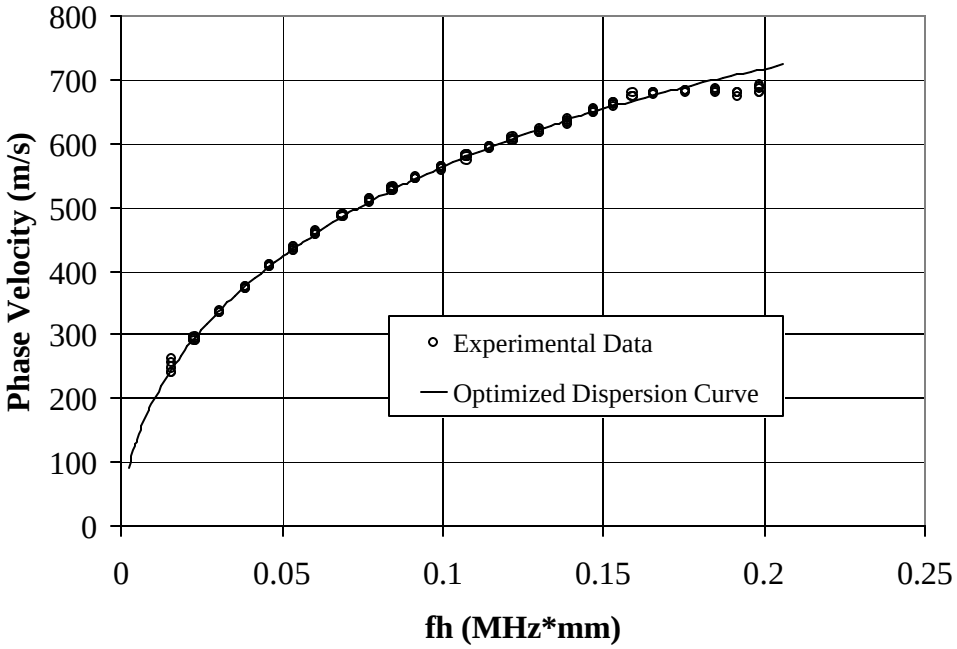

Figure 26: Dispersion curve for MDF-A

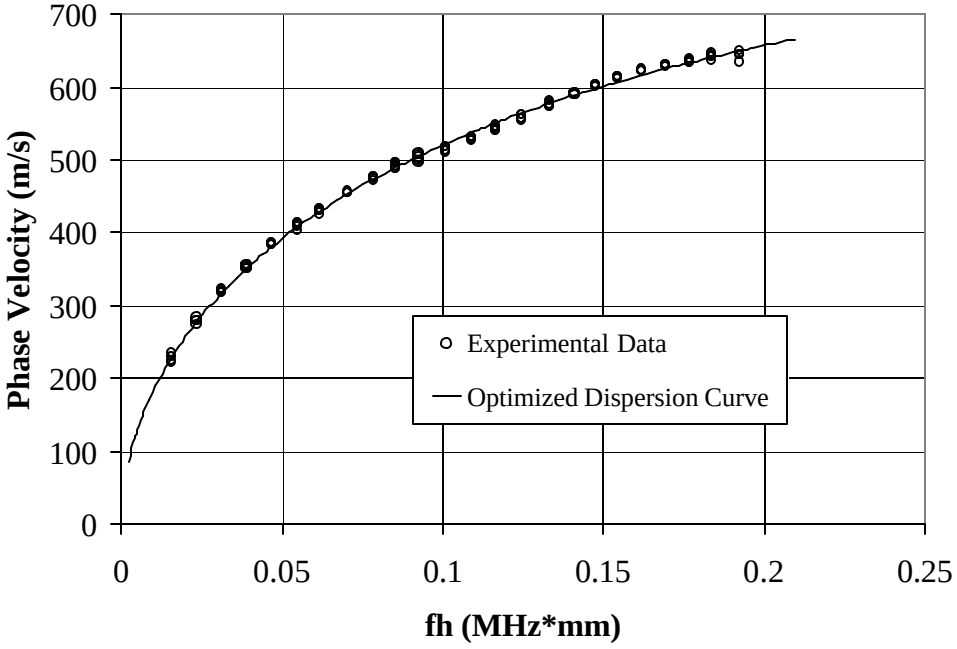

Figure 27: Dispersion curve for MDF-B

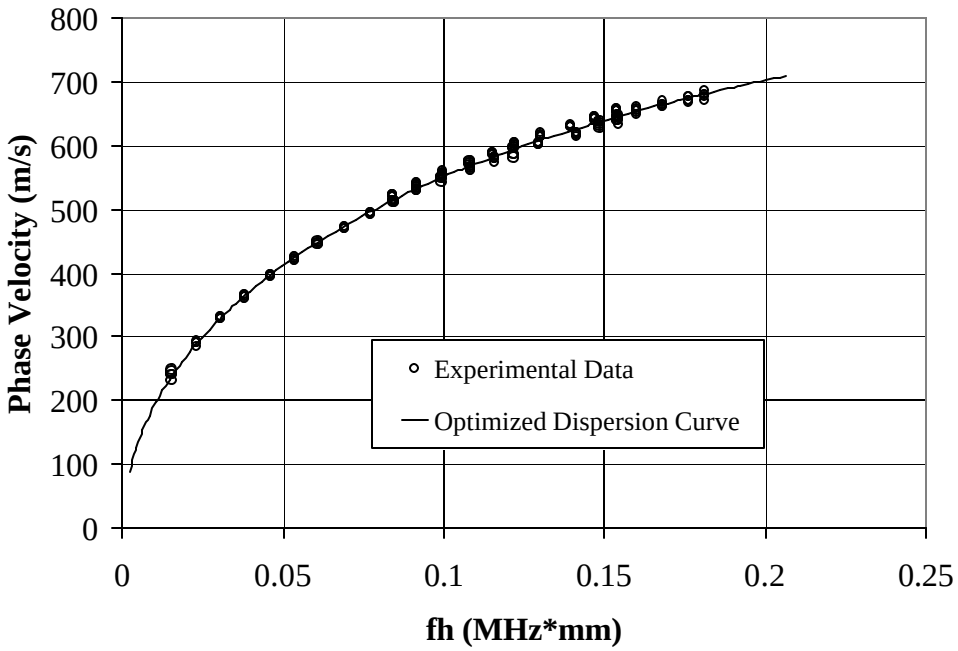

Figure 28: Dispersion curve for MDF-C

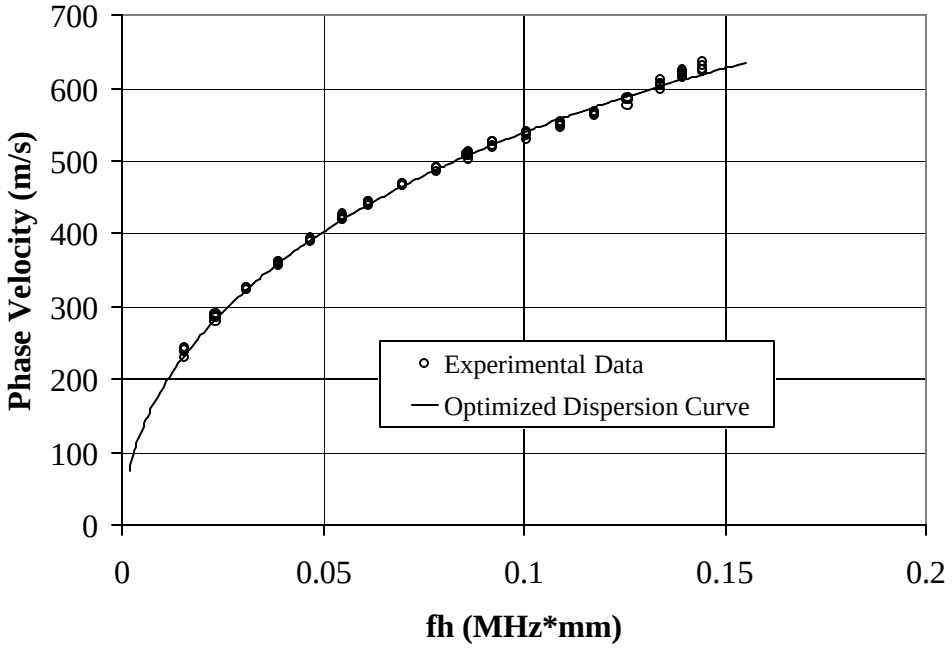

Figure 29: Dispersion curve for MDF-D

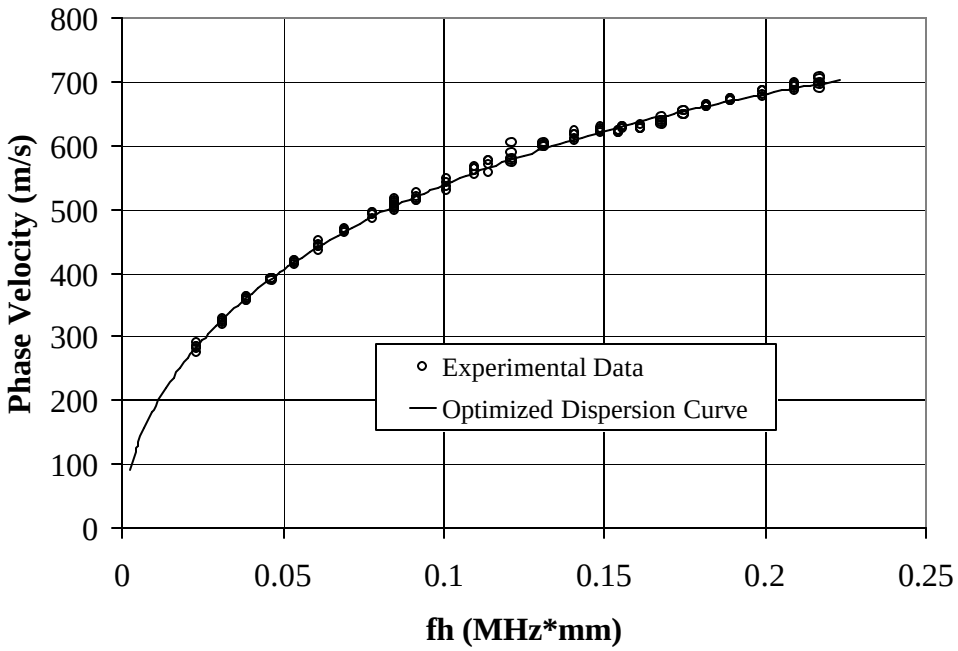

Figure 30: Dispersion curve for MDF-E

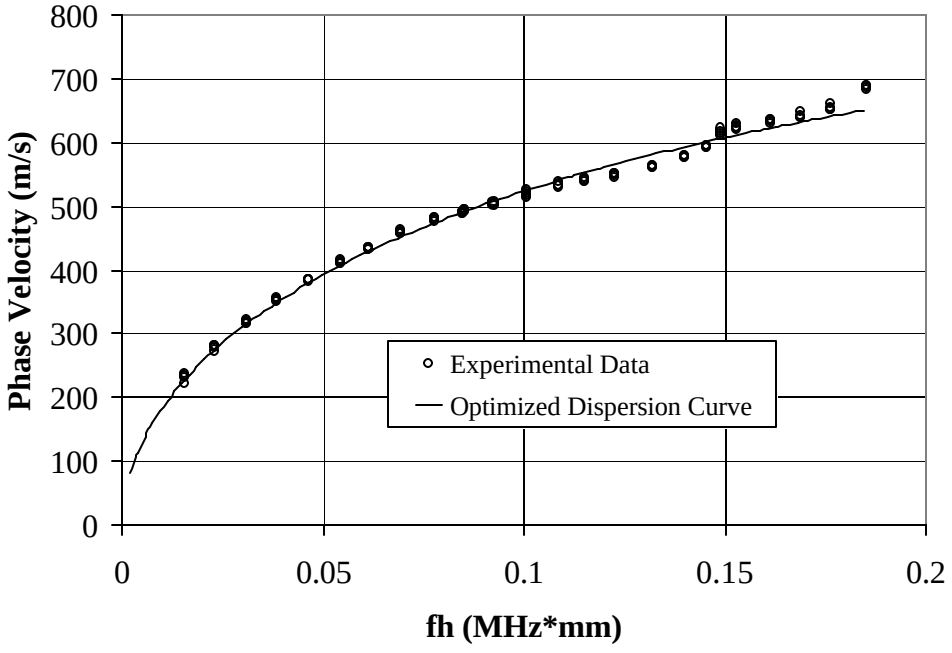

Figure 31: Dispersion curve for MDF-F

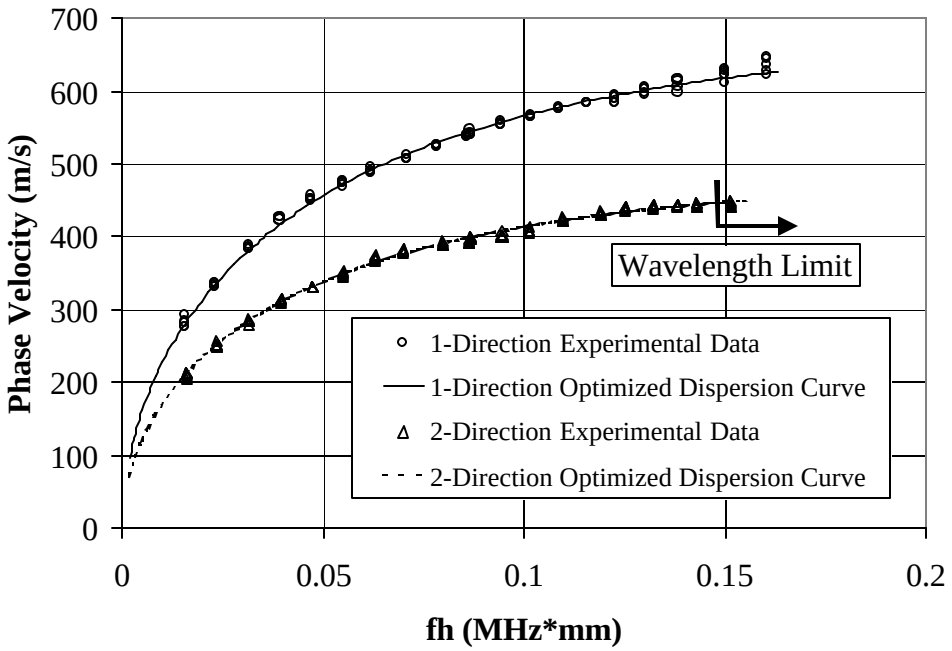

Figure 32: Dispersion curves for OWS-A

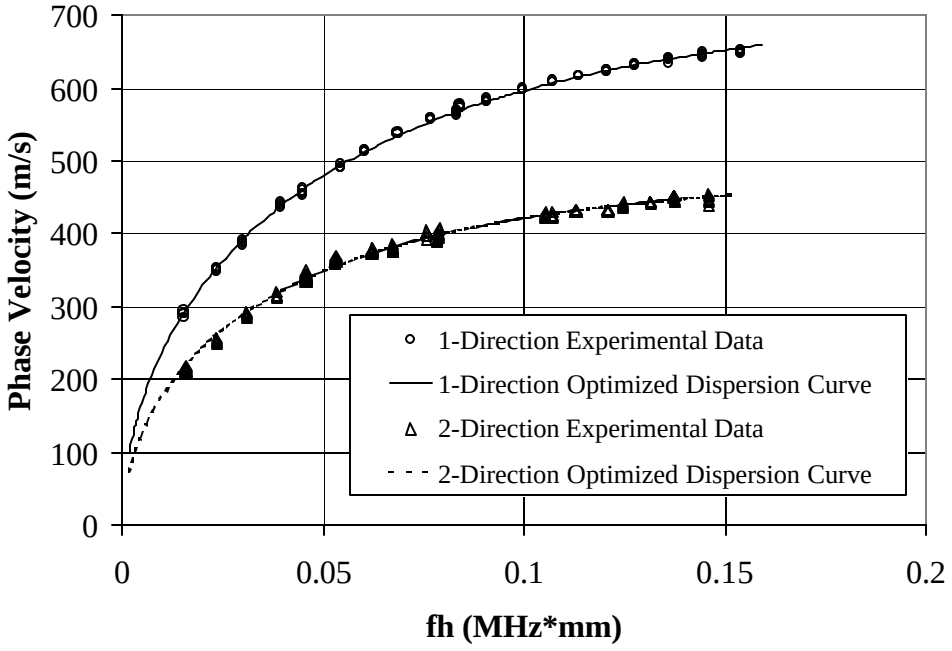

Figure 33: Dispersion curves for OWS-B

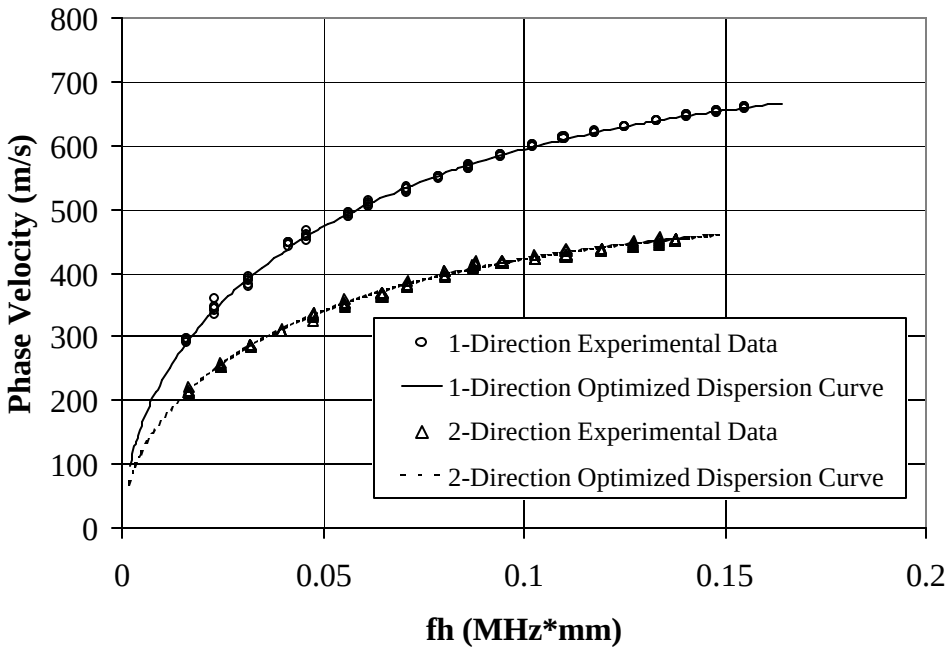

Figure 34: Dispersion curves for OWS-C

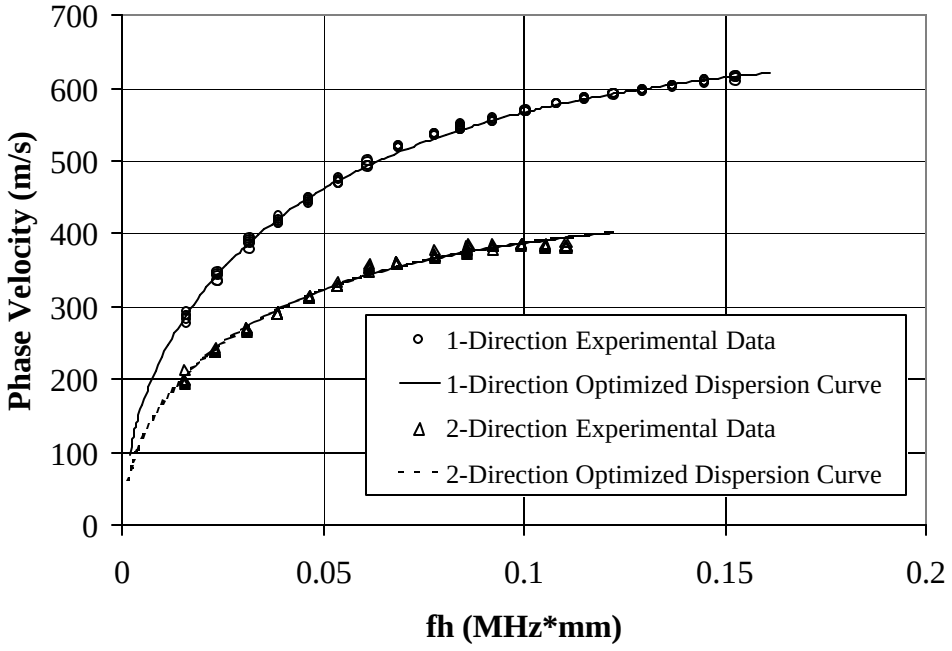

Figure 35: Dispersion curves for OWS-D

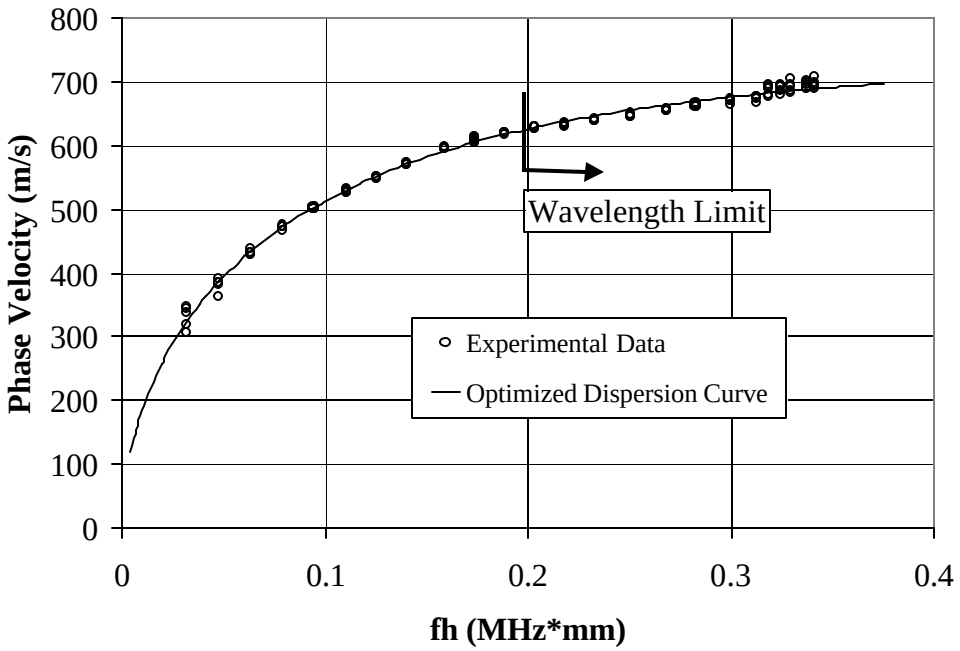

Figure 36: Dispersion curve for MDF-G

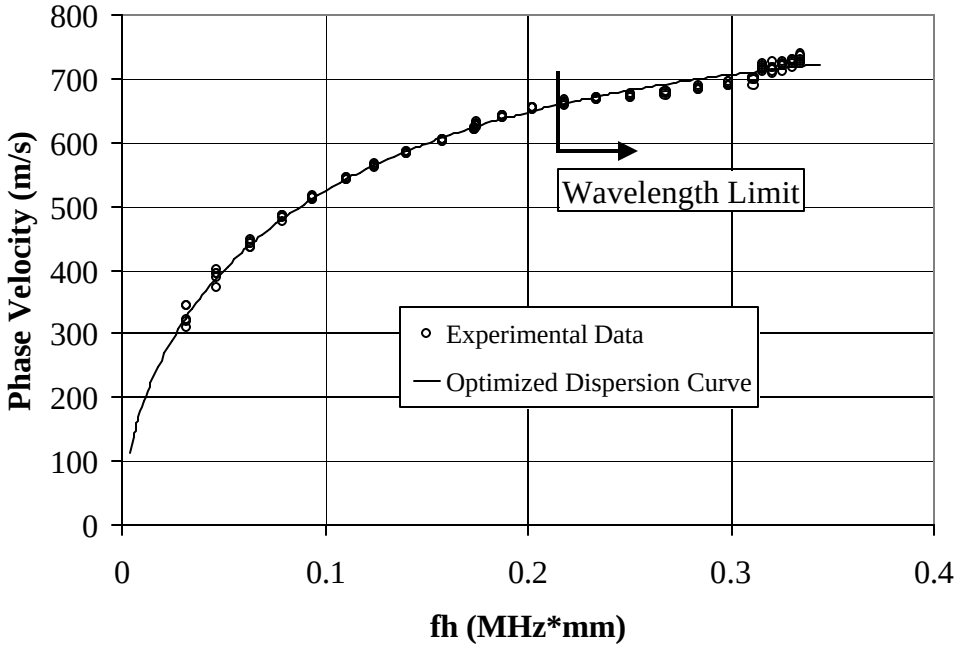

Figure 37: Dispersion curve for MDF-H

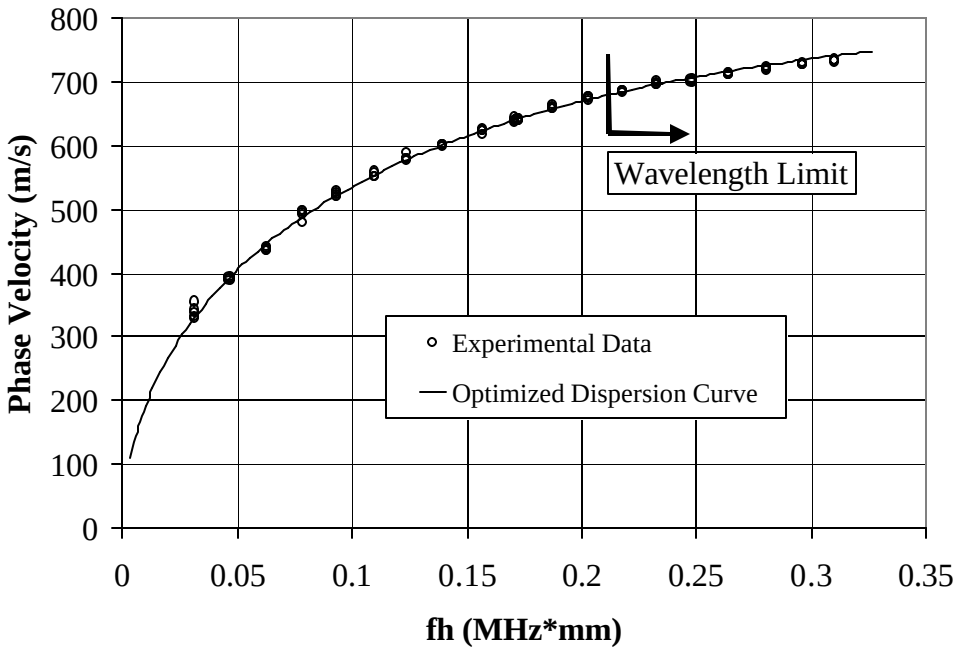

Figure 38: Dispersion curve for MDF laminate

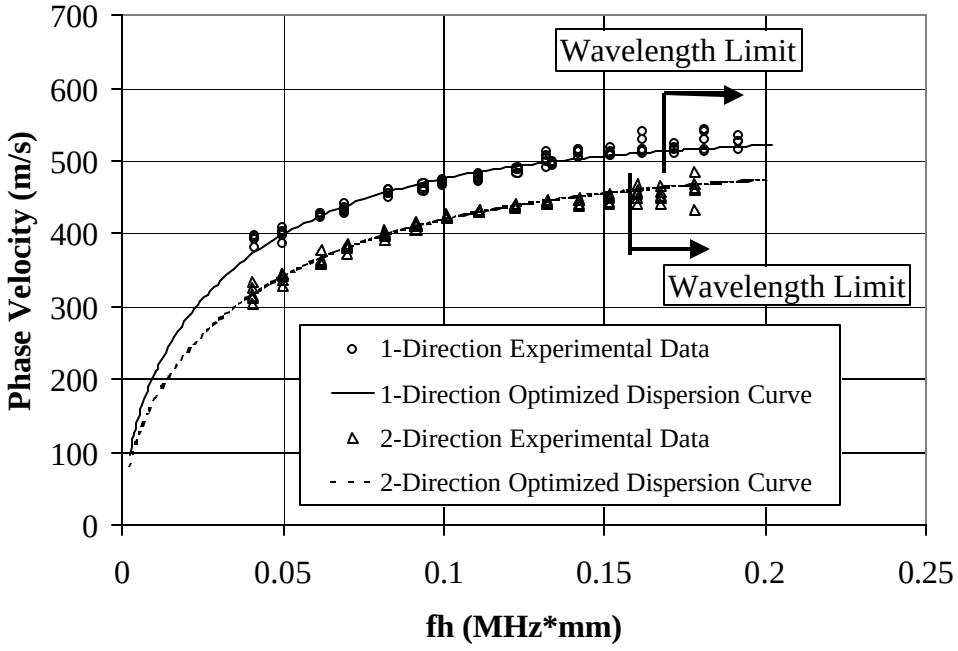

Figure 39: Dispersion curves for [0/90/0] OWS laminate

APPENDIX III. DEFECT DETECTION PLOTS

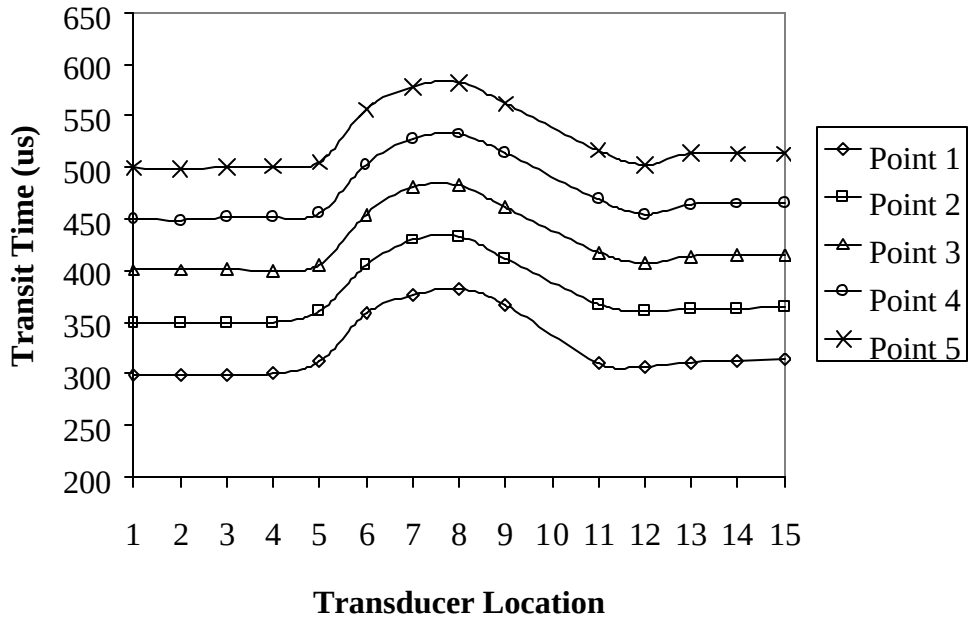

Figure 40: Defect detection of 6-cm square delamination in an MDF laminate using a 10-kHz frequency at 1.5-cm location increments

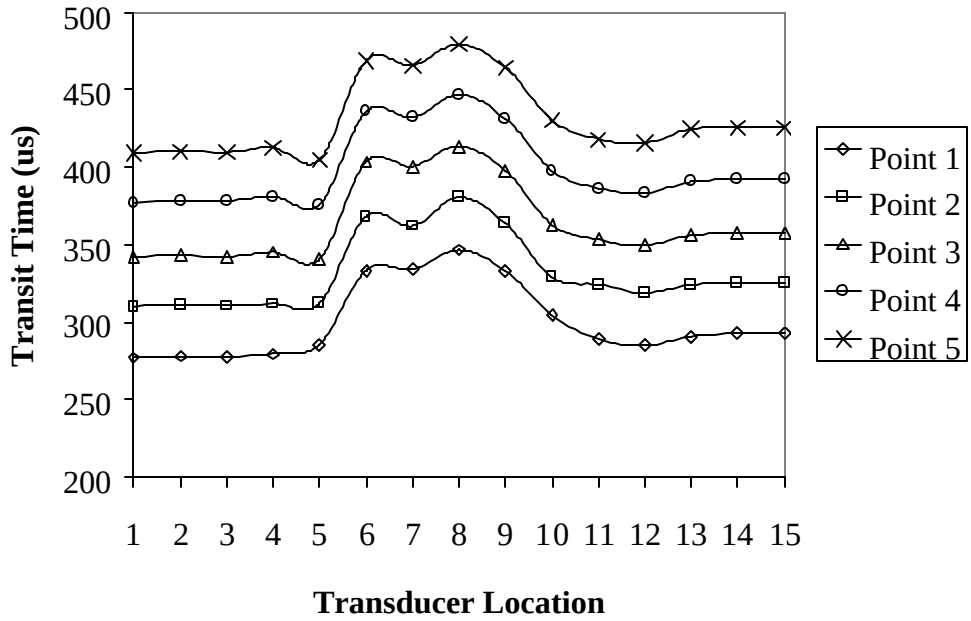

Figure 41: Defect detection of 6-cm square delamination in an MDF laminate using a 15-kHz frequency at 1.5-cm location increments

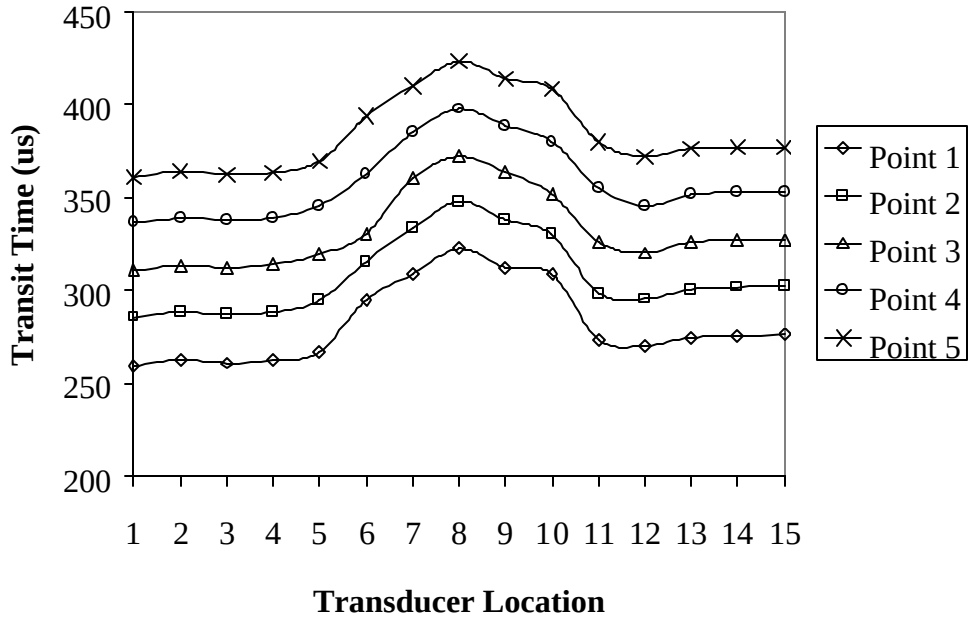

Figure 42: Defect detection of 6-cm square delamination in an MDF laminate using a 20-kHz frequency at 1.5-cm location increments

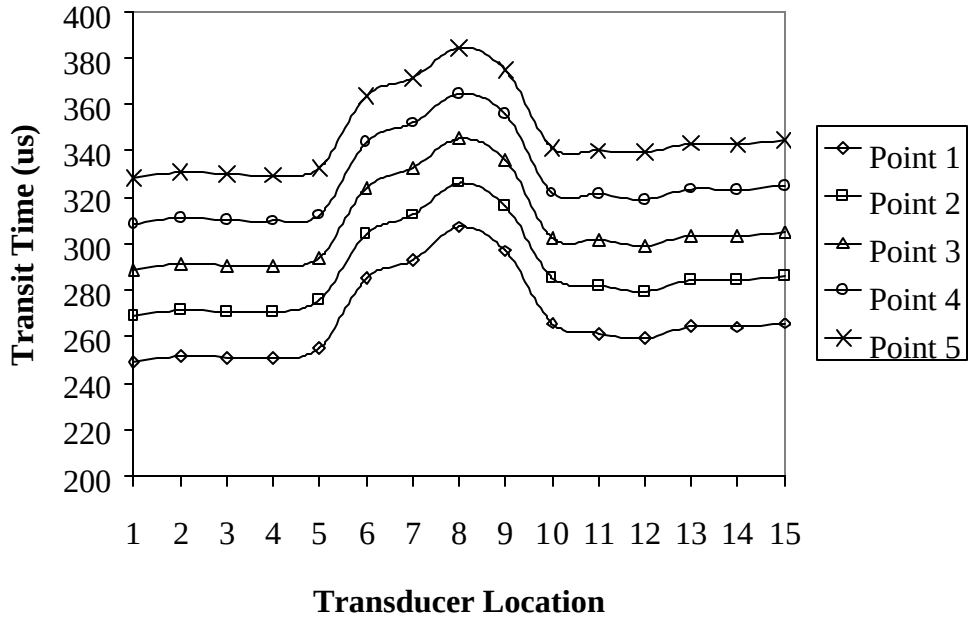

Figure 43: Defect detection of 6-cm square delamination in an MDF laminate using a 25-kHz frequency at 1.5-cm location increments

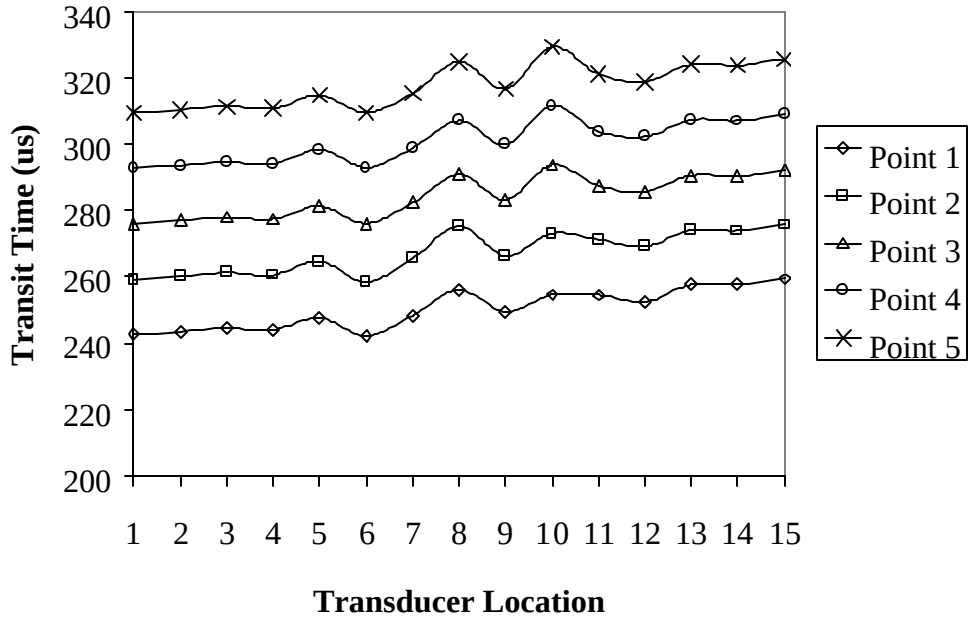

Figure 44: Defect detection of 6-cm square delamination in an MDF laminate using a 30-kHz frequency at 1.5-cm location increments

APPENDIX IV. SHEAR DEFORMATION PLATE THEORY WORKSHEETS

MDF Laminate Properties

Author: Lloyd Smith, 11-17-98
Brian Tucker, 11-7-99
smith@mme.wsu.edu
tuckerb@wsu.edu

Enter lamina orientations, thicknesses, and material group (insert rows as necessary)

Orientations: Thicknesses: Material group:

$$\theta := \begin{pmatrix} 0 \\ 0 \\ 0 \end{pmatrix} \cdot deg \qquad \Delta z := \begin{pmatrix} 0.1201 \\ 0.1221 \\ 0 \end{pmatrix} \cdot 0.0254 \qquad m := \begin{pmatrix} 5 \\ 6 \\ 1 \end{pmatrix}$$

1=Null
2=OWS_A
3=OWS_C
4=OWS_D
5=MDF_A
6=MDF_D

Elastic properties from NDE testing (units in Pa)

$Q_{11} := (0 \quad 7.411466908 \quad 8.257273832 \quad 7.175718716 \quad 3.3708 \quad 2.7275 \quad 0 \quad 0 \quad 0)^T \cdot 10^9$

$Q_{22} := (0 \quad 2.177858783 \quad 2.560860868 \quad 1.899556624 \quad 3.3708 \quad 2.7275 \quad 0 \quad 0 \quad 0)^T \cdot 10^9$

Q44 = $kG_{23} := (0 \quad 311.6574588 \quad 384.1103216 \quad 295.1687433 \quad 0660.4 \quad 0619.9 \quad 0 \quad 0 \quad 0)^T \cdot 10^6$

Q55 = $kG_{31} := (0 \quad 157.5551512 \quad 181.0429019 \quad 126.9652128 \quad 0660.4 \quad 0619.9 \quad 0 \quad 0 \quad 0)^T \cdot 10^6$

Mass Density $\rho := (0 \quad 0.639474175 \quad 0.664673859 \quad 0.631762812 \quad 0.684405173 \quad 0.674242287 \quad 0 \quad 0 \quad 0)^T \cdot 1000$

$i := 1.. length(m)$

Number of lamina: $n := \sum_i (m_i > 1) \qquad i := 1..n$

$$R := \begin{pmatrix} 1 & 0 & 0 \\ 0 & 1 & 0 \\ 0 & 0 & 2 \end{pmatrix}$$

Laminate thickness: $t := \sum_i \Delta z_i \qquad t = 6.1519 \times 10^{-3}$

$\Delta z_1 = 3.0505 \times 10^{-3}$

Lamina locations: $z_1 := \frac{-t}{2} \qquad z_{i+1} := z_i + \Delta z_i$

Define 2-d compliance matrix:

$$Q(k) := \begin{bmatrix} Q_{11_{(m_k)}} & 1 & 0 & 0 & 0 \\ 1 & Q_{22_{(m_k)}} & 0 & 0 & 0 \\ 0 & 0 & kG_{23_{(m_k)}} & 0 & 0 \\ 0 & 0 & 0 & kG_{31_{(m_k)}} & 0 \\ 0 & 0 & 0 & 0 & 1 \end{bmatrix}$$

Define transformation matrix

$$T(k) := \begin{bmatrix} \cos(\theta_k)^2 & \sin(\theta_k)^2 & 0 & 0 & 2\cdot\cos(\theta_k)\cdot\sin(\theta_k) \\ \sin(\theta_k)^2 & \cos(\theta_k)^2 & 0 & 0 & -2\cdot\cos(\theta_k)\cdot\sin(\theta_k) \\ 0 & 0 & \cos(\theta_k) & \sin(\theta_k) & 0 \\ 0 & 0 & -\sin(\theta_k) & \cos(\theta_k) & 0 \\ -(\cos(\theta_k)\cdot\sin(\theta_k)) & \cos(\theta_k)\cdot\sin(\theta_k) & 0 & 0 & \cos(\theta_k)^2 - \sin(\theta_k)^2 \end{bmatrix}$$

$$Q_b(k) := T(k)^{-1}\cdot Q(k)\cdot T(k)^{-1^T}$$

Calculate the Laminate Rigidity Matrices

$$A := \sum_i Q_b(i)\cdot(z_{i+1} - z_i) \qquad D := \frac{1}{3}\cdot\sum_i Q_{bred}(i)\cdot\left[(z_{i+1})^3 - (z_i)^3\right]$$

$A_{1,1} = 1.8742\times 10^7$ $\frac{N}{m}$ $\quad A_{3,3} = 3.9371\times 10^6$ $\frac{N}{m}$ $\quad D_{1,1} = 5.9159\times 10^1$ $N\cdot m$

$A_{2,2} = 1.8742\times 10^7$ $\quad A_{4,4} = 3.9371\times 10^6$ $\quad D_{2,2} = 5.9159\times 10^1$

Effective Laminate Density $\quad \rho bar := \sum_i \rho_i\cdot(z_{i+1} - z_i) \quad \rho bar = 1.9832 \quad \frac{kg}{m^2}$

Rotational Inertia $\quad I := \sum_i \rho_i\cdot\left[(z_{i+1})^3 - (z_i)^3\right] \quad I = 1.861\times 10^{-5} \quad kg \quad or \quad \frac{N\cdot s^2}{m}$

OWS Laminate Properties

Author: Lloyd Smith, 11-17-98
Brian Tucker, 11-7-99
smith@mme.wsu.edu
tuckerb@wsu.edu

Enter lamina orientations, thicknesses, and material group (insert rows as necessary)

Orientations: Thicknesses: Material group:

$$\theta := \begin{pmatrix} 0 \\ 90 \\ 0 \end{pmatrix} \cdot \text{deg} \qquad \Delta z := \begin{pmatrix} 0.1225 \\ 0.1235 \\ 0.121 \end{pmatrix} \cdot 0.0254 \qquad m := \begin{pmatrix} 2 \\ 3 \\ 4 \end{pmatrix}$$

Elastic properties from NDE testing (units in Pa)

1=Null
2=OWS_A
3=OWS_C
4=OWS_D

$$Q_{11} := (0 \quad 6.03169093875736.70469610500556.51479656537280 \quad 0 \quad 0 \quad 0 \quad 0)^T \cdot 10^9$$

$$Q_{22} := (0 \quad 1.96920653940641.96306272524931.79557917135300 \quad 0 \quad 0 \quad 0 \quad 0)^T \cdot 10^9$$

Q44 =

$$kG_{31} := (0 \quad 311.6574588 \quad 384.1103216 \quad 295.1687433 \quad 0 \quad 0 \quad 0 \quad 0 \quad 0)^T \cdot 10^6$$

Q55 =

$$kG_{23} := (0 \quad 157.5551512 \quad 181.0429019 \quad 126.9652128 \quad 0 \quad 0 \quad 0 \quad 0 \quad 0)^T \cdot 10^6$$

Mass Density

$$\rho := (0 \quad 0.639474175 \quad 0.664673859 \quad 0.631762812 \quad 0 \quad 0 \quad 0 \quad 0 \quad 0)^T \cdot 1000 \qquad \frac{kg}{m^3}$$

$$\rho US := \left(0 \quad 5.9735310^{-5} \quad 6.2089310^{-5} \quad 5.901510^{-5} \quad 0 \quad 0 \quad 0 \quad 0 \quad 0\right)^T$$

$$i := 1 .. \text{length}(m)$$

Number of lamina: $n := \sum_i (m_i > 1)$ $\quad i := 1 .. n$

Laminate thickness: $t := \sum_i \Delta z_i$ $\quad t = 9.3218 \times 10^{-3}$

$$R := \begin{pmatrix} 1 & 0 & 0 \\ 0 & 1 & 0 \\ 0 & 0 & 2 \end{pmatrix}$$

Lamina locations: $z_1 := \frac{-t}{2}$ $\quad z_{i+1} := z_i + \Delta z_i$

Define 2-d compliance matrix:

$$Q(k) := \begin{bmatrix} Q11_{(m_k)} & 1 & 0 & 0 & 0 \\ 1 & Q22_{(m_k)} & 0 & 0 & 0 \\ 0 & 0 & kG23_{(m_k)} & 0 & 0 \\ 0 & 0 & 0 & kG31_{(m_k)} & 0 \\ 0 & 0 & 0 & 0 & 1 \end{bmatrix}$$

Define transformation matrix

$$T(k) := \begin{bmatrix} \cos(\theta_k)^2 & \sin(\theta_k)^2 & 0 & 0 & 2\cdot\cos(\theta_k)\cdot\sin(\theta_k) \\ \sin(\theta_k)^2 & \cos(\theta_k)^2 & 0 & 0 & -2\cdot\cos(\theta_k)\cdot\sin(\theta_k) \\ 0 & 0 & \cos(\theta_k) & \sin(\theta_k) & 0 \\ 0 & 0 & -\sin(\theta_k) & \cos(\theta_k) & 0 \\ -(\cos(\theta_k)\cdot\sin(\theta_k)) & \cos(\theta_k)\cdot\sin(\theta_k) & 0 & 0 & \cos(\theta_k)^2 - \sin(\theta_k)^2 \end{bmatrix}$$

$$Q_b(k) := T(k)^{-1}\cdot Q(k)\cdot T(k)^{-1^T}$$

Calculate the Laminate Rigidity Matrices

$$A := \sum_i Q_b(i)\cdot(z_{i+1} - z_i) \qquad D := \frac{1}{3}\cdot\sum_i Q_{bred}(i)\cdot\left[(z_{i+1})^3 - (z_i)^3\right]$$

$A_{1,1} = 4.4948\times 10^7$ $\frac{N}{m}$ $A_{3,3} = 2.0854\times 10^6$ $\frac{N}{m}$ $D_{1,1} = 4.1234\times 10^2$ $N\cdot m$

$A_{2,2} = 3.2678\times 10^7$ $A_{4,4} = 2.4448\times 10^6$ $D_{2,2} = 1.3948\times 10^2$

Effective Laminate Density $\rho bar := \sum_i \rho_i\cdot(z_{i+1} - z_i)$ $\rho bar = 4.0488$ $\frac{kg}{m^2}$

Rotational Inertia $I := \sum_i \rho_i\cdot\left[(z_{i+1})^3 - (z_i)^3\right]$ $I = 6.9578\times 10^{-5}$ kg or $\frac{N\cdot s^2}{m}$

$$\rho barUS := \sum_i \rho US_i\cdot\frac{(z_{i+1} - z_i)}{0.0254} \qquad \rho barUS = 1.489\times 10^{-5}$$

OWS Laminate Properties

Enter lamina orientations, thicknesses, and material group (insert rows as necessary)

[ADJUSTED THICKNESSES]

Author: Lloyd Smith, 11-17-98
Brian Tucker, 11-7-99
smith@mme.wsu.edu
tuckerb@wsu.edu

Orientations: Thicknesses: Material group:

$$\theta := \begin{pmatrix} 0 \\ 90 \\ 0 \end{pmatrix} \cdot \text{deg} \qquad \Delta z := \begin{pmatrix} 0.1327 \\ 0.1336 \\ 0.1307 \end{pmatrix} \cdot 0.0254 \qquad m := \begin{pmatrix} 2 \\ 3 \\ 4 \end{pmatrix}$$

Elastic properties from NDE testing (units in Pa)

1=Null
2=OWS_A
3=OWS_C
4=OWS_D

$$Q_{11} := (0 \quad 6.0316909387573 \quad 6.7046961050055 \quad 6.5147965653728 \quad 0 \quad 0 \quad 0 \quad 0 \quad 0)^T \cdot 10^9$$

$$Q_{22} := (0 \quad 1.9692065394064 \quad 1.9630627252493 \quad 1.7955791713530 \quad 0 \quad 0 \quad 0 \quad 0 \quad 0)^T \cdot 10^9$$

Q44 =

$$kG_{31} := (0 \quad 311.6574588 \quad 384.1103216 \quad 295.1687433 \quad 0 \quad 0 \quad 0 \quad 0 \quad 0)^T \cdot 10^6$$

Q55 =

$$kG_{23} := (0 \quad 157.5551512 \quad 181.0429019 \quad 126.9652128 \quad 0 \quad 0 \quad 0 \quad 0 \quad 0)^T \cdot 10^6$$

Mass Density

$$\rho := (0 \quad 0.639474175 \quad 0.664673859 \quad 0.631762812 \quad 0 \quad 0 \quad 0 \quad 0 \quad 0)^T \cdot 1000 \qquad \frac{kg}{m^3}$$

$$\rho US := \left(0 \quad 5.97353 \cdot 10^{-5} \quad 6.20893 \cdot 10^{-5} \quad 5.9015 \cdot 10^{-5} \quad 0 \quad 0 \quad 0 \quad 0 \quad 0\right)^T$$

$i := 1 .. \text{length}(m)$

Number of lamina: $n := \sum_i (m_i > 1)$ $\quad i := 1 .. n$

Laminate thickness: $t := \sum_i \Delta z_i$ $\quad t = 1.0084 \times 10^{-2}$

$$R := \begin{pmatrix} 1 & 0 & 0 \\ 0 & 1 & 0 \\ 0 & 0 & 2 \end{pmatrix}$$

Lamina locations: $z_1 := \frac{-t}{2}$ $\quad z_{i+1} := z_i + \Delta z_i$

Define 2-d compliance matrix:

$$Q(k) := \begin{bmatrix} Q11_{(m_k)} & 1 & 0 & 0 & 0 \\ 1 & Q22_{(m_k)} & 0 & 0 & 0 \\ 0 & 0 & kG23_{(m_k)} & 0 & 0 \\ 0 & 0 & 0 & kG31_{(m_k)} & 0 \\ 0 & 0 & 0 & 0 & 1 \end{bmatrix}$$

Define transformation matrix

$$T(k) := \begin{bmatrix} \cos(\theta_k)^2 & \sin(\theta_k)^2 & 0 & 0 & 2\cdot\cos(\theta_k)\cdot\sin(\theta_k) \\ \sin(\theta_k)^2 & \cos(\theta_k)^2 & 0 & 0 & -2\cdot\cos(\theta_k)\cdot\sin(\theta_k) \\ 0 & 0 & \cos(\theta_k) & \sin(\theta_k) & 0 \\ 0 & 0 & -\sin(\theta_k) & \cos(\theta_k) & 0 \\ -(\cos(\theta_k)\cdot\sin(\theta_k)) & \cos(\theta_k)\cdot\sin(\theta_k) & 0 & 0 & \cos(\theta_k)^2 - \sin(\theta_k)^2 \end{bmatrix}$$

$$Q_b(k) := T(k)^{-1}\cdot Q(k)\cdot T(k)^{-1^T}$$

Calculate the Laminate Rigidity Matrices

$$A := \sum_i Q_b(i)\cdot(z_{i+1} - z_i) \qquad D := \frac{1}{3}\cdot\sum_i Q_{bred}(i)\cdot\left[(z_{i+1})^3 - (z_i)^3\right]$$

$A_{1,1} = 4.862\times 10^7$ $\frac{N}{m}$ $A_{3,3} = 2.256\times 10^6$ $\frac{N}{m}$ $D_{1,1} = 5.2194\times 10^2$ $N\cdot m$

$A_{2,2} = 3.535\times 10^7$ $A_{4,4} = 2.6447\times 10^6$ $D_{2,2} = 1.7657\times 10^2$

Effective Laminate Density $\rho bar := \sum_i \rho_i\cdot(z_{i+1} - z_i)$ $\rho bar = 4.3766$ $\frac{kg}{m^2}$

Rotational Inertia $I := \sum_i \rho_i\cdot\left[(z_{i+1})^3 - (z_i)^3\right]$ $I = 8.8047\times 10^{-5}$ kg or $\frac{N\cdot s^2}{m}$

$$\rho barUS := \sum_i \rho US_i\cdot\frac{(z_{i+1} - z_i)}{0.0254} \qquad \rho barUS = 1.6096\times 10^{-5}$$

APPENDIX V. UNCERTAINTY ANALYSIS FOR NDE MEASUREMENTS

The focus of this research relies on the determination of effective flexural plate properties. The accuracy of the determination of material rigidity depends upon the accuracy of distance and time measurements as well as the nonlinear iterative solution process used to obtain material properties from phase velocities. Due to coupling difficulties, inconsistencies have surfaced in transit time measurement. Remaining measurements have relatively small errors compared with that of transit time. Therefore, the uncertainty of estimated material properties will focus solely on transit time errors.

The phase velocity of flexural Lamb waves is dependent upon material properties, geometry, and frequency. The plate rigidities, D_{11} and A_{55}, are coupled in the equation for phase velocity. (Rigidities are a function of material elastic properties and thickness.) This coupling of terms prevents inversion of the phase velocity expression to solve for D_{11} and A_{55} independently. According to Huggins (1983), partial derivatives of the primary measurement (in this case, material properties) must be evaluated; however, without the existence of an independent expression for each primary measurement, this is not possible. Therefore, a numerical approach was taken to determine the uncertainty associated with the primary measurements.

The numerical approach used to determine the percentage of error associated with the estimation of D_{11} and A_{55} was based on transit time errors. Using the properties (density, thickness, D_{11} and A_{55}) of a wood-based composite (Duron), phase velocities were calculated for several frequencies. In addition, the transit time for a given distance (3, 6, 9, or 12 cm) was calculated. An additional set of transit times was created from the calculated times to simulate a transit time measurement error. Errors ranged within ±8 microseconds. From the erroneous transit times, additional phase velocities were calculated. The Excel Solver was used to calculate two new (erroneous) plate rigidity values (D_{11} and A_{55}) for each set of erroneous transit time measurements (-8, -5, -4, -3, -2, -1, 1, 2, 3, 4, 5, and 8 μs). The percentage error in D_{11} and A_{55} was calculated and graphed versus the respective transit time error (Figure 45 and Figure 46). This was repeated for several transducer distances relative to the initial position (30, 60, 90, and 120 mm). Similar graphs were constructed by varying the plate thickness, density, and material properties. The additional graphs showed no significant changes in the relationship between material property percentage error and transit time error. Therefore, error percentage stays somewhat constant for differences in material properties.

To evaluate the transit time error associated with coupling, the transducers were held at a constant distance while readings were acquired. Excitation frequencies of 20 and 45 kHz were used to transmit flexural plate waves through the panel. The transducer, couplant, and coupling pad were removed from the panel surface and replaced between readings. Periodically, the pad was removed and couplant was re-applied. The transit time of five phase points within the acquired signals (Figure 47 and Figure 48) was monitored and recorded. The transit times for each phase point were plotted for each reading (Figure 49 and Figure 50) and analyzed for variation (Table 17 and Table 18).

Using the results from the transit time error calculations, the percentage error in material properties may be determined by using Figure 45 and Figure 46. With a transit time variation of ±1.0 microsecond and a 6.0-cm total transducer distance, the percentage error for both flexural and transverse shear rigidity values was approximately ±1.0 percent. For a 9.0-cm total transducer distance (used at lower frequencies), the error is a few fractions of a percent smaller.

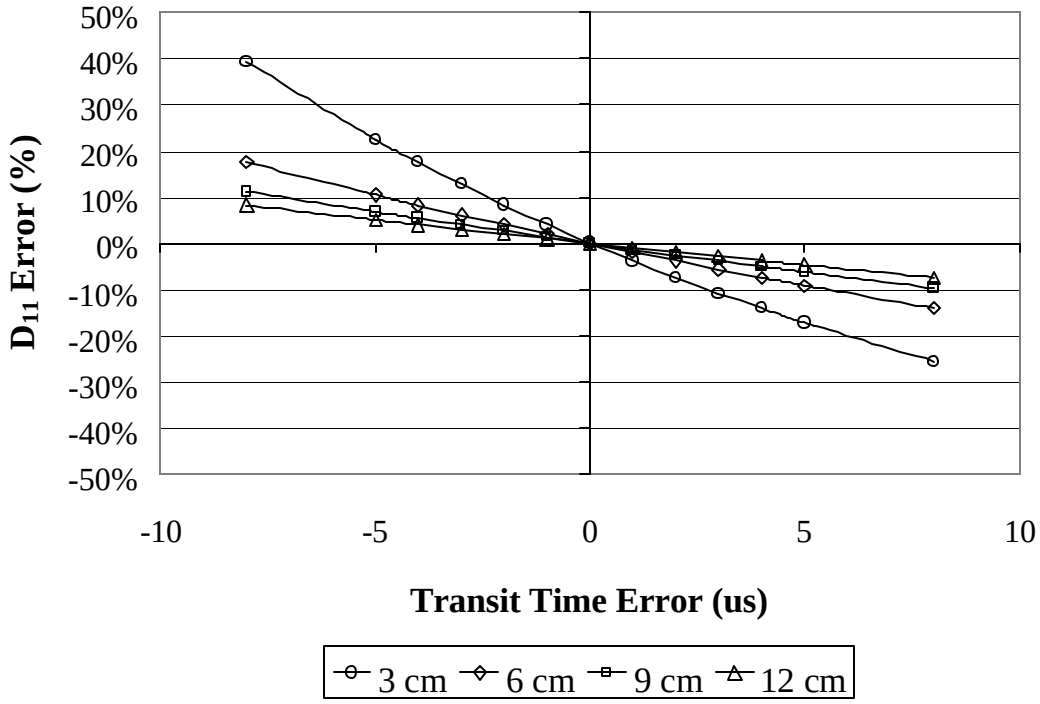

Figure 45: Effect of transit time error on flexural rigidity

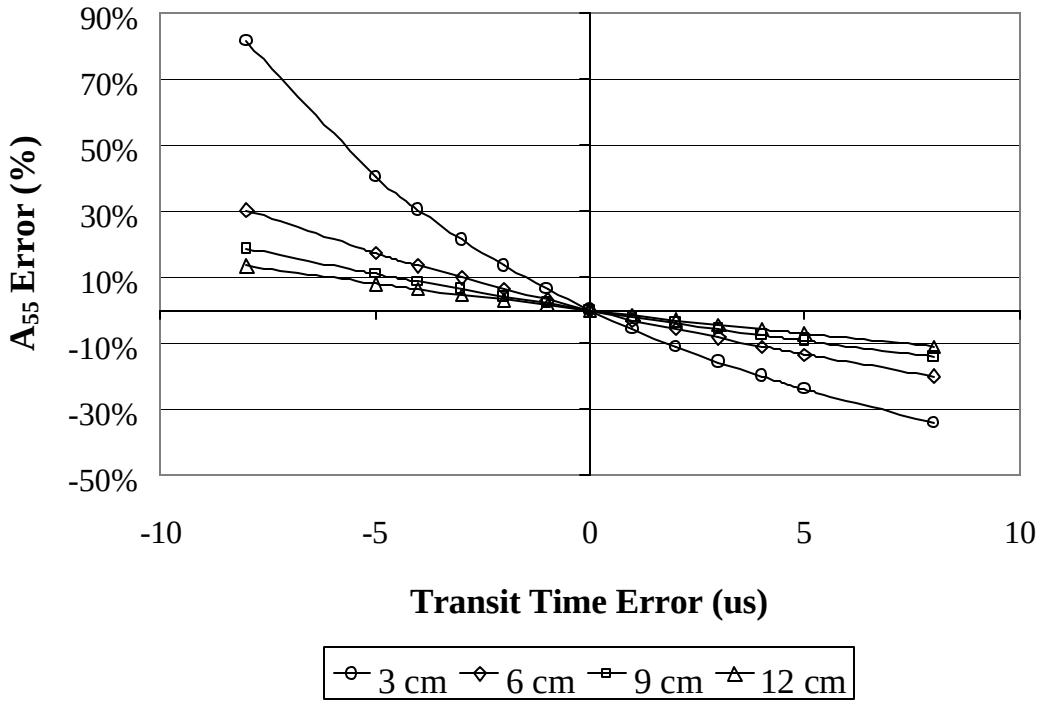

Figure 46: Effect of transit time error on transverse shear rigidity

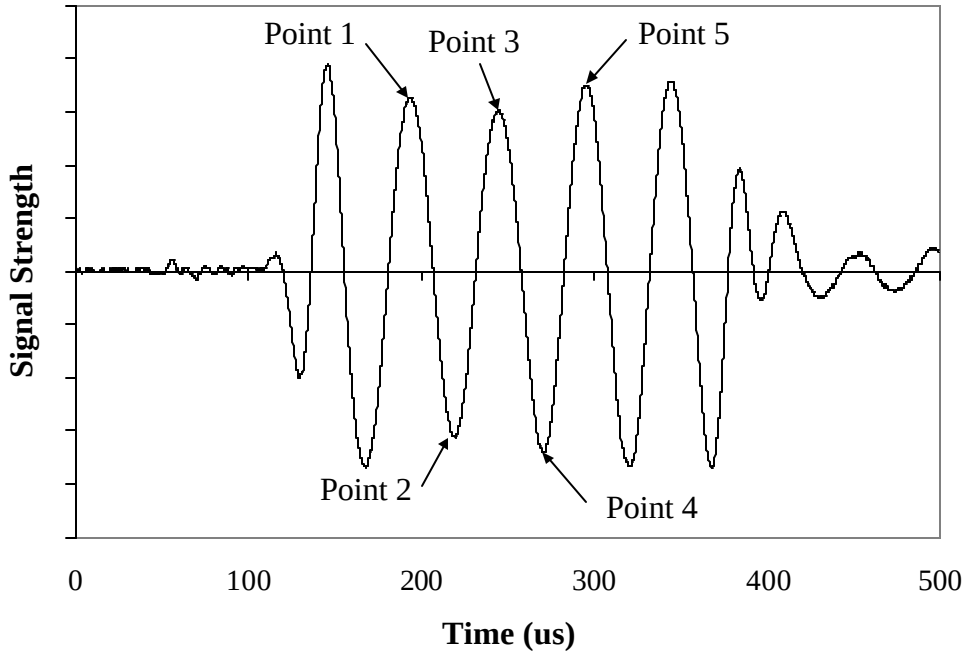

Figure 47: Sample 20-kHz signal showing phase points for uncertainty analysis

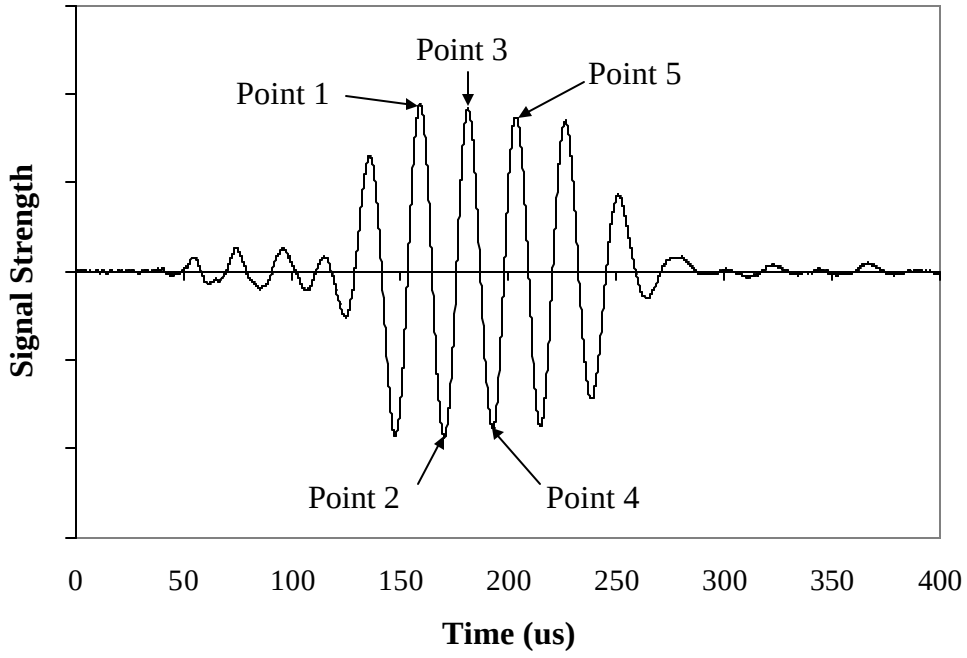

Figure 48: Sample 45-kHz signal showing phase points for uncertainty analysis

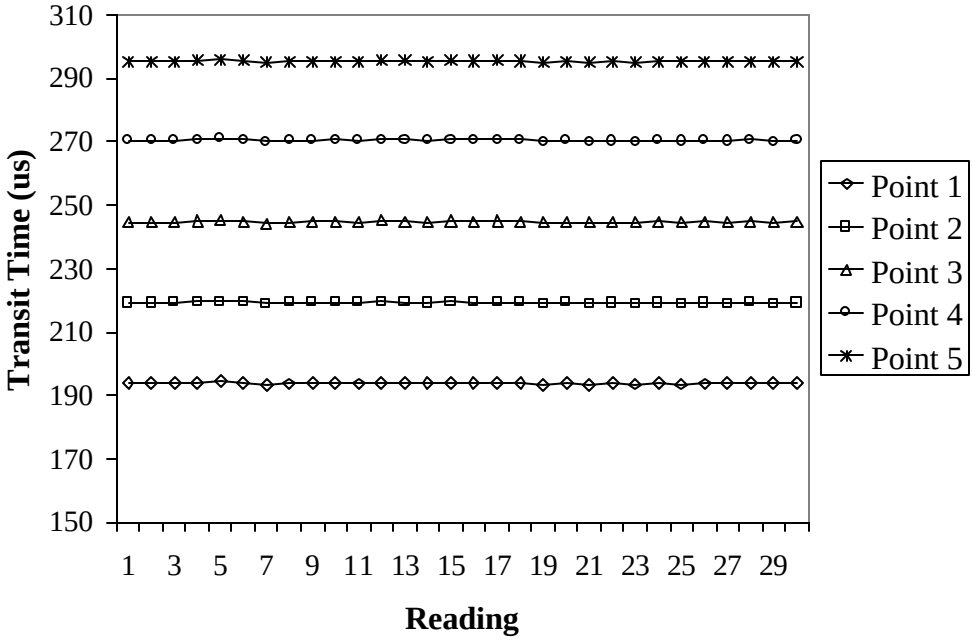

Figure 49: Transit times at a constant transducer distance for repeated 20 kHz signals

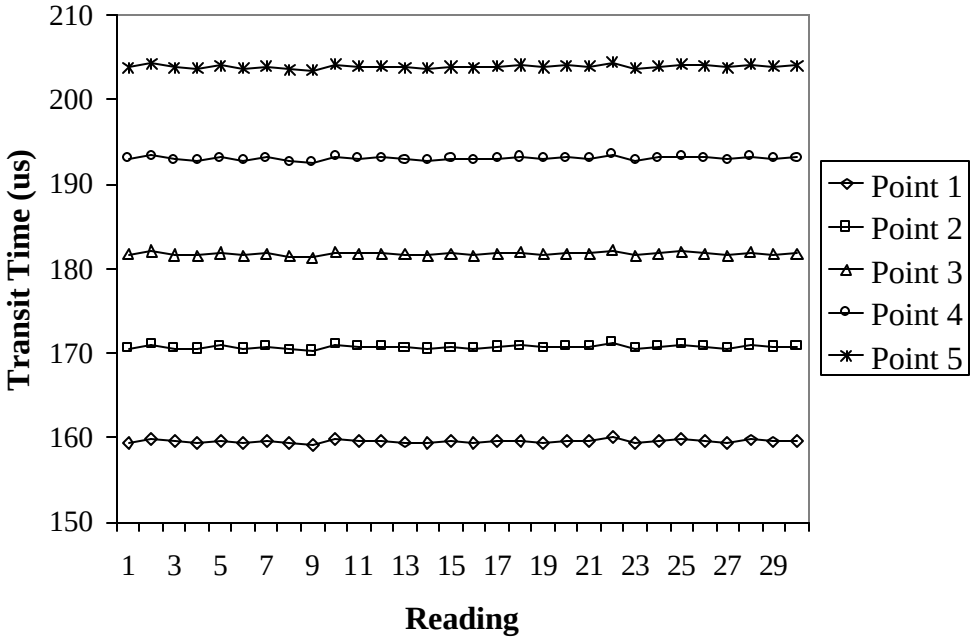

Figure 50: Transit times at a constant transducer distance for repeated 45 kHz signals

Table 17: Variation of phase points for 20-kHz signal

	Point 1	Point 2	Point 3	Point 4	Point 5
AVG	194	219	245	270	295
STDEV	0.216	0.213	0.230	0.234	0.200
CV	0.11%	0.10%	0.09%	0.09%	0.07%

Table 18: Variation of phase points for 45-kHz signal

	Point 1	Point 2	Point 3	Point 4	Point 5
AVG	160	171	182	193	204
STDEV	0.174	0.212	0.187	0.200	0.214
CV	0.11%	0.12%	0.10%	0.10%	0.11%

THE END